論文 / 著書情報
Article / Book Information

題目(和文)	1073 Kにおけるフェライト系Fe-Cr合金の内部酸化/外部酸化の遷移に及ぼす水蒸気の影響
Title(English)	The effect of water vapor on transition of internal/external oxidation in ferritic Fe-Cr alloy at 1073 K
著者(和文)	ﾓﾊﾏﾄﾞ ﾊﾅﾌｲ
Author(English)	Mohd Hanafi Bin Ani
出典(和文)	学位:博士(工学), 学位授与機関:東京工業大学, 報告番号:甲第7744号, 授与年月日:2009年6月30日, 学位の種別:課程博士, 審査員:
Citation(English)	Degree:Doctor (Engineering), Conferring organization: Tokyo Institute of Technology, Report number:甲第7744号, Conferred date:2009/6/30, Degree Type:Course doctor, Examiner:
学位種別(和文)	博士論文
Type(English)	Doctoral Thesis

The effect of water vapor on transition of internal/external oxidation in ferritic Fe-Cr alloys at 1073 K

Supervisor :
Prof. MARUYAMA Toshio
Associate Prof. KAWAMURA Kenichi

Department of Metallurgy and Ceramics Sciences
Tokyo Institute of Technology
06D06133
Mohd Hanafi Bin Ani

Contents

Chapter 1

Introduction

1.1 Research background

It is a matter of common knowledge that anthropogenic sources of green house gases like carbon dioxide (CO_2), methane, chlorofluocarbons and nitrous oxide are changing the climate of the world. Due to their propensity to insulate the earth like a blanket, the increasing emission of these gases increasingly cause retention of heat in the upper atmospheres and average global temperatures. Earlier, having realized the impending consequences of global warming, around 160 nations of the world had jointly implemented the UN Framework Convention on Climate Change (UNFCCC) by signing the Kyoto Protocol in December 1997. Although the protocol did not become legally binding due to non-involvement of U.S. and Australia, most of the remaining industrialized nations had set targets to reduce green house emissions and achieve their preset reduction goals by 2010. However, the European commission has recently issued warning that 13 of the EU's 15 member states were set to miss their emission targets by a huge margin. Thus the Kyoto Protocol, which was widely considered to be the only feasible opportunity to address the impending environmental disaster appears to be off the track.

Figure 1.1 shows the concentration of CO_2 in the global atmosphere from 1000 to 2000 A.D [1]. Pre-industrial CO_2 levels hovered around 280 ppm until 1850. Human activities pushed those levels up to close to 370 ppm by early 2000.The rate of increase

in CO_2 concentrations accelerated over recent decades along with fossil fuel emissions. Since 2000, annual increases of 2 ppm or more have been common, compared with 1.5 ppm per year in the 1980s and less than 1 ppm per year during the 1960s. Global temperatures have been recording a steady rise along with the quantities of CO_2 and methane in the atmosphere.

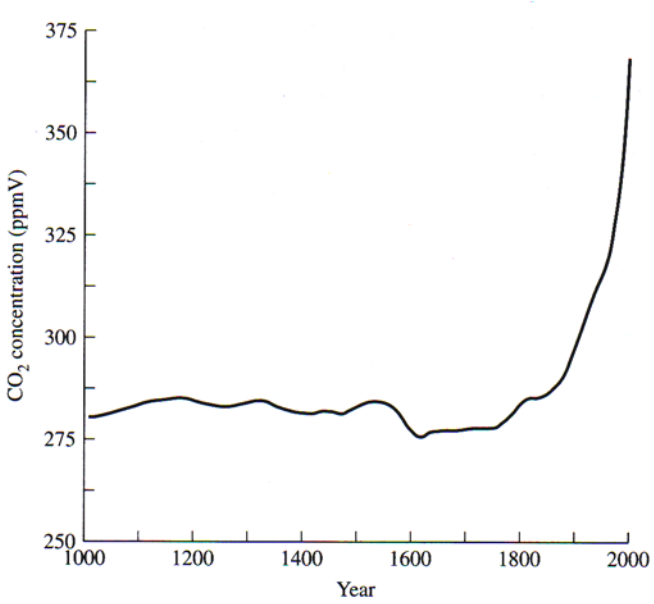

Fig 1.1 The increase of CO_2 concentration in the atmosphere from 1000 to 2000 A.D [1].

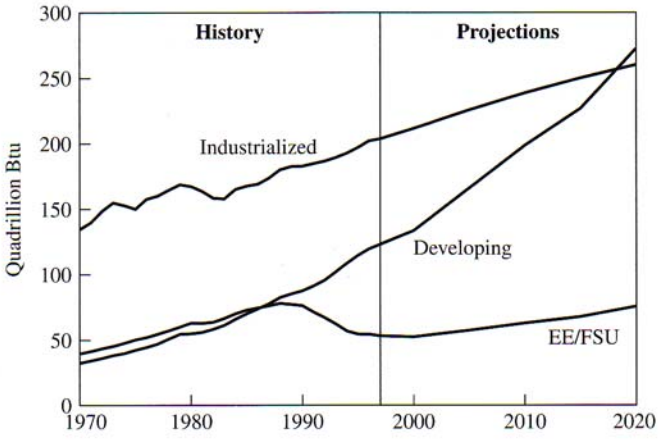

Fig. 1.2 Trend of world's energy consumption to 1997 and a projection to 2020. EE/FSU : Eastern European and former Soviet Union countries [4].

The Intergovernmental Panel on Climate Change (IPCC) has forecast in its Fourth Assessment Reports, 2007 [2] that global warming is set to intensify in the coming years, the long range effects of which would be unprecedented phenomena like rising oceans, melting of glaciers, dissolution of polar caps, extreme weathers, rise in tropical diseases, changes of seasons and disruption of ecosystems. Reports from different parts of the world already hint at the possibility that global warming may be slipping out of human control due to the fact that CO_2 has crossed over its delicate threshold value of around 380 ppm in the earth's atmosphere in the year 2006.

The world fossil fuel emission of CO_2 exceeded 20 billion tons annually during the late 1990s [3]. Available statistics of that time indicate that fossil fuelled combustion accounted for 89% of the commercial energy consumption in the U.S. and 80% of total energy consumed worldwide. The demand for energy was then growing, at around 3% per annum among the industrialized countries, while it had touched around 7% in the Third World whose population is three times that of the developed countries [3]. Figure 1.2 depicts the world energy consumption from 1970 to 1997, and a projection to 2020 [4]. Projection of energy consumption in 2020 shows that less developed countries will consume larger percentage of the world's energy than the industrialized countries.

In 2002 about 40% of carbon dioxide emissions in the U.S. came from the burning of fossil fuels for the purpose of electricity generation. Even by the end of the second decade of 21st century, 90% of energy worldwide would still be supplied by fossil fuels. Thus, there appears to be no end in sight, in the near future, to the compounding environmental problems caused by rising global demands for energy and industrialization.

International community has comes up with strategies to countermeasure this problem. A certain approach is to increase the efficiency of power generation in conventional power plant. While others propose to fully implement new technology in power generation such as solid oxide fuel cells (SOFCs). The primary constraint to realize these strategies is due to the lack of materials for high temperature environment. Materials problems for high temperature are associated with high oxidation rate, phase stability, void formation and exfoliation of oxide scale. Moreover, oxidizing

environments, such as the existence of water vapor in conventional power generation and electrodes of SOFCs, accelerates the oxidation rates of employed materials. Overcoming these problems is crucial in order to achieve higher efficiency in energy generation.

A reduction up to one million tons of CO_2 emission can be achieved in the lifetime of an 800MW fossil fuel power plant by increasing its efficiency by 1% [6]. While the utilization of SOFCs offers emission free and higher energy conversion efficiency up to 60%. This energy conversion efficiency is higher about 20% compared to conventional fossil fuel power plant. This obviously necessitates the development and use of suitable high temperature materials that can comply with the elevated temperature service. In both conventional power plant and SOFCs, it has long been known that steam oxidation greatly reduces the oxidation resistance of the alloys. Materials with better resistance to steam oxidation and improved properties of creep rupture strength are obviously the need of the hour to facilitate such elevated temperature operations of power plants dictated by the crucial considerations of global warming.

1.2 Fossil fueled power plants

The energy crisis of the 1970s triggered the first global attempt on improving thermal energy conversion efficiency of power plants. The worldwide interest in improving energy efficiency was necessitated mainly by an increasing consensus that all anthropogenic sources of green house gases should be trimmed to keep global climate changes in check. The increasing cost of natural gas was another compelling factor to that effect.

The energy conversion efficiency of a thermal power plant depends on its ability to operate at higher steam temperatures and pressures. Carnot cycle is the most efficient cycle possible for converting a given amount of thermal energy into work. A thermodynamic cycle occurs when a system is taken through a series of different states,

and finally returned to its initial state. In the process of going through this cycle, the system may perform work on its surroundings, thereby acting as a heat engine. A heat engine acts by transferring energy from a warm region to a cool region of space and, in the process, converting some of that energy to mechanical work. The cycle may also be reversed. The Carnot energy conversion efficiency is shown as below.

$$\eta_{\text{car}} = \frac{T_2 - T_1}{T_2} \tag{1.1}$$

where T_1 is the absolute temperature of the cold reservoir, T_2 is the temperature of the hot reservoir. Larger difference between the low-temperature heat source and high-temperature heat source will results an increase of Carnot efficiency. Figure 1.3 shows the Carnot cycle efficiency as a function of maximum process temperature [5]. Some examples of current high efficiency power plant are included in the figure. There is a gap between the Carnot efficiency and the efficiency of currently operating power plant due to internal losses and lack of completeness of water/steam cycle (Carnotisation gap). The gap is decrease with increase of temperature. Therefore, in the thermal power plant, gas turbines, aircraft engines, high-temperature equipments in chemical industry, municipal incinerators, many efforts have been done aiming to achieve higher operating temperature, and further increase thermal efficiency output.

Advance steam power plant has been a main subject of research in Japan, US and Europe. Overview of recent research and development project is shown in Fig. 1.4 [7]. Numerous heat-resisting steels of ferritic 9-12%Cr have been developed to achieve supercritical steam condition.

Supercritical (SC) and ultra super critical (USC) steam power plants are widely recognized as the main viable options for future energy generation in many countries. SC in thermodynamics means the state of a substance where there is no clear distinction between liquid and gaseous phases. Water reaches this state at a temperature of 373°C and a pressure of 22.1 MPa. In power plant, SC or USC is always referring to turbine inlet steam condition for main steam pressure and reheat steam.

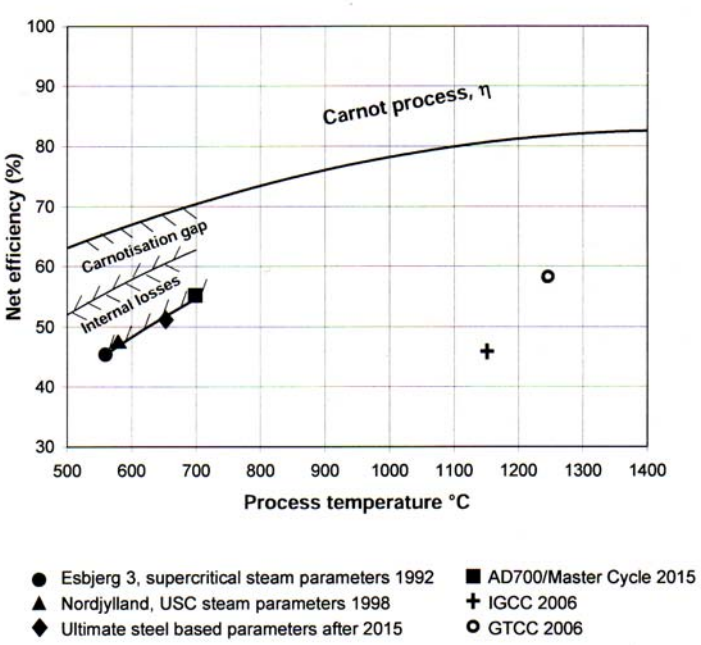

Fig. 1.3 Carnot efficiency and some power plant efficiency as a function of process temperature [5].

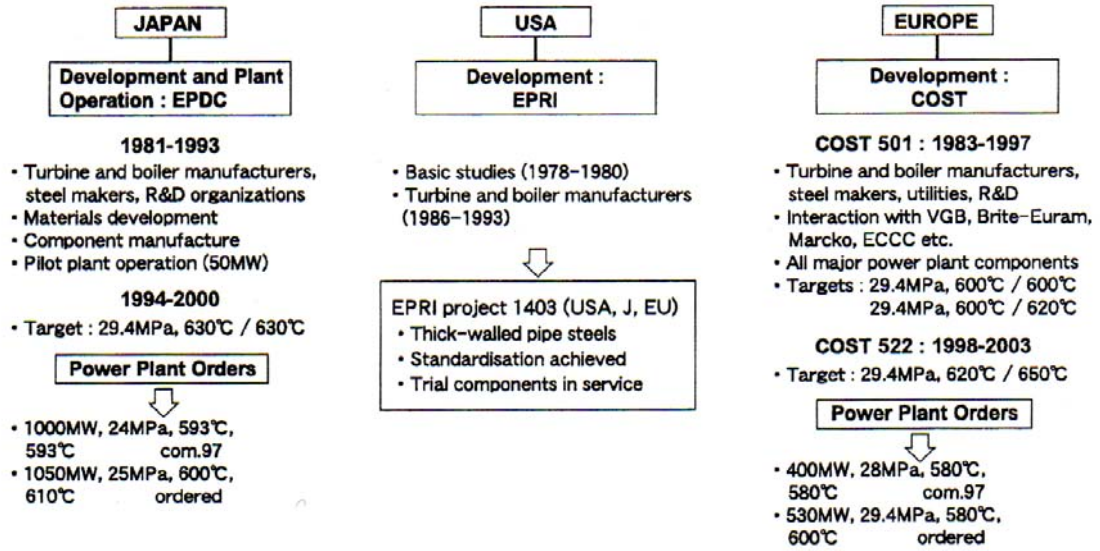

Fig. 1.4 Recent research and development projects on steam power plant [7].

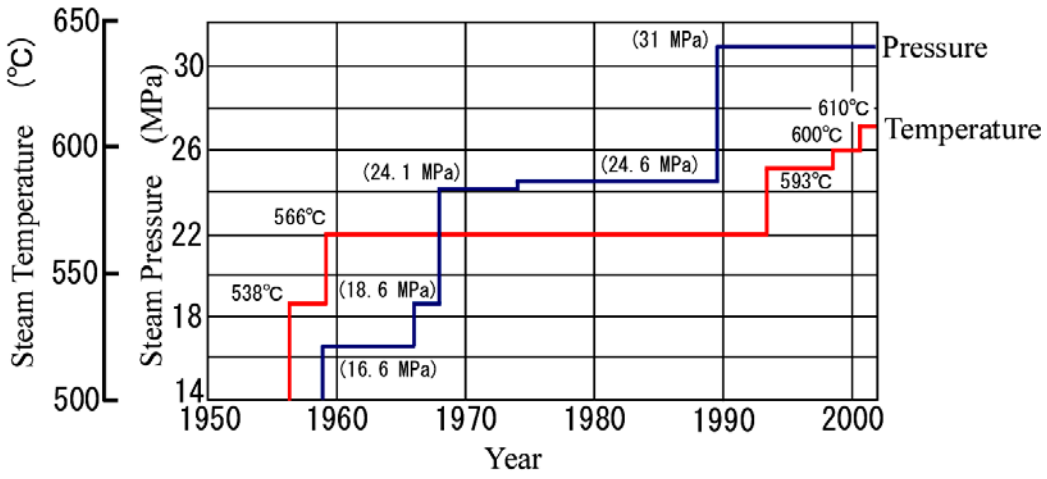

Fig. 1.5 Increase of steam temperature and pressure of power plant in Japan [8].

Figure 1.5 shows the increase of service temperature and pressure of steam power plant in Japan. Modern USC power plant began in the early 1980s with operating temperature of 829 K at 24.6 MPa. Currently, the operating steam condition of fossil power plant with Fe-Cr ferritic steels has successfully increased to 883 K at 31 MPa. Now the target has been set to achieve a goal of 973 K at around 38 MPa pressure [8].

Figure 1.6 shows a schematic diagram of steam power plant. In the combustion chamber, fuel is burned to generate heat. Superheater, reheater etc are installed as heat exchanger to efficiently transfer the heat energy to the steam. The heat is used to boiled water in boiler to produce steam. Superheated steam is then circulated through steam piping to turbine to rotate it and then converted to electric energy by power transformer. The steam from turbine is cooled back to water in condenser, which is fed back to boiler to repeat the cycle again.

To achieve high temperature and high pressure steam condition, components such as boiler tubes or pipeline with higher creep strength and oxidation resistance is required because it is the major determinant the maximum operating temperature and pressure of power plant. Ferritic steels are preferred for heavy, thick-walled components

due to their smaller coefficient of thermal expansion, which reduces significantly thermal stress.

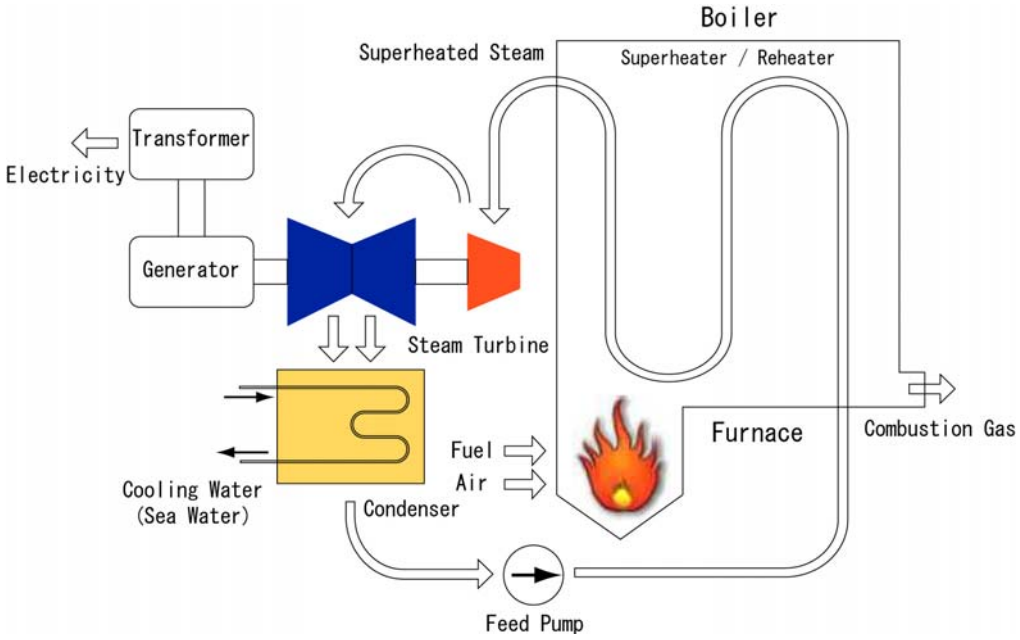

Figure 1.6 Schematic diagram of steam power plant.

1.2.1 Ferritic steels for boiler used in fossil fueled power plant

High-pressure steam piping and heater, superheater tubing and waterwall tubing are the key components in USC plants. Ferritic steels include carbon steels (C-Mn, etc.), low alloy steels (0.5% Mo, ~2.25 % Cr-1% Mo), intermediate alloy steels (5 – 10% Cr) and high alloy steels (12% Cr martensitic steels and 12 – 18% Cr ferritic steels of the AISI400 series).

Steels are designed by taking great consideration of their service condition and environments. When a new alloy is modified from existing steels, their general properties such as oxidation resistance are expected to be close to the original steels. Hence, chemical compositions and heat treatment conditions are examined in particular

to improve the creep strength. Figure 1.7 shows the general concept of alloy design to improve creep strength by the modification of existing steels [7].

Figure 1.8 shows a flow chart of alloy design of 12% Cr steels[7]. Primary properties of this steels are oxidation resistance, creep strength, weldability and toughness because these steels are mainly used in large diameter and thick–walled pipes. 9% Cr would be insufficient in terms of oxidation resistance if the steel to be used up to 923 K, therefore, 12% Cr must be used.

Many studies have been done on the effects of alloying elements on the creep strength of 9 – 12% Cr steels. Cr is a basic alloying element in ferritic steels, and increase Cr concentration improves oxidation resistance. Cr percentage near 2% and 9 – 12% gives high creep strength. However, the strength is decreases at Cr concentration between the two ranges.

Table 1.1 shows nominal chemical composition of ferritic steels for boilers[7]. Figure 1.9 shows the development of ferritic steels of 2% Cr, 9% Cr and 12% Cr with 10^5 h creep rupture strength at 873 K[7]. Steels with 9% and 12% Cr are relatively good in corrosion resistance. The thickness of pipe wall of these steels can be reduced compared to conventional 2.25% Cr – 1% Mo steels.

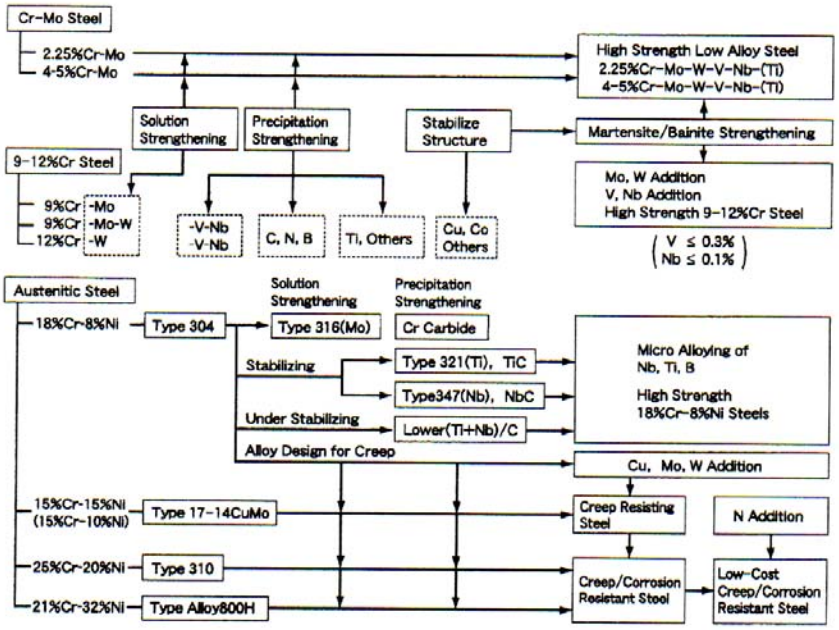

Fig 1.7 General concept of alloy design to improve creep strength by the modification of existing steels [7].

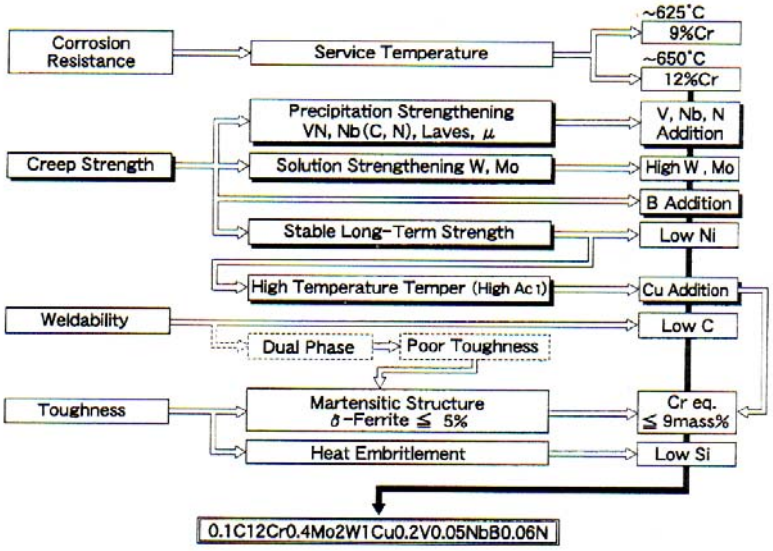

Fig 1.8 Flow chart of alloy design of 12Cr0.4Mo2WcuVNb steel [7].

Table 1.1 shows nominal chemical composition of ferritic steels for boilers [7].

	Steels	Specification		Chemical Composition (mass %)											
		ASME	JIS	C	Si	Mn	Cr	Mo	W	Co	V	Nb	B	N	Others
2%Cr	2.25Cr1Mo	T/P22	STBA24	0.12	0.3	0.45	2.25	1.0	—	—	—	—	—	—	—
	2.25Cr1.6WVNb	T/P23	STBA24J1	0.06	0.2	0.45	2.25	0.1	1.6	—	0.25	0.05	0.003	—	—
9%Cr	9Cr1Mo	T/P9	STBA26	0.12	0.6	0.45	9.0	1.0	—	—	—	—	—	—	—
	9Cr2Mo	—	STBA27	0.07	0.3	0.45	9.0	2.0	—	—	—	—	—	—	—
	9Cr1MoVNb	T/P91	STBA28	0.10	0.4	0.45	9.0	1.0	—	—	0.20	0.08	—	0.05	—
	9Cr0.5Mo2WVNb	T/P92	STBA29	0.07	0.06	0.45	9.0	0.5	1.8	—	0.20	0.05	0.004	0.06	—
	9Cr1Mo1WVNb	T/P911	—	0.11	0.3	0.45	9.0	1.0	1.0	—	0.20	0.08	0.003	0.06	—
	LowC9Cr1MoVNb	—	—	0.06	0.5	0.60	9.0	1.0	—	—	0.25	0.40	0.005	—	—
	9Cr2MoVNb	(NFA49213)		0.10	0.4	0.10	9.0	2.0	—	—	0.30	0.40	—	—	—
12%Cr	12Cr1MoV	(DIN X20CrMoV121)		0.20	0.4	0.60	12.0	1.0	—	—	0.25	—	—	—	0.5Ni
	12Cr1MoWV	(DIN X20CrMoWV121)		0.20	0.4	0.60	12.0	1.0	0.5	—	0.25	—	—	—	0.5Ni
	12Cr1Mo1WVNb	—	SUS410J2TB	0.10	0.3	0.55	12.0	1.0	1.0	—	0.25	0.05	—	0.03	—
	12Cr0.4Mo2WCuVNb	T/P122	SUS410J3TB	0.11	0.1	0.60	12.0	0.4	2.0	—	0.20	0.05	0.003	0.06	1.0Cu
	11Cr2.6W2.5CoVNbBN	—	—	0.08	0.2	0.50	11.0	0.2	2.6	2.5	0.20	0.07	0.004	0.05	—
	11Cr3W3CoVNbTaNdN	—	—	0.10	0.3	0.20	11.0	—	3.0	3.0	0.20	0.07	—	0.04	0.07Ta, 0.04Nd

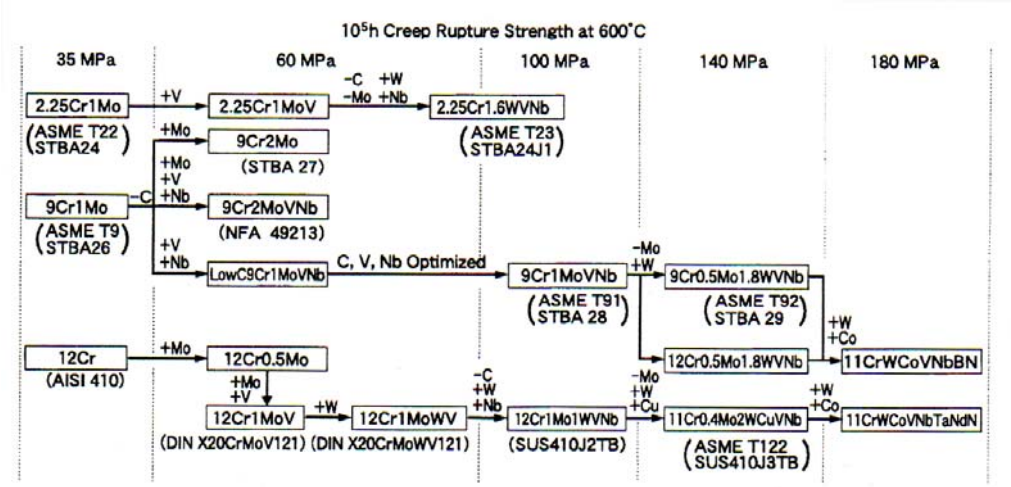

Fig 1.9 The development of ferritic steels of 2% Cr, 9% Cr and 12% Cr with 10^5 h creep rupture strength at 873 K [7].

1.2.2 Steam oxidation of ferritic alloy steel used in boiler

In a boiler operating at high temperature, steam dissociates into its constituent elements hydrogen and oxygen when it comes into contact with metal surfaces, which is followed by a severe oxidation of the metal surface. Steam oxidation has been widely recognized as one of the stumbling blocks to any further improvements in the ferritic Cr steels as they exist today. Oxide films formed on the steam side of boiler tubes can cause major failures. Main problems due to steam oxidation are the exfoliation of oxide scale and solid-particle erosion of turbine components caused by exfoliated scale. Moreover, increased stresses can cause premature failures due to local stress induced creep. Oxide films cause thermal insulation effect on tubes due to their low thermal conductivity thereby impeding heat transfer resulting in higher component temperatures. This causes scaling, deposit formation, reduction in cross sectional area of load bearing sections.

Ueda [9] has analyzed the tube material of JIS火STBA27 steel (9% Cr – 2% Mo) which was exposed to steam condition up to 70000 hours. The estimated temperature is 828 K to 848 K. Figure 1.10 shows the fracture surface of cross section of the oxide scales that exposed to steam condition. The scale is consists of outer scale, inner scale and intermediate layer between outer and inner scales. Internal oxide precipitates between inner scale and alloy substrate. In the outer scale, Fe_2O_3 and Fe_3O_4 is formed, while in the inner scale $(Fe,Cr)_3O_4$ is formed. Interestingly, in the intermediate layer, a great volume of void was observed. The formation of void leads to the exfoliation of outer scale.

Many investigations were carried out on ferritic Cr alloys oxidized in steam condition and dry condition [10 – 15]. It was unequivocally established that wet oxygen is far more corrosive than dry oxygen. In dry oxygen, the chromium in steel initially forms a protective chromium rich oxide film over the entire surface of the metal component, protecting it from any further rapid oxidation. However, in the presence of water vapor, rapid oxidation is observed. This matter attracts special interest from many researchers, however their explanations remain in qualitative manner and there is no consensus regarding the cause of accelerated oxidation in steam condition.

Essuman[16] has studied the oxidation of Fe-10% Cr and Fe-20% Cr alloys in Ar-20% O_2, Ar-4% H_2-7% H_2O and Ar-7% H_2O mixed gaseous. Internal precipitates of oxide were formed in the presence of water vapor, which change the oxidation mechanism. This shows that water vapor affects the transport processes in the alloy. Cr is oxidized internally and not forming protective external scale. They speculated that water vapor affects the solubility and/or diffusivity of oxygen in the alloy. However no quantitative analysis was done.

Exfoliation of oxide scale is a main problem in the high temperature oxidation of ferritic steel. The presence of steam in the oxidation environment accelerates the oxidation rates. From the point of practical view, it is very important to control the oxide scale from exfoliation and establish protective scale during early stage of oxidation. In order to solve above issues, it is essential to understand the effect of steam on the mechanism of high temperature oxidation. In this study, the oxidation mechanism

steam condition was clarified in the view of mass transport process in the alloy and was compared to dry condition.

Fig. 1.10 Fracture surface of cross section of scale forms in steam side of boiler tube [9].

1.3 Solid Oxide Fuel Cells

The development of Solid Oxide Fuel Cells (SOFCs) attracts a lot of attention and has been a subject of intensive research due to its potential to convert chemical energy (fuel sources) to electrical energy directly without combustion. In conventional steam power plant, the chemical energy is first converted to mechanical energy to rotate the turbine, and later converted to electrical energy. This intermediate step of conversion into mechanical energy is one of the reason that conventional power plant having a lower efficiency in energy conversion.

The electric generation base on theoretical solid-state energy conversion is a promising technology to cope the crucial problem of global warming. Energy generation from SOFCs offers a lot of advantages such as zero emission, high efficiency, low environmental impact and zero noise pollution. It is a promising technology as a power sources to households, commercial buildings, vehicles and aircraft systems. These applications will give great impacts to the energy industry worldwide.

The main parts of SOFCs are ion conducting electrolyte, anode, cathode and interconnector. Schematic diagram of SOFCs is shows in the Fig. 1.11. A single cell of SOFC generates only about 1 V. In a planar type SOFC, the cell parts are stacked together and later connected into siries to generate sufficient high power output. Interconnector material plays an important role as it enables the electric connection between anode of a unit cell to cathode of the other cell. It also separates fuel in anode from air in cathode. For that reason, interconnector material is exposed in severe oxidizing and reducing environments at each side. For example, Kurokawa [17] has summarized the oxygen, water vapor and hydrogen potential in anode and cathode. The results are shown in the Table 1.2. The oxygen potential for anode and cathode is around 4.1×10^{-17} Pa and 2.1×10^{4} Pa, respectively. Many challenges to commercialize SOFCs are due to materials related issues.

In early development of SOFCs, the operating temperature is set to be around 1273 K due to limited conductivity of solid electrolyte at that time. However, recently the development of thin-electrolyte cells with improves cathode materials enables the

operating temperature to be reduced around 923 K ~ 1073 K. Lower operating temperature of SOFCs permits the use metallic interconnector. Zhu and Deevi[20] have summarized the characteristics that been required for interconnector.

i) High electronic conduction, low ohmic loss.

ii) Adequate stability of dimension, microstructure, phase and chemistry.

iii) Low permeability of oxygen and hydrogen to minimize direct combination of oxidant and fuel during cell operation.

iv) Thermal expansion coefficient should comparable to electrodes and electrolyte to avoid the generation of thermal stress during start-up and shut down process.

v) No reaction between interconnect and anode/cathode.

vi) Good thermal conductivity.

vii) Excellent oxidation, sulfidation and carburization resistance.

viii) Easy to fabricate.

ix) High temperature strength and creep resistance.

Metallic materials fit above characteristics and have been intensively studied to evaluate their potential as interconnector material. The successful development of competent and affordable metallic interconnect is essential to the commercialization of SOFCs.

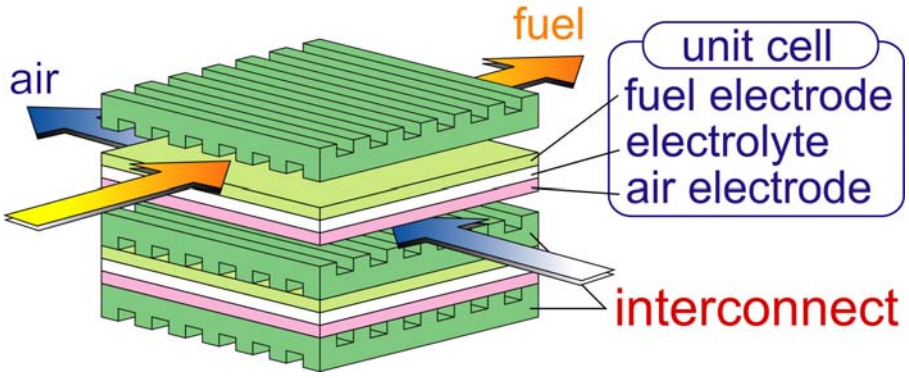

Fig 1.11 Schematic diagram of SOFCs and oxidizing conditions of each electrodes [17].

Table 1.2 The oxygen, water vapor and hydrogen potentials in anode (fuel side) and cathode (air side) [17].

	Anode	Cathode
P_{O2} / Pa	4.1×10^{-17}	2.1×10^{4}
P_{H2O} / Pa	3.0×10^{3}	$6.0 \times 10^{2} \sim 2.0 \times 10^{3}$
P_{H2} / Pa	1.0×10^{5}	-

Japan, US and European countries have been actively developing SOFCs. In Japan, New Energy and Industrial Technology Development Organization (NEDO) is overseeing the commercialization of national SOFCs project. The project is divided into phases, and has started since year 1989 with cooperation of corporate companies such as Hitachi, TOTO, MMC, Mitsubishi Heavy Industry (MHI) and others. The tasks [18] of each company are show in Fig. 1.12. NEDO has planned the commercialization of SOFCs earliest by the year 2008. The project schedule is shows in Fig. 1.13. It intends to develop full system and basic technology of SOFCs for the future. Among the important tasks are including designing new materials and high performance stack technology.

Intermediate Temperature SOFCs (IT-SOFCs) with operating temperature below 1073 K and ferritic alloys as interconnectors is definitely an attractive and promising technology that needs to develop further. As the consequences, the basic knowledge of steam oxidation on ferritic alloys used as interconnectors in anode and cathode condition is essentials to better evaluate the performance of SOFCs. Ferritic alloy with substantial amount of Cr is a prospective candidate as it nearly fit the above characteristics for interconnector materials.

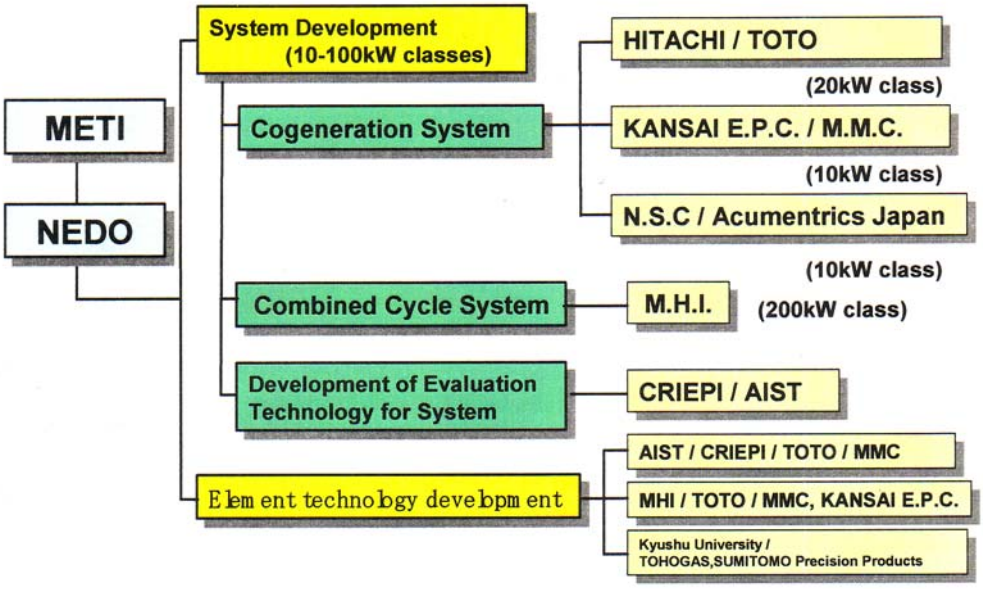

Fig 1.12 Task of each company to commercialize SOFCs in Japan under coordination of NEDO [18].

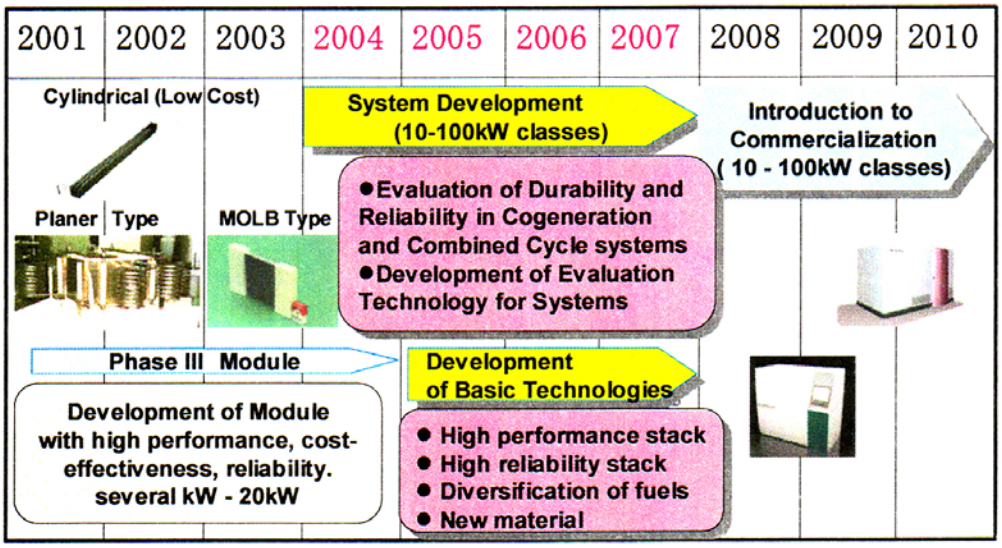

Fig 1.13 The SOFCs project's progress and plan until year 2010 in Japan [18].

1.3.1 Ferritic alloys for SOFCs interconnector

Lower operating temperature of SOFCs allows the use of alloys in the cell stacks. As alloys could easily be manufacture compared to ceramic materials, it greatly contributes to the reduction of fabrication cost which is one of important factor to commercialize SOFCs technology. Perry and Tuller [19] have reported that the main challenges of lowering the operating temperature are reducing the ohmic losses, electrolyte stability and cathode polarization. The using of thinner interconnector helps in achieving acceptable conductance. Recently, many works [20-24] have been done aiming to explore the possibility of metallic alloys as interconnector. Alloys design for interconnector is differ from alloys for power plant in a manner that electrical conductivity of oxides formed in both side of anode and cathode is given a top priority since it will affect the cell's performance. Moreover, studies of steam oxidation on metallic interconnect emphasis on its' effects on electrical conductivity in longer cell's running time rather than to clarify the oxidation mechanism.

Ferritic Cr_2O_3-forming [24 - 25] alloys are promising candidates as interconnector because the Cr_2O_3 scale has suitable properties of low growth rate and reasonable electronic conductivity. Table 1.3 shows the electrical resistivity and thermal expansion coefficient of some oxide scales [20]. Among the inert oxides, i.e SiO_2, Al_2O_3 and Cr_2O_3, Cr_2O_3 shows an extremely low electrical resistivity by a few magnitudes compared to the other two oxides at 1073 K. This fact has been well understood since Cr_2O_3 is an intrinsic semiconductor at high temperature, while SiO_2 and Al_2O_3 are insulators. Due to this crucial property, the development of new ferritic alloys for SOFCs interconnects always concentrate on Cr_2O_3 forming alloys rather than SiO_2 or Al_2O_3 forming alloys, although both the latter oxides have excellent oxidation resistance.

Fergus [25] has summarized metallic alloys used for interconnector as shown is Table 1.4. The properties of each alloy are compared including oxidation resistance, volatility, electrical resistance and thermal expansion. In developing alloys for interconnector, Cr composition was altered from 10 wt % up to 30 wt % with very small alloying elements such as Si and Al. Some of the alloys have been developed as

commercial alloys such as Hitachi ZMG232 (Hitachi Metals), E-brite (Allegheny Ludlum) and Crofer 22 APU (ThyssenKrupp VDM).

Table 1.3 Electrical resistivity and thermal expansion coefficient of Cr_2O_3 scale and some others oxide scales [20].

Oxide	Electrical resistivity / (Ωcm)	Electrical resistivity at 25 ℃ / (Ωcm)	Thermal expansion coefficient (25 ~1000℃) x 10^{-6} per ℃
SiO_2	7 x 10^6 at 600℃	1 x 10^{14}	0.6
Al_2O_3	5 x 10^8 at 700℃	3 x 10^{14}	8
Cr_2O_3	1 x 10^2 at 800℃	1.3 x 10^3	9.6
NiO	5~7 at 900℃	1 x 10^{13}	14
CoO	1 at 950℃	1 x 10^8	-
MgO	1.8 x 10^7 at 800℃	5.5 x 10^{14}	15.6
TiO_2	1 x 10^2 at 900℃	1 x 10^{11}	7~8

Table 1.4 Chemical composition of alloys for SOFCs.

Nominal compositions of iron-based alloys

Alloy	Concentration (wt%)										
	Fe	Cr	Mn	Mo	W	Si	Al	Ti	Y	Zr	La
Fe–10Cr	Bal	10	<0.02			<0.1					
1.4724	Bal	13					1				
SUS 430	Bal	16–17	0.2–1.0			0.4–1.0	≤0.2				
Fe–17Cr–0.2Y	Bal	17							0.2		
1.4016	Bal	17									
Ferrotherm (1.4742)	Bal	17–18	0.3–0.7			0.8–0.9	0.9–1.0				
Fe–18Cr–9W	Bal	18			9						
Fe–20Cr–7W	Bal	20			7	0.3	0.6			0.3	
Fe–20Cr	Bal	20	<0.02			<0.1					
ZMG 232	Bal	21–22	0.5			0.4	0.1–0.2			0.2	0.04
AL 453	Bal	22	0.3			0.3	0.6	0.02			0.1
Fe22CrMoTiY	Bal	22	0.1	2		<0.05	< 0.05	0.3	0.4		
1.4763(446)	Bal	24–26	0.7–1.5	≤0.05		0.4–1		< 0.05			
FeCrMn(LaTi)	Bal	16–25	?					?			?
Fe–Cr–Mn	Bal	16–25	?								
Fe–25Cr–DIN 50049	Bal	25	0.3			0.7		0.01			
Fe–25Cr–0.1Y–2.5Ti	Bal	25						2.5	0.1		
Fe–25Cr–0.2Y–1.6Mn	Bal	25	1.6						0.2		
Fe–25Cr–0.4La	Bal	25									0.4
Fe–25Cr–0.3Zr	Bal	25								0.3	
Fe26CrTiY	Bal	26	0.1	< 0.02		<0.05	< 0.05	0.3	0.4		
Fe26CrTiNbY	Bal	26	Composition not provided, but presumably same as Fe26CrTiY with Nb								
Fe26CrMoTiY	Bal	26	0.1	2		<0.05	< 0.05	0.3	0.3		
E-Brite	Bal	26–27	≤0.1	1		0.03–0.2	≤0.05	≤0.05	≤0.01		
Al29–4C	Bal	27	0.3	4		0.3		?			
Fe–30Cr	Bal	30	<0.02			<0.1					

Symbol '?' indicates element is present, but concentration is not specified.

Alman and Jablonski [26] have measured the area specific resistance (ASR) of Crofer 22 APU coupons (Fe-22Cr-0.5Mn-0.1Ti-0.1La-<0.1Al-<0.1Si (wt%)) in moist air at 1073 K. The samples were divided into treated sample with Ce and untreated sample. Sample treated with Ce was preheated at 673 K and sprayed with cerium-nitrate salt slurry. After deposition, samples were oxidized at 673 K to decompose cerium-nitrate salt and deposit CeO_2 on the surface. The result of ASR measurement is showed in Fig. 1.14. Sample treated with Ce on the surface has a lower ASR compared to untreated sample. Moreover, Alman and Jablonski [26] have reported that sample with Ce surface treatment shows lower mass gain as untreated sample, which reflects to better oxidation resistance. Surface treatment on interconnector alloys is an important and challenging task because it requires that the alloys must not degrade the electrical performance as well as effectively reducing oxidation. For example, alloys with dilute alloying elements are having a tendency to form internal oxide of SiO_2 or Al_2O_3. These two oxides are insulators, and their present in alloy matrix may increase the alloy ASR. The results of Alman and Jablonski [26] show that surface treatment suppress the formation of internal oxide, thus decrease the ASR value.

Titanium was added into ferritic steel to improve the performance of oxide layer [27]. The formation of TiO_2 at the oxide-alloy interface improves the scale adherence and mechanical properties of the scale. Mn was added to obtain better electrical conductivity of the scale. The formation of Mn spinel at the scale surface is beneficial to block the formation of volatile Cr species gas [25,27-28]. Moreover, some studies have reported that the addition of reactive element such as La, Nd and Y may also enhance the electrical properties as well as increase the scale adherence [29-31]. The selection of alloying element for SOFCs interconnector mainly relies on their properties to improve electrical conductivity and scale adherence.

It is clear that the oxidation of metallic interconnector directly affects the performance of SOFCs. Further studies to understand the steam oxidation mechanism, particularly the formation of protective Cr_2O_3 scale, the formation of internal oxide and the transition form internal to external scale are urgently needed. Understanding of these

subjects will pave a way to design improved alloy for interconnector.

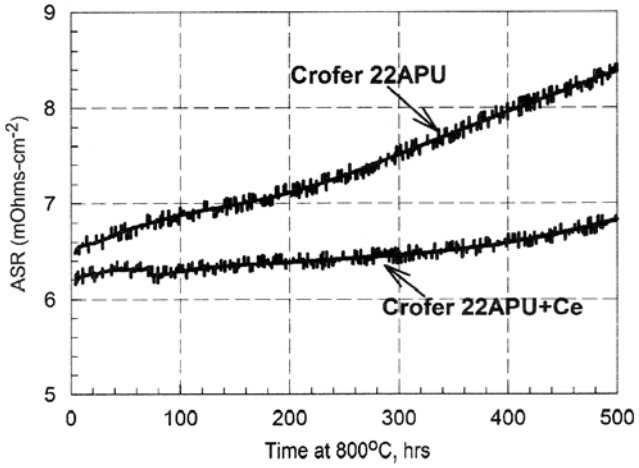

Fig 1.14 The results of area specific resistance (ASR) of Crofer 22 APU alloys with untreated surface and Ce treated surface in moist environment at 1073 K [26].

1.3.2 Oxidation of ferritic alloys for SOFCs interconnector

The oxidation of metallic interconnector is another important aspects as it significantly affects the cell's performance [32]. An oxide scale forms on the surface of metallic interconnects at high temperature may reduces the electric conductivity of the material and thereby SOFC power output. Chromia-forming ferritic stainless steels are currently well known as a promising alloy group for SOFC interconnects because an electrically conductive oxide scale forms at high temperature. Nevertheless, in water vapor containing environment, many studies reported that the formation of protective Cr_2O_3 scale is retarded [10-16]. The reasons of the increase of oxidation rate in water vapor environment are remains unclear. However, some studies suggest that ferritic alloy have low resistance to Cr_2O_3 evaporation in the SOFCs operating environment. Evaporation of Cr species results in continuous removal of protective Cr_2O_3 scale. Moreover, Volatile Cr species such as CrO_3 and $CrO_2(OH)_2$ can contaminate the cathode and cause rapid degradation of cell performance [28].

Many studies has been done to investigate the oxidation of metallic interconnector in water vapor condition [25-35], yet little has clarified about the mechanism. Hammer et. al. [28] has has extensive summarize the results of cyclic oxidation of ferritic steels at 973 K – 1173 K in simulated SOFCs atmosphere. At temperature above 1073 K, 10% of water vapor significantly degrades the performance of the alloys, which leads to excessive spallation of Fe-26Cr, Crofer 22APU, E-brite and AL43 alloys. Moreover, a very small variation of minor element or impurities such as Si and Al greatly changes the oxidation behaviors. Alman and Jablonski [26] also have commented on the presence of such minor element as it could decrease the area contact resistance (ASR). From these works, it is apparent the importance to form protective Cr_2O_3 scale at very early stage of oxidation as it could retard the formation of insulating internal oxides such as SiO_2 and Al_2O_3. Moreover, the mechanism of Cr evaporation needs to be clarified in order to sustain the SOFCs performance in longer run.

1.4 Objective and overview of the thesis

It is in the backdrop of global warming and the consequent need for reduction in CO_2 emissions, that operation of steam power plant at higher temperature is essential to improve the energy conversion efficiency. Notwithstanding to the advancement of ferritic alloy development, steam oxidation has been identified as one of the limiting factors to operate steam power plant at higher temperature due to it behavior is not fully understand.

Furthermore, the trend of lower operating temperature of SOFCs around 1073 K enables ferritic alloys to be used as interconnector. But this has rises the concern about the cell performance in the existence of oxide scale. In the SOFCs oxidizing environment, Cr may evaporate and deposited in cathode side, which degrade the cells. Moreover, the presences of insulating internal oxides also have detrimental effects on generated cell’s power.

In both cases, power plant and SOFCs, the formation of protective Cr_2O_3 scale

is the keyword to achieve higher energy conversion efficiency. However, the role of water vapor in accelerating oxidation rates is still not well explained. Understanding of this matters are important to counterattack above problems, hence improve the energy generation in both system.

The objective of this study is to inspect the effects of water vapor on the rapid oxidation of ferritic steels with special attention to the transition from internal oxidation to the formation of protective Cr_2O_3 scale at early stage of oxidation. However, conventional inspection method to clarify the internal-external oxidation requires laborious works and time consuming. Hence, in addition to above objective and in industrial viewpoint, a new method was developed to continuously monitor the formation of protective scale by monitoring the surface oxygen potential. Akiba [36] was previously measured the oxygen potential on FeO surface successfully. This is an extension works to apply the method into ferritic alloys.

This thesis is concerned with the transition from internal to external oxidation of ferritic Fe-Cr alloys in steam condition compared to dry condition. By inspecting the formation of internal-external scale at early stage in dry and humid condition, the effects of water vapor could be clarified. Figure 1.15 shows the overview of this thesis.

In **Chapter 1 ; "Introduction"**, the background of this study was presented with the emphasis to increase power generation efficiency. Recent trend in steam power plant, the roles of ferritic alloys, and the problems encountered by ferritic alloy in power plant was reviewed. Moreover, the development of metallic interconnector of SOFCs with special attention to ferritic alloys was highlighted. The problems on high temperature oxidation of interconnector were reviewed. The objectives of this study were cited from the standpoint of conventional power plant and metallic interconnector of SOFCs.

In **Chapter 2 ; "High temperature oxidation of Fe-Cr alloy at 1073 K in dry and humid atmospheres with the oxygen partial pressure of the Fe-FeO coexistance"**, the effect of water vapor on the oxidation of the alloys in Fe/FeO oxygen partial pressure at 1073 K was clarified base on Wagner theory of transition from internal to external oxidation. The formation of internal precipitated oxide and external scale in

both conditions was given special attention.

In **Chapter 3 ; "Oxygen permeability in internal oxidation zone of Fe-Cr alloys at 1073 K under dry and humid conditions"**, the permeability of oxygen was measured form internal oxidation of Fe-0.5 ~ 2.25% Cr alloys in dry and humid condition. The oxygen permeability change in both conditions was inspected. The microstructure change of internal precipitated oxide was observed and the effect of humidity on high temperature oxidation was clarified.

In **Chapter 4 ; "Measurement of surface oxygen potential on Fe-Cr alloys in dry and humid atmospheres"**, a new method was proposed to monitor the formation of protective scale on Fe-Cr alloys at early stage of oxidation by continuously measuring the surface oxygen potential. Protective scale consumes less oxygen and the surface oxygen potential is almost similar to oxygen potential in the environment. While if non-protective scale is formed, the surface oxygen potential is decreases significantly compared to oxygen potential in the environment. The change in surface oxygen potential in dry and humid conditions was evaluated and discussed.

In **Chapter 5 : Conclusion**, the results from this study was summarized.

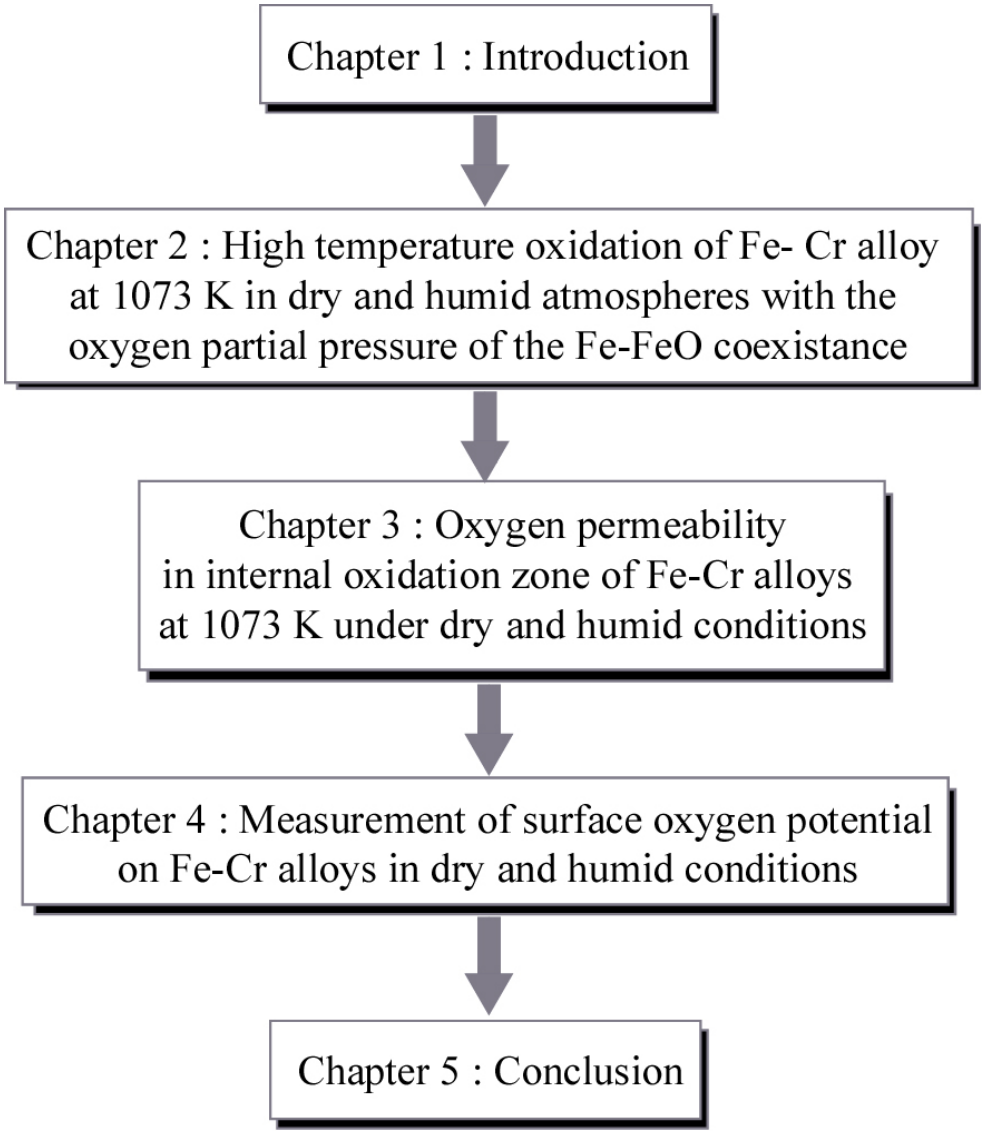

Fig. 1. 15 Overview of the thesis.

References

[1] J. A. Fay and D. S. Golomb, Energy and the Environment, Oxford University Press Inc., 2002.

[2] Intergovernmental Panel on Climate Change / Forth Asssesment Report 2007, http://www.ipcc.ch/pdf/assessment-report/ar4/syr/ar4_syr.pdf

[3] S. C. Edward *Prospects for Sustainable Energy- A Critical Assessment* Cambridge, U.K. The Press Syndicate of The University of Cambridge,2000.

[4] M. Sato, M. Yaguchi, Y. Tanaka, J. Iwasaki, M. Fukuda, E. Saito, H. Nakagawa, A. Shiibashi and S. Izumi, *Karyoku Genshiryoku Hatsuden*, **57** (10), 89-106 (2006), In Japanese.

[5] R. Blum, S. Kjær and J. Bugge, Riso-R-1608(EN) 69-80. http://www.risoe.dk/rispubl/reports/ris-r-1608_69-80.pdf

[6] R. Vishwanathan, & W. T. Bakker, "Materials for Boilers in Ultra Supercritical Power Plants", Proceedings of the 2000 International Joint Power Generation Conference, Miami Beach, Florida, July 23-26,2000,page-2.

[7] F. Masuyama, *ISIJ International*, **41** (6), 612-625 (2001).

[8] M. Sato, M. Yaguchi, Y. Tanaka, J. Iwasaki, M. Fukuda, E. Saito, H. Nakagawa, A. Shiibashi and S. Izumi, *Karyoku Genshiryoku Hatsuden*, **57** (10), 821–838 (2006), In Japanese.

[9] M. Ueda and T. Maruyama, *Zairyo-to-Kankyo*, **54**(5), 175-182 (2005). In Japanese.

[10] J. Zurek, M. Michalik, F. Schmitz, T. U. Kern, L. Singheiser and W. J. Quadakkers, *Oxidation of Metals*, **63** (5/6), 401–422 (2005).

[11] K. Segerdahl, J. E. Svensson and L. G. Johansson, *Journal of the Electrochemical Society*, **151** (7), B394-B398 (2004).

[12] C. T. Fujii and R. A. Meussner, *Journal of the Electrochemical Society*, **111** (11), 1215-1221 (1964).

[13] H. Asteman, K. Segerdahl, J. E. Svensson, L. G. Johansson, M. Halvarsson and T. E. Tang, *Materials Science Forum*, **461-464**, 775-782 (2004).

[14] A. Yamauchi, K. Kurokawa and H. Takahashi, *Oxidation of Metals*, **59** (5/6), 517-527 (2003).

[15] K. Segerdahl, J. E. Svensson and L. G. Johansson, *Materials and Corrosion*, **53**, 247–255 (2002).

[16] E. Essuman, G. H. Meier, J. Zurek, M. Hansel, L. Singheiser and W. J. Quadakkers, Scripta Materialia, 57, 845-848(2007).

[17] H. Kurokawa, K. Kawamura and T. Maruyama, *Solid State Ionics*, **168**, 13-21 (2004).

[18] T. Ujiie, *ECS Transactions*, **7** (1), 3-9 (2007).

[19] M. L. Perry and T. F. Tuller, *Journal of Electrochemical Society*, **149** (7), S59-S67 (2002).

[20] W. Z. Zhu and S.C. Deevi, *Materials Science and Engineering*, **A348**, 227-243 (2003).

[21] W. Z. Zhu and M. Yan, *Journal of Zhejiang University of Science*, **5** (12), 1471-1503 (2004).

[22] W. Z. Zhu and S.C. Deevi, *Materials Research Bulletin*, **38**, 957-972 (2003).

[23] S. Geng and J. Zhu, *Journal of Power Sources*, **160**, 1009-1016 (2006).

[24] S. Geng, J. Zhu, Michael P. Brady, Harlan U. Anderson, X. D. Zhou and Z. Yang, *Journal of Power Sources*, **172**, 775-781 (2007).

[25] J. W. Fergus, *Materials Science and Engineering A*, **397**, 271-283 (2005).

[26] D. E. Alman and P. D. Jablonski, *International Journal of Hydrogen Energy*, **32**, 3743-3753 (2007).

[27] W. J. Quadakkers, J. Piron-Abellan, V. Shemet and L. Singheiser, *Materials at High Temperature*, **20** (2), 115-127 (2003).

[28] J. E. Hammer, S. J. Laney, R. W. Jackson, K. Coyne, F. S. Pettit and G. H. Meier, *Oxidation of Metals*, **67** (1/2), 1-38 (2007).

[29] P. Piccardo, S. Chevalier, R. Molins, M. Viviani, G. Caboche, A. Barbucci, M. Sennour and R. Amendola, *Surface & Coatings Technology*, **201**, 4471-4475 (2006).

[30] G. Cabouro, G. Caboche, S. Chevalier and P. Piccardo, *Journal of Power Sources*, **156** , 39-44 (2006).

[31] S. Fontana, R. Amendola, S. Chevalier, P. Piccardo, G. Caboche, M. Viviani, R. Molins and M. Sennour, *Journal of Power Sources*, **171**, 652-662 (2007).

[32] P. D. Jablonski and D. E. Alman, *Journal of Power Sources*, **180**, 433-439 (2008).

[33] N. Sakai, T. Horita, K. Yamaji, Y. P. Xiong, H. Kishimoto, M. E. Brito, H. Yokokawa, *Solid State Ionics*, **177**, 1933-1939 (2006).

[34] L. Mikkelsen and S. Linderoth, *Materials Science and Engineering A*, **361**, 198-212 (2003).

[35] S. Fontana, S. Chevalier and G. Caboche, *Journal of Power Sources*, (2007), doi:10.1016/j.jpowsour.2008.11.041.

[36] K. Akiba, M. Ueda, K. Kawamura and T. Maruyama, *Materials Transactions*, **49** (3), 629-636 (2008).

Chapter 2

High temperature oxidation of Fe-Cr alloys at 1073 K in dry and humid atmospheres with the oxygen partial pressure of the Fe-FeO coexistence

2.1 Introduction

It was obvious from Chapter 1 that water vapor significantly affects high temperature oxidation of ferritic alloy, contributes to the scale exfoliation and accelerates the reaction rates. Many works have been done to investigate the oxidation in water vapor containing environment, however their explanation remain in qualitative manner and there is a lack of concrete consensus.

Figure 2.1 summarizes the possible effects of water vapor on the high temperature oxidation. Water vapor may affect the oxidation behaviors of alloys in the form of water molecules, hydrogen atoms or protons. The possible effects of water vapor are ;

(i) Impedes the formation of protective scale by promotes the formation of internal oxides with the present of water vapor species. To understand this subject, a details study in the transition from internal to external oxidation is required.

(ii) Water vapor accelerates the vaporization of Cr_2O_3 scale by forming volatile

species of $CrO_2(OH)_2$. The evaporation of Cr_2O_3 makes the scale thin, resulting in rapid oxidation.

(iii) Water vapor dissolves in the Cr_2O_3 scale as proton and alters the defect chemistry of Cr_2O_3 scale. This may lead to an increase of mass transport in Cr_2O_3 scale. The increase of mass transport in Cr_2O_3 scale will directly increase the oxidation rates.

(iv) Water vapor increases the mass transport in gaseous. The formation of void is always observed in the scale on ferritic alloys. Water vapor in the void enhances the mass transport within the void. This result in overall increase of mass transport in the scale, hence increase the oxidation rates.

Among 4 effects mentioned above, the transition from internal to external oxidation is probably the main causes.

In this chapter various Fe-Cr alloys was oxidized in dry and humid environment under same oxygen partial pressure of the Fe/FeO coexistance at 1073 K to clarify how water vapor affects the oxidation behaviors.

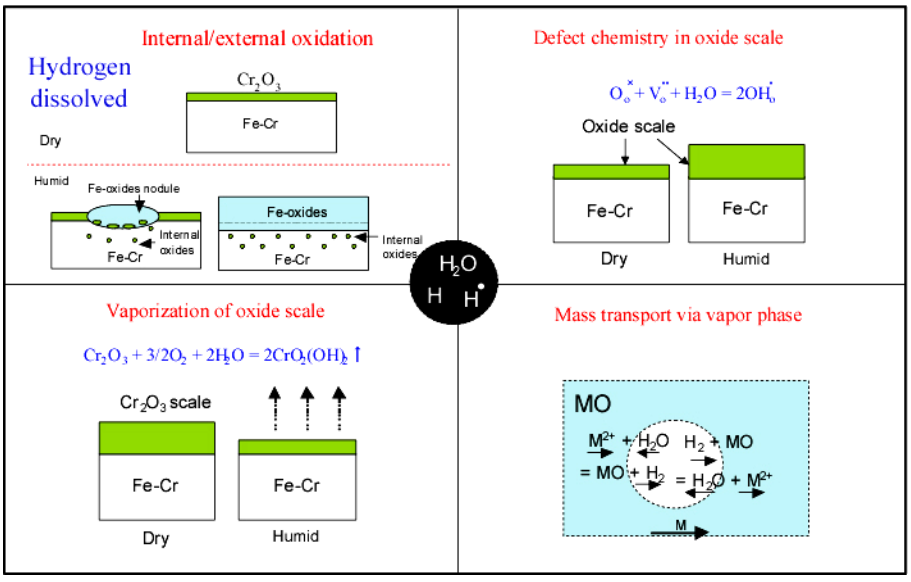

Fig. 2.1 The possible effects of water vapor on the high temperature oxidation.

2.2 The formation of Cr_2O_3 external scales on Fe-Cr alloy

Water vapor is speculated to retard the formation of protective oxide scale. In this chapter, Wagner's [1] treatment of the formation of external scale in binary alloy was applied. Figure 2.2 shows the schematic diagram of the formation of internal oxide and external scale in Fe-Cr alloy. If Cr concentration in Fe-Cr alloy is low, then the internal precipitates of Cr_2O_3 in the alloy matrix (Fig. 2.2(a)). The growth rate of internal oxidation zone (IOZ) is shown as below.

$$V = \frac{dX}{dt} = \frac{N_O^{(s)} D_O}{\nu N_{Cr}^{(0)}} \frac{1}{X} \tag{2.1}$$

where $N_O^{(s)}$ is the mol fraction of oxygen at the metal surface, $N_{Cr}^{(0)}$ is the concentration of Cr in the alloy, D_O is the diffusion coefficients of oxygen in the alloy, X is the thickness if IOZ and ν is the atomic ratio of O to Cr in Cr_2O_3 (ν = 1.5).

From the equation (2.1), the growth rate of IOZ is decrease with the increase of Cr concentration in the alloy and the decrease of oxygen permeability, $N_O^{(s)} D_O$ in the alloy. By increasing the Cr concentration, the outward flux of Cr in the alloy is sufficiently high compare to the inward flux of oxygen. More Cr will be oxidized underneath the alloy surface, which leads to the formation of Cr_2O_3 external scales as illustrated in Fig. 2.2(b).

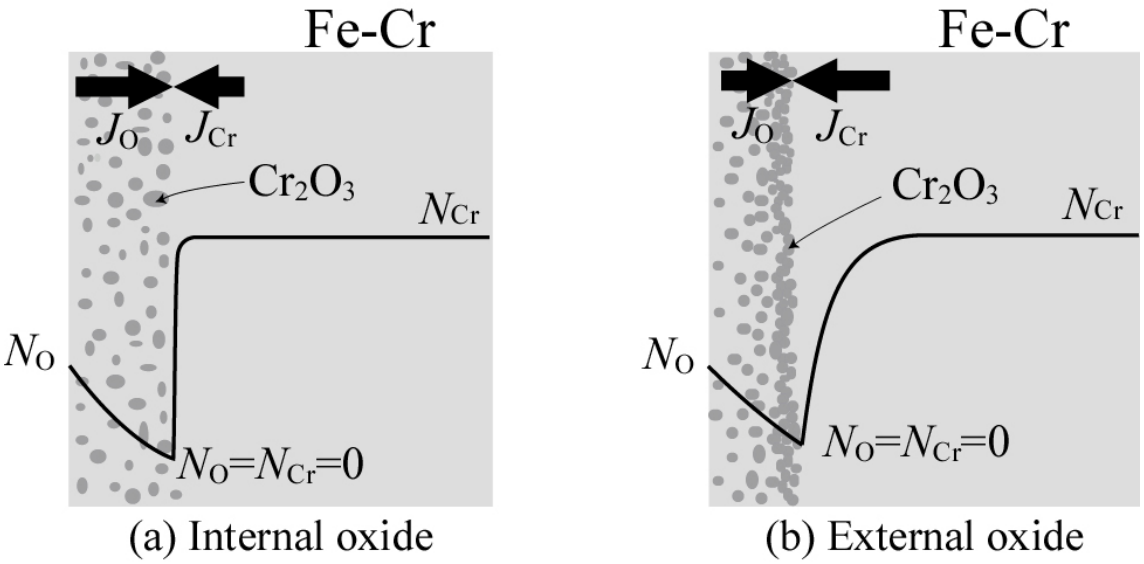

Fig. 2.2 Schematic diagram of the formation (a) internal oxide and (b) external oxide in Fe-Cr alloy.

Wagner has derived a minimum concentration for solute element B in a general A-B binary alloy to form external scales. In case of Fe-Cr alloy, the minimum concentration of Cr is shown as below.

$$N^{*}_{\mathrm{Cr\ (External)}} > \left[\frac{\pi g^{*} N_{O}^{(s)} D_{O} V_{\mathrm{Alloy}}}{2\upsilon D_{\mathrm{Cr}} V_{\mathrm{CrO_{1.5}}}} \right]^{\frac{1}{2}} \tag{2.2}$$

where D_{Cr} is diffusion coefficients of Cr in the alloy, V_{Alloy} and $V_{CrO_{1.5}}$ are molar volumes of alloy and $CrO_{1.5}$. g^* is the volume fraction of internal oxide precipitates at which external oxidation takes place. Rapp [2] has evaluated the transition from internal to external oxidation of In_2O_3 in Ag-In binary alloys and proposed that the value of g^* is 0.3. In this work, the value proposed by Rapp [2] was adopted.

Therefore, if the concentration of Cr in Fe-Cr alloy is higher than the minimum concentration stated in equation 2.2, external Cr_2O_3 scale form at the early stage of oxidation.

However, during a long exposure of oxidation condition, it is necessary for the Cr_2O_3 scale to maintain it protectiveness. After the formation of external scale, the Cr concentration in alloy matrix beneath the scale is depleted as it is consumed during the oxidation. Slight damage on the scale leads a rapid progress of oxidation of the Fe matrix. Consequently, higher Cr flux, J_{Cr} at the metal/oxide interface compare to the flux of Cr in Cr_2O_3, $J_{Cr} > J`_{Cr}$ is prerequisite to maintain the protectiveness of Cr_2O_3 scale. Atkinson [3] has proposed the minimum concentration to maintain the protective external scale base on the Wagner's treatment. The minimum concentration to maintain Cr_2O_3 scale is shown as below.

$$N^{*}_{\mathrm{Cr\ (Maintain)}} = \frac{V_{\mathrm{Alloy}}}{V_{\mathrm{CrO_{1.5}}}}\left[\frac{\pi k_p}{4\tilde{D}}\right]^{\frac{1}{2}} \tag{2.3}$$

where k_p is the parabolic rate constant of the growth of Cr_2O_3 scale, $\tilde{D}$ is the inter-diffusion coefficient in the alloy.

Equation (2.2) and (2.3) was used to calculated the critical concentration of Cr in Fe-Cr alloy to form and to maintain the Cr_2O_3 external scale. Parameter in equation (2.2) and (2.3) that have been used in the calculation is shown in the Table 2.1 and 2.2 respectively. The inter-diffusion coefficient in alloy was obtained from Darken equation as below.

$$\tilde{D} = N_{Cr}D_{Fe} + N_{Fe}D_{Cr} \tag{2.4}$$

Figure 2.3 shows the minimum Cr concentration required to form Cr_2O_3 external scale and to maintain the scale under oxygen partial pressure of dissociation of FeO. For reference, the target USC temperature and operating temperature of SOFCs interconnector, which are 973 K and 1073 K respectively, are included in the figure. The critical Cr concentration to form external Cr_2O_3 scale decreases with an increase of temperature. Similar tendency is observed on the Cr concentration to maintain the external scale. From the calculation, under currently operating USC temperature of 883K and target USC temperature of 973 K, 19 mol% and 14 mol% Cr is needed to form external scale, respectively. At the temperature of this experiment, which is 1073 K, 10.5 mol% of Cr is required to form external scale. The dashed line above the internal external transition line is the predicted transition line if the oxidation is

occurred in the humid condition. The dashed line is draws base on empirical fact that oxidation rate is higher in humid condition. Thus, the line does not represent the actual quantitative value. In this study, the shift from solid line to dashed line is investigated extensively. This constitutes the change of critical Cr concentration to form external scale in dry and humid condition.

Figure 2.3 is used as a reference to decide the alloy composition in the experiment. At 1073 K, the minimum Cr concentration needed to established external Cr_2O_3 scale is calculated to be 10.5 mol%, while 3.7 mol% Cr is required to maintain the Cr_2O_3 scale.

The presence of water vapor is speculated to accelerate the oxidation rates and retards the formation of protective external Cr_2O_3 scale. Accordingly, the minimum concentration to form and maintain external Cr_2O_3 scale is expected to shift into higher concentration.

In this chapter, the Cr concentration around the transition region of internal-external oxidation, which is 8 mol% to 12 mol% Cr was choose to study how water vapor retards the formation of external Cr_2O_3 scale. As a reference, Fe-0.5~5 mol%Cr alloys that precipitate internal oxide and Fe-17 mol% Cr alloy that exhibits external scale in dry and humid condition were selected to compare the oxidation mechanism with the formers.

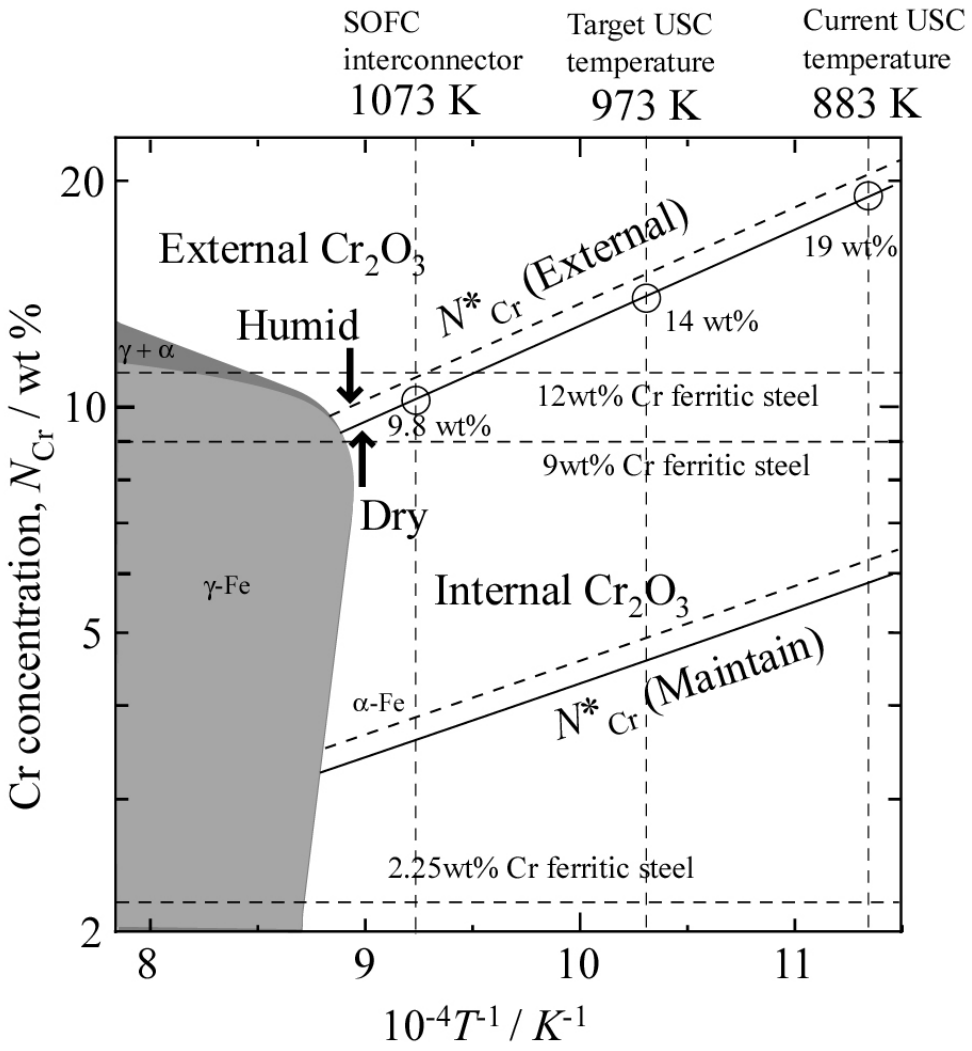

Fig. 2.3 Minimum Cr concentration needed to establish external Cr_2O_3 scale and maintain the scale as a function of temperature at oxygen partial pressure of 1.1 x 10^{-14} Pa.

Table 2.1 Parameters for the calculation of critical bulk Cr concentration to form external Cr_2O_3 scale.

Parameter for calculation		References
v	1.5	
g*	0.3	[2]
N_O (Fe/FeO)	$0.381\exp(-104\text{kJmol}^{-1} / RT)$	[4]
D_O / m^2s^{-1}	$1.79 \times 10^{-7}\exp(-85.7\text{kJmol}^{-1} / RT)$	[5]
D_{Cr} / m^2s^{-1}	$2.33 \times 10^{-4}\exp(-238.8\text{kJmol}^{-1} / RT)$	[6]
V_{Fe} / m^3mol^{-1}	7.09×10^{-6}	
$V_{CrO1.5}$ / m^3mol^{-1}	1.46×10^{-5}	
R / $Jmol^{-1}K^{-1}$	8.315	

Table 2.2 Parameters for the calculation of critical bulk Cr concentration to maintain external Cr_2O_3 scale.

Parameter for calculation		References
$k_p(Cr_2O_3)$ / m^2s^{-1}	$2.7 \times 10^{-8}\exp(-202.2\text{ kJmol}^{-1} / RT)$	[7]
D_{Fe} / m^2s^{-1}	$2.0 \times 10^{-7}\exp(-240.9\text{ kJmol}^{-1} / RT)$	[6]
D_{Cr} / m^2s^{-1}	$2.33 \times 10^{-4}\exp(-238.8\text{kJmol}^{-1} / RT)$	[6]
V_{Fe} / m^3mol^{-1}	7.09×10^{-6}	
$V_{CrO1.5}$ / m^3mol^{-1}	1.46×10^{-5}	
R / $Jmol^{-1}K^{-1}$	8.315	

2.3 Experimental Procedure

2.3.1 Sample preparation

The Fe-0.5~17 wt% Cr binary alloys were prepared by argon-arc melting of the pure constituent metals of Fe (99.99%) and Cr (99.9%). The alloy ingots were homogenized at 1373 K in vacuum for 86.4 ks. Then, the alloys were sliced into coupons of 1 mm thick and grounded to 2000-grit finish using SiC abrasion paper. The samples were then finally polished with 4 μm diamond paste, followed by cleaning in ethanol with ultrasonic agitation.

Chemical composition and phases in the alloys were analyzed using Electron Probe Micro Analyzer (EPMA) and X-ray diffraction (XRD). The chemical compositions of Fe-Cr alloys are shown in Table 2.3. The XRD pattern of the samples in Fig. 2.4 confirmed that the samples are in single phase of α-Fe solid solution.

Table 2.3 The chemical composition of the Fe-Cr alloys analyzed using EPMA.

Alloys	Fe Concentration		Cr Concentration	
	mass %	mole %	mass %	mole %
Fe-0.5Cr	99.51	99.51	0.49	0.49
Fe-2.25Cr	97.76	97.76	2.24	2.24
Fe-8Cr	91.8	91.2	8.2	8.8
Fe-10Cr	90.2	89.5	9.8	10.5
Fe-12Cr	87.5	86.7	12.5	13.3
Fe-17Cr	83.1	82.1	16.9	17.9

2.3.2 Oxidation of Fe-Cr alloys

Figure 2.5 shows the experimental setup. The sample was placed in an air-tight apparatus. Two R-type thermocouples were placed at the top and bottom of the sample to monitor the temperature. The distance between sample and thermocouple is about 5 mm. The isothermal zone is 30 mm range within temperature fluctuation of ±0.5 K.

The oxygen partial pressure in the atmosphere was fixed by an Fe/FeO buffer

and was calculated by the standard Gibbs energy change of the reaction below.

$$0.947\ Fe + 1/2O_2 \rightarrow Fe_{0.947}O \quad (2.5)$$

FeO was known as a non-stoichiometric oxide having a chemical composition of $Fe_{0.947}O$ at 1073 K. Figure 2.6 shows the non-stoichiometry in FeO as a function of temperature [8]. The standard Gibbs energy change of the equation (2.5) at 1073 K is -194.7 $kJmol^{-1}$ from thermodynamic data compiled by Barin [9]. The calculated equilibrium oxygen partial pressure is 1.1×10^{-14} Pa.

For the oxidation in dry environment, the apparatus was evacuated using a rotary pump for 1.8 ks and closed. The sample was heated to 1073 K and hold for 172.8 ks to 691.2 ks. For the oxidation in humid environment, the apparatus was evacuated, filled with Ar - 5% H_2 gas of 3×10^4 Pa and closed. The sample was heated to 1073 K and hold for 172.8 ks to 691.2 ks. Hydrogen in the chamber reacts with oxygen to form water vapor as the following manner,

$$H_2 + 1/2O_2 \rightarrow H_2O \quad (2.6)$$

At 1073 K, the measured total pressure of the apparatus was 4×10^4 Pa. Using the standard Gibbs energy change of -188.7 $kJmol^{-1}$ at 1073 K compiled by Barin, the water vapor pressure is calculated to be 3.3×10^2 Pa. After oxidation, the samples were cooled to room temperature in the furnace.

Oxide phases formed were analyzed by X-ray diffraction (XRD) using the divergence slit of 1 degree. A fluorescence plate was used to estimate the irradiation area of the x-ray. At low diffraction angle of 20° the irradiation area is 19 x 14 mm, and at high diffraction angle of 80° the irradiation area is 6 x 14 mm. To examine the oxide phases in the internal oxidation zone, a sample was tilted by 2 degree and polished. Distribution of elements was analyzed by EPMA. Surface morphology was observed by scanning electron microscopy (SEM).

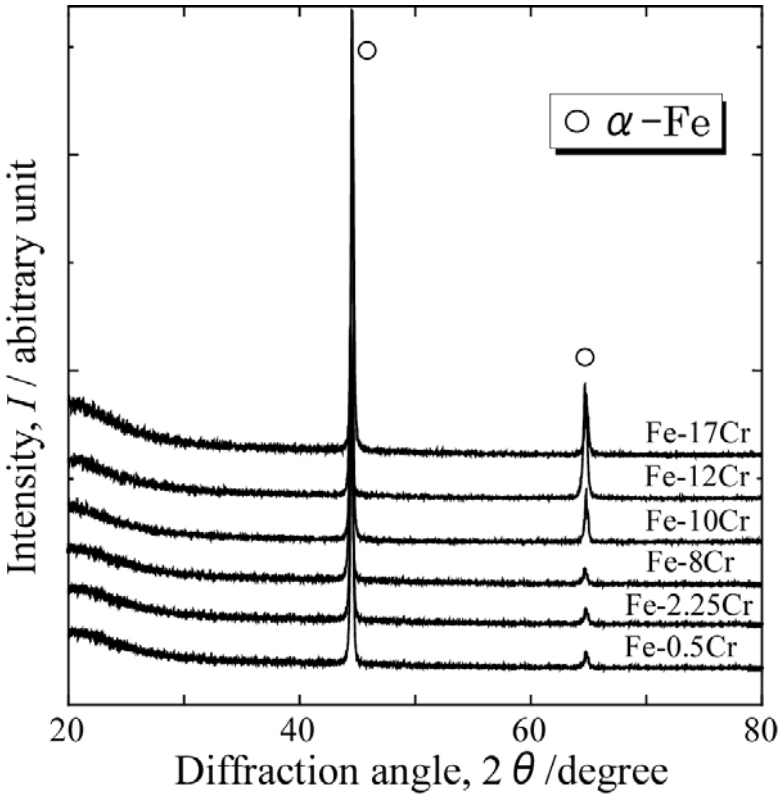

Fig. 2.4 XRD patterns of Fe-Cr alloys before oxidation.

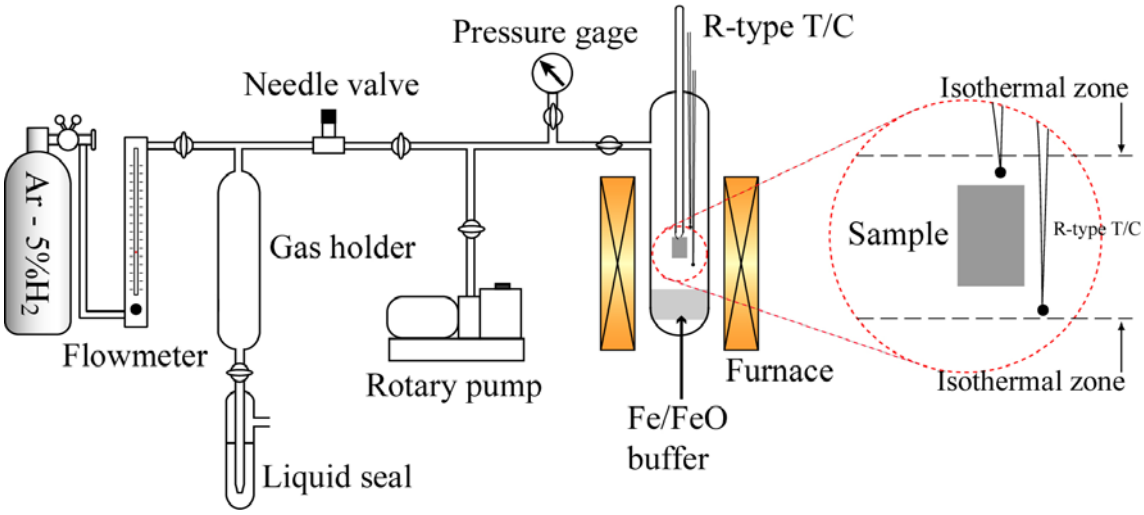

Fig. 2.5 Schematic diagram of the oxidation apparatus.

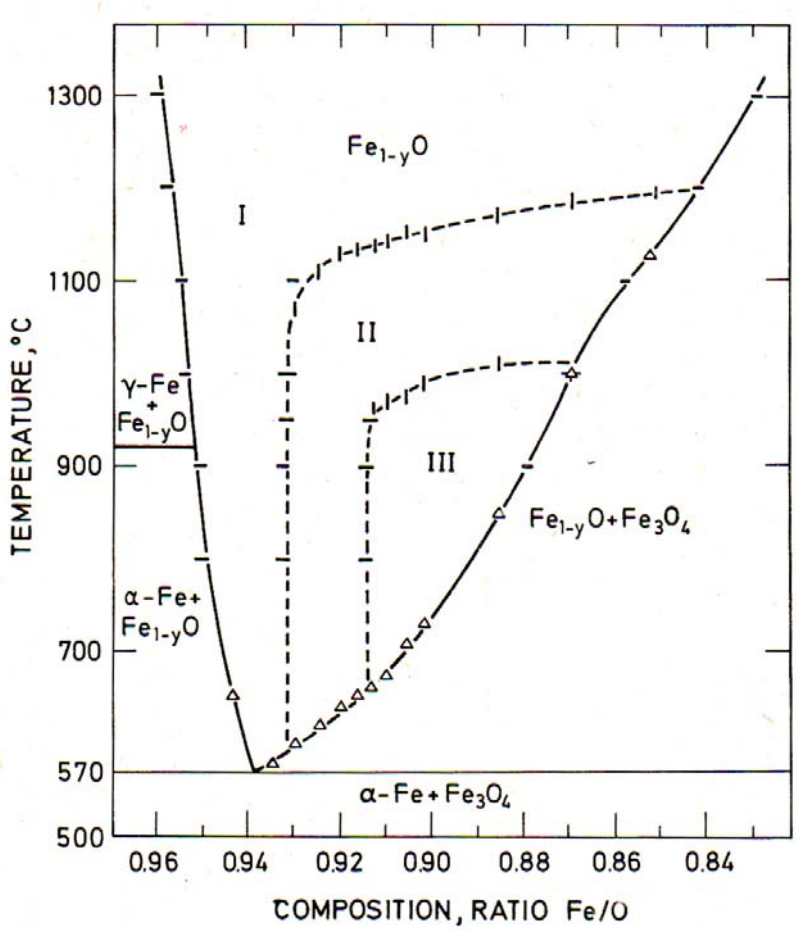

Fig. 2.6 Non-stoichiometry of FeO as a function of temperature [8].

2.4 Results

2.4.1 Cross section of Fe-Cr Alloy

Figure 2.7 shows typical cross sections of Fe-0.5Cr and Fe-17Cr alloys in dry and humid conditions at 1073 K. Internal oxides precipitate in alloy matrix of Fe-0.5Cr both in dry and humid environments. No external scale and grain boundary oxidation was observed on the sample. The internal oxidation was occurred uniformly through out the alloys without anomalous localized oxidation. The microstructure of internal oxide is similar both in dry and humid condition. On the other hand, Fe-17Cr alloy exhibits continuous external scale in both dry and humid conditions. Beneath the oxide scale, no precipitated internal oxides were observed.

Figure 2.8 shows cross sections of Fe-8Cr, -10Cr and -12Cr in oxidized dry and humid environments. Alloys with these Cr concentrations are expected to exhibit the transition from internal to external oxidation. In dry environment, continuous oxide scales (external oxidation) without internal oxidation are observed on the alloys with Cr concentration higher than 10 mass%. The thickness of external oxide is about 2 μm. On the other hand, IOZ in which oxides precipitate is observed in the alloy with Cr concentration lower than 8 mass%. The thickness of IOZ is about 5 μm. In humid environment, IOZ is observed on both Fe-10Cr and Fe-12Cr alloy.

Figure 2.9 shows various parts of cross section of Fe-8Cr and Fe-12Cr in dry and humid environments, respectively. The microstructures apparently show that internal oxidation and external oxidation occur simultaneously in one specimen, probably depending on the small difference of surface condition. Several parts of the samples show that internal oxide is formed beneath the continuous external scale (mixed oxide layer). The thickness of continuous scale is about less than 2 μm on both samples. Despite the difference in Cr concentration, both alloys exhibit almost an identical microstructure. These results indicated that the transition from internal oxidation to external oxidation occurred on Fe-8Cr in dry environment, while the transition took places on Fe-12Cr alloys in humid.

Figure 2.10 summarizes the mode of oxide morphology of Fe-Cr alloys in dry and humid conditions. Kodama [10] results of Fe-5Cr alloys are presented in the figure for reference. Kodama [10] did the oxidation experiment under the same conditions of this work. Higher Cr concentration, as such in Fe-17Cr alloy, exhibits an external oxidation on both samples in dry and humid conditions.

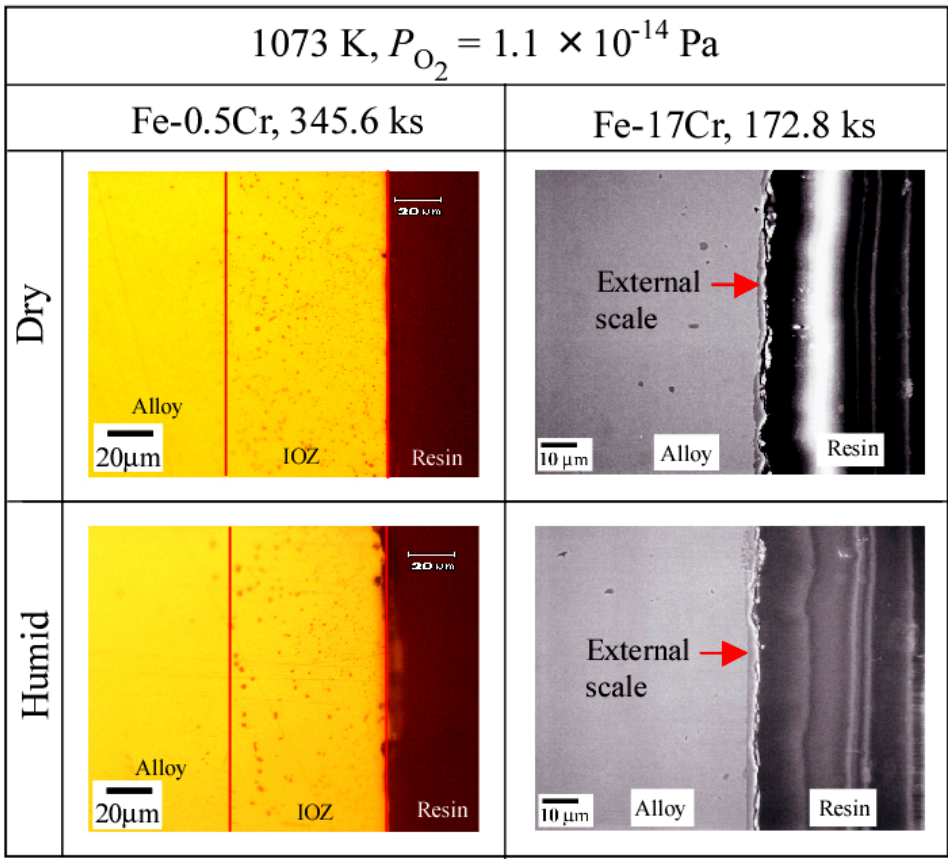

Fig. 2.7 Cross sectional micrograph of Fe-0.5Cr and Fe-17Cr alloys oxidized at 1072 K showing the formation of internal precipitated oxide and external scale, respectively in both alloys.

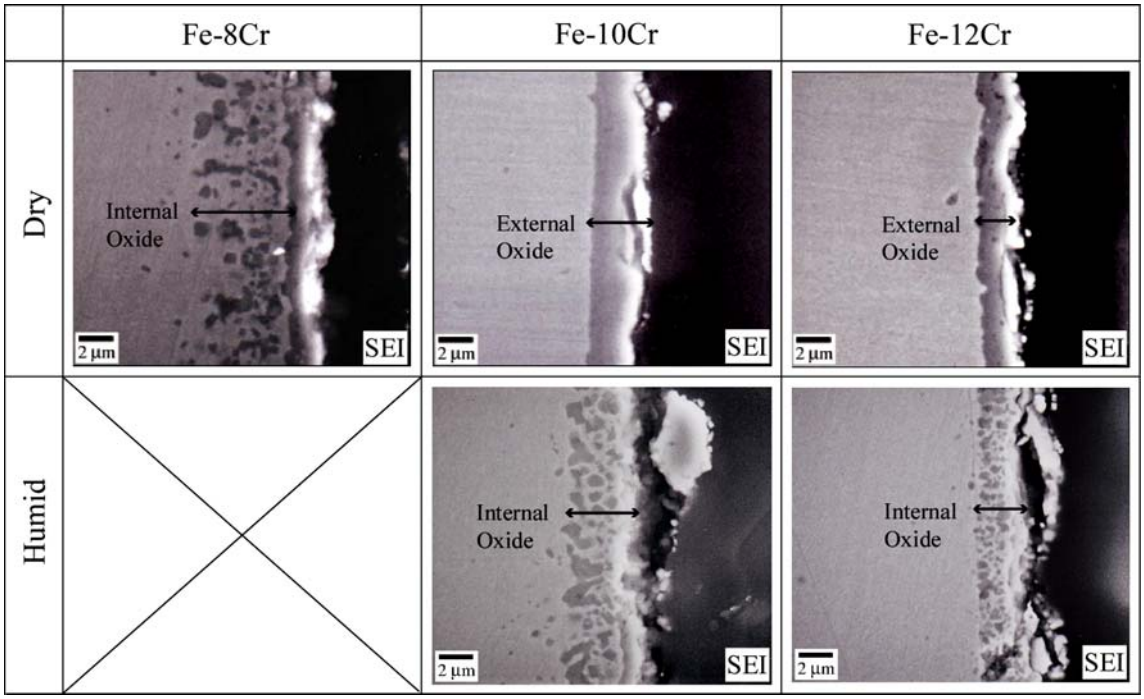

Fig. 2.8 Cross sectional micrograph of Fe-Cr alloys oxidized at 1072 K for 172.8 ks.

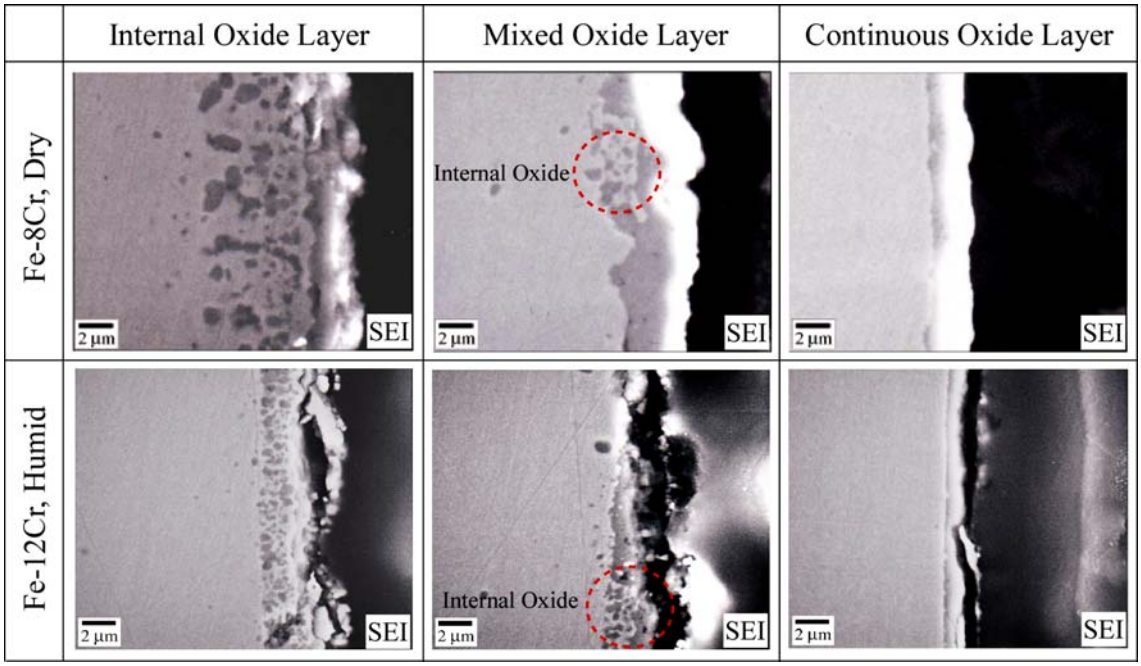

Fig. 2.9 Cross sectional micrograph of Fe-Cr alloys oxidized at 1072 K for 172.8 ks showing the simultaneous formation of internal oxide and external scale.

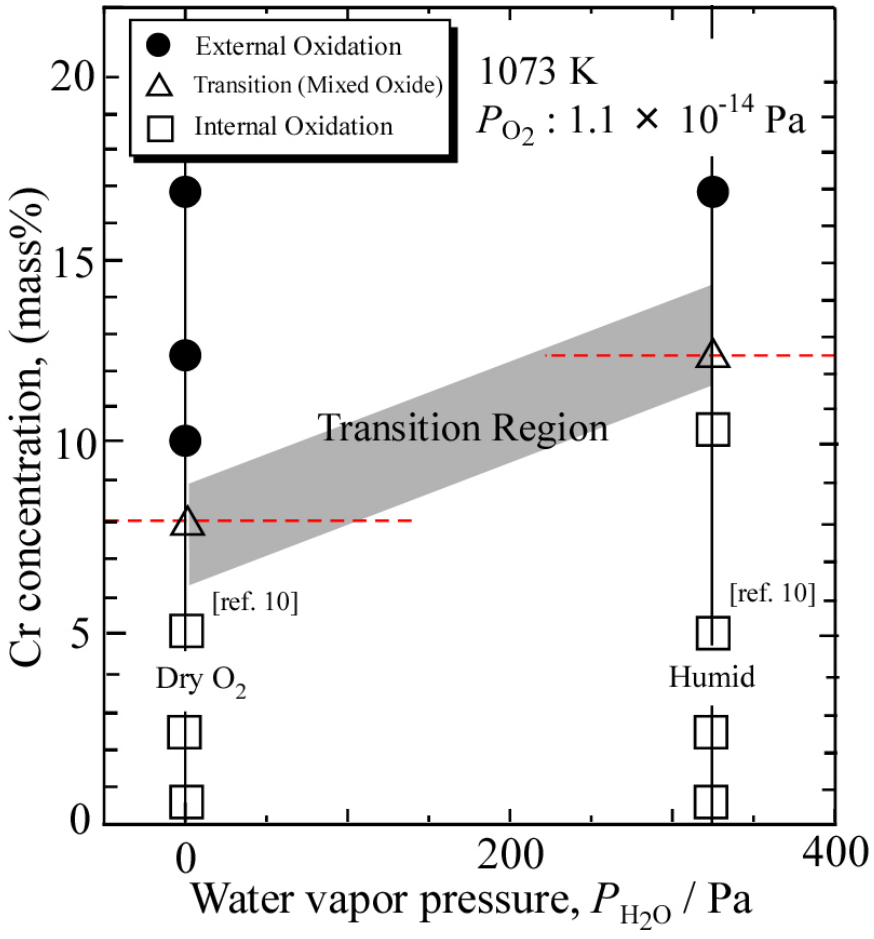

Fig. 2.10 Mode of oxidation of Fe-Cr alloys in dry and humid condition at 1073 K.

2.4.2 Oxidation Kinetic

Mass gain per unit area of the original sample is presented in Fig. 2.11 as a function of oxidation time. All the samples show rapid mass gain at the initial stage. The results show that the oxidation of the samples is following the parabolic rate law, which signifies that the diffusion of ion is the rate determining-step of the oxidation process.

The results show that all samples exposed in humid condition having higher mass change compared to the samples in dry environment. Mass gain of Fe-2.25Cr alloy is higher than that of Fe-0.5Cr alloy. Fe-2.25Cr shows the highest mass gain among the alloys, this shows that the internal oxidation was rapidly occurred in the alloy. Fe-0.5Cr shows a lowest mass gain among the alloys through out the oxidation time. Fe-17Cr alloys show lower mass gain at 172.8 ks compare to other alloys with Cr concentration of transition from internal to external (Fe-8~12Cr). This could be understood that relatively protective Cr_2O_3 scale was formed on the sample at this stage. Moreover, the mass gain of Fe-17Cr alloy gives almost constant value between sample oxidized at 172.8 ks and 691.2 ks. This shows that the protective Cr_2O_3 scale was formed even at earlier than 172.8 ks.

(a)

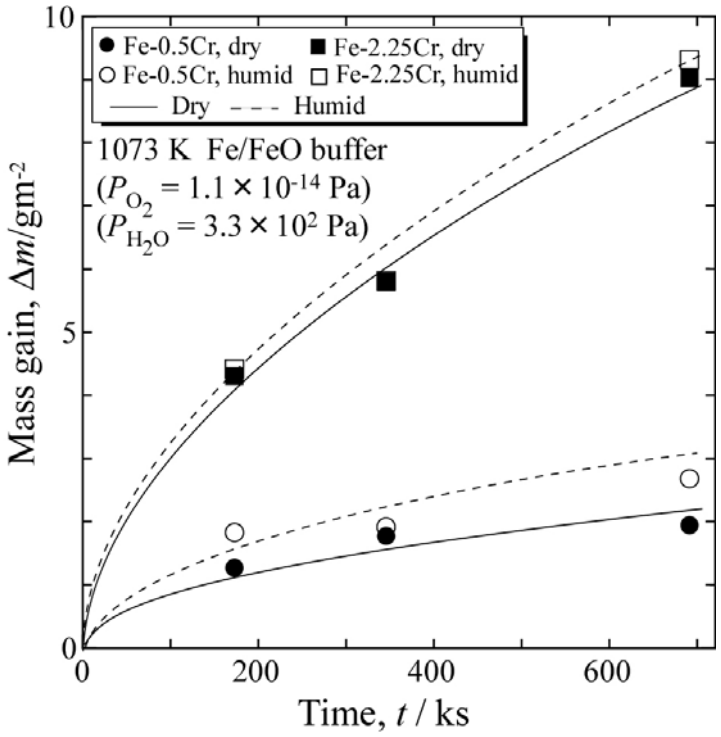

(b)

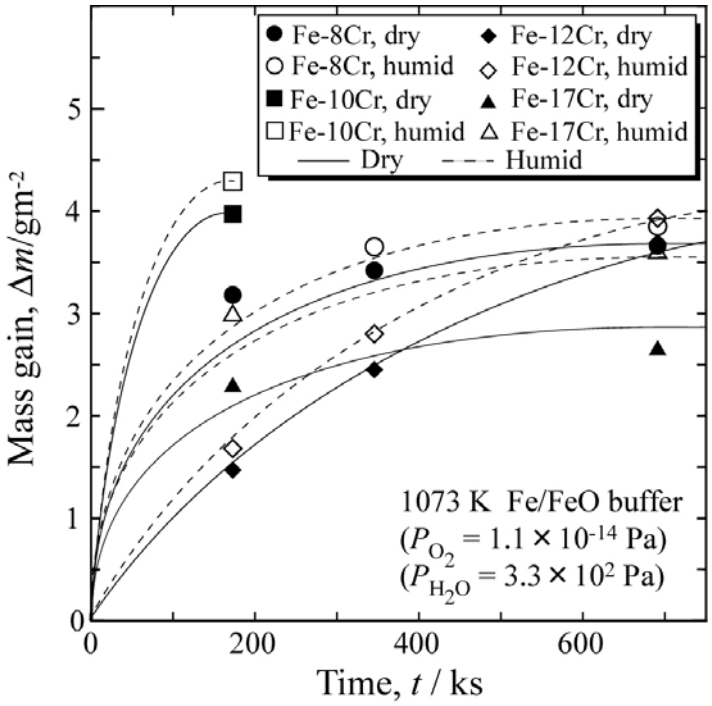

Fig. 2.11 Mass gain of the alloys, (a) Fe-0.5Cr and Fe-2.25Cr, (b) Fe-8~17Cr oxidized at 1073 K.

2.4.3 Phase identification

Figure 2.12 shows the XRD patterns of the sample surfaces oxidized in dry and humid conditions for 172.8 ks. The XRD patterns are similar both in dry and humid conditions. All samples show the peaks of α-Fe, which means that the oxide scales are thin enough for x-ray to penetrate into alloy substrate. Alloys with Cr concentration from 8 to 12 wt% formed $FeCr_2O_4$ and Cr_2O_3. The peaks of Cr_2O_3 are less intense than of $FeCr_2O_4$. The results of Fe-17Cr show only Cr_2O_3 was formed. Alloys that exhibit internal oxidation, such as Fe-0.5Cr and Fe-2.25Cr, only the peak of α-Fe was observed. This could be understands from the facts that the precipitated oxides particles are too small to be detected by the XRD.

Figure 2.13 presents the morphology of unpolished and polished (tilted by 2 degree) surfaces of an Fe-12Cr alloy in humid environment. Unpolished surface shows that the oxide structures are undulating with some coarse oxide particles (Fig. 2.12(a)). From the elemental analysis, it is clear that Cr and Fe are enriched at the surface. Oxygen also was detected at this surface. On the contrary, the polished surface shows that Cr and oxygen enriched in oxide scale (Fig. 2.12(b)). In some parts of the oxide, metallic Fe was observed in oxide close to the alloy due to uneven alloy/oxide interface. The intensity of Fe in the oxide decreases gradually from alloy/oxide interface toward the oxide scale. XRD results show that only Cr_2O_3 is detected at alloy/oxide interface.

From the results mentioned above, it is confirmed that the oxides at surface is $FeCr_2O_4$ and Cr_2O_3 scale is formed at the alloy/oxide interface.

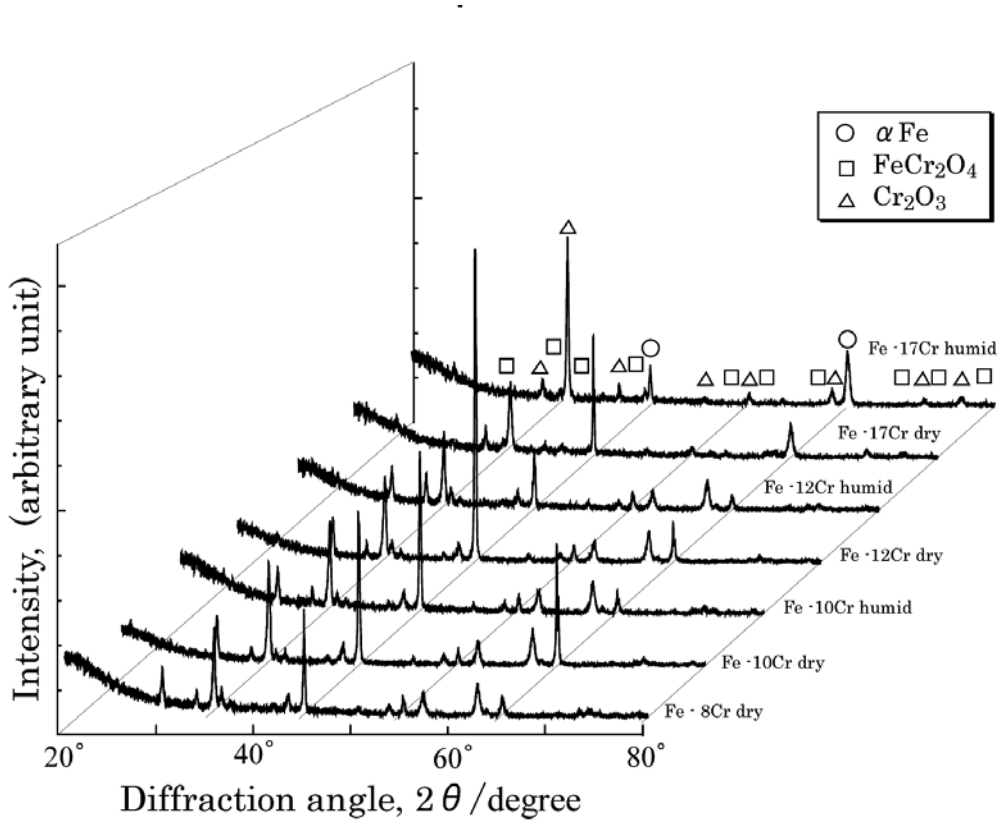

Fig. 2.12 XRD patterns of Fe-Cr alloys oxidized at 1073 K for 172.8 ks

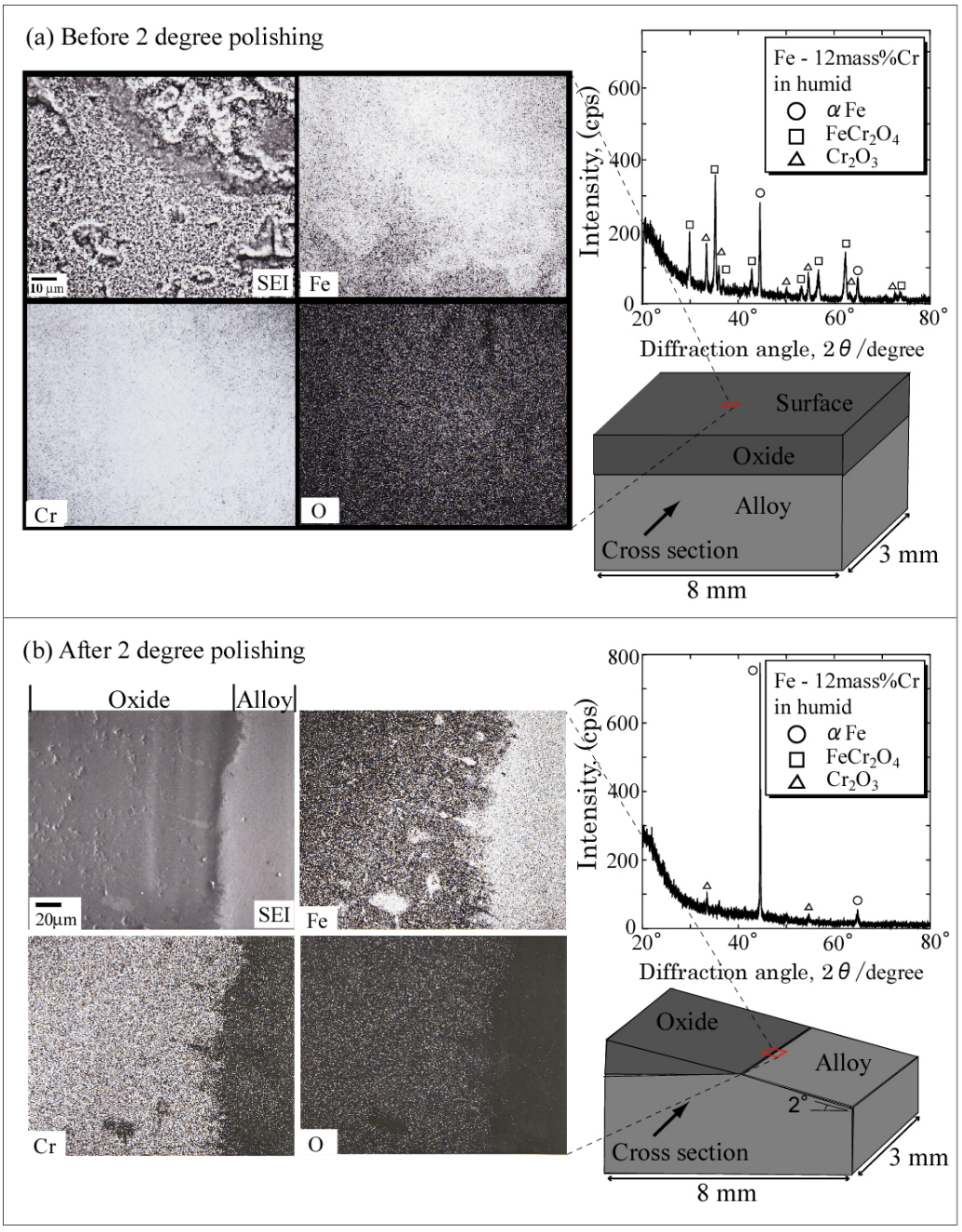

Fig. 2.13 Morphology of unpolished and 2 degree polished Fe-12Cr oxidized in humid condition and their XRD results.

2.5 Discussion

2.5.1 Transition from internal to external scale

Equation (2.2) shows the minimum concentration of Cr in Fe-Cr alloys to form external Cr_2O_3 scale. Cr concentration higher than this value will exhibit external scale, while below this value will form internal oxide. From the equation (2.2), it is clear that 2 variables may affect the minimum Cr concentration to form external scale, namely oxygen permeability in the alloy, $N_O^{(s)}D_O$ and interdiffusion coefficient of Cr in the alloy, D_{Cr}.

The ratio of minimum Cr concentration to form external scale in humid to dry condition could be derived from the equation (2.2). The ratio is shows in equation (2.5) as following.

$$\frac{N^*_{Cr(humid)}}{N^*_{Cr(dry)}} = \left[\frac{N_O^{(s)} D_{O(humid)}}{N_O^{(s)} D_{O(dry)}} \times \frac{D_{Cr(dry)}}{D_{Cr(humid)}} \right]^{\frac{1}{2}} \approx 1.5 \qquad (2.5)$$

where $N^*_{Cr(humid)}$ and $N^*_{Cr(dry)}$ is critical Cr concentration to form external scale in humid and dry condition, respectively. $N_O^{(s)} D_{O(humid)}$ is oxygen permeability in Fe-Cr alloy oxidized in humid condition, $N_O^{(s)} D_{O(dry)}$ is oxygen permeability in Fe-Cr alloy oxidized in dry condition. $D_{Cr(dry)}$ and $D_{Cr(humid)}$ is the diffusion coefficient of Cr in dry and humid condition, respectively.

The ratio of Cr concentration required to form external scale in humid to dry is about 1.5, which is evaluated from the fact that transition from internal to external oxidation occurs on Fe-8Cr and Fe-12Cr alloy in dry and humid condition, respectively.

Equation (2.5) clearly gives an explanation that higher Cr concentration is required to form external oxide in humid compared in dry condition is due to the change of oxygen permeability, $N_O^{(s)}D_O$ and/or Cr diffusion coefficient, D_{Cr} in the alloy. On other words, humidity somehow affects the transport mechanism of oxygen or/and the Cr. From this point of view, the effect of water vapor on the high temperature oxidation of Fe-Cr alloys can be quantitatively evaluated by measuring the change of oxygen

permeability and Cr diffusion coefficient in dry and humid condition.

2.5.2 Diffusion coefficient of Cr in α-Fe in dry and humid conditions

Cr diffusion in Fe base alloy has been studied extensively because of technological interest in high temperature kinetic processes. Oikawa [6] has reviewed lattice diffusion of various solute elements in Fe. Figure 2.14 illustrates diffusion coefficients of substitutional solutes in α-Fe and γ-Fe. The diffusion coefficient of substitutional solutes in α-Fe is a few magnitudes lower than the diffusion coefficient of oxygen in α-Fe. Oikawa [6] has shows the diffusion coefficient of Cr in α-Fe as a function of temperature as below.

$$D_{Cr} = 2.33 \times 10^{-4} \exp\ (-238.8 \text{kJmol}^{-1} / RT) \quad (2.6)$$

At 1073 K the diffusion coefficient of Cr in α-Fe is reported to be 5.5 x 10^{-16} m^2s^{-1}. In order to clarify which factor, i.e oxygen permeability or Cr diffusivity is responsible to the effect of water vapor as proposed in equation (2.5), it is important to verify the change of the parameters both in dry and humid condition. However, almost no work has been reported on the effect of water vapor on diffusivity of Cr. Kodama [10] has extensively study the diffusivity of Cr in α-Fe at 1073 K using Fe/Fe-16Cr diffusion couples in dry and humid condition. The diffusion couples was reacted up to 691.2 ks in vacuum for sample in dry condition and in Ar-20%H_2 mixed gas for samples in humid condition. The diffusion couples then was analyzed using point analysis of EPMA. Figure 2.15 shows the calculated diffusion coefficient of Cr at 1073 K as a function of Cr concentration. Kodama [10] has shown that the results are in conformity with the results of Oikawa [6], with the value of Cr diffusion coefficient is scattered from 8 x 10^{-16} m^2s^{-1} to 10 x 10^{-16} m^2s^{-1}. Moreover, it has shows that no significant difference between the diffusion coefficient of Cr in dry and humid condition.

From the works of Kodama [10] and compiled data of Oikawa [6], it could be concluded that the effects of dissolved hydrogen arised from water vapor on Cr diffusivity in α-Fe is negligible. The ratio of Cr diffusion coefficient in dry condition to

humid condition in equation (2.5) is nearly unity. The equation (2.5) could be rewrite as below.

$$\frac{N^{*}_{\mathrm{Cr(humid)}}}{N^{*}_{\mathrm{Cr(dry)}}} = \left[\frac{N^{(s)}_{\mathrm{O}} D_{\mathrm{O(humid)}}}{N^{(s)}_{\mathrm{O}} D_{\mathrm{O(dry)}}} \right]^{\frac{1}{2}} \approx 1.5 \qquad (2.7)$$

It is clear from the equation (2.7) that the increase of the critical Cr concentration to form external Cr_2O_3 scale in humid condition compared to dry condition is solely due to the increase of oxygen permeability in α-Fe in the presence of water vapor. How the water vapor enhances the oxygen permeability is the keyword to understand the effect of water vapor.

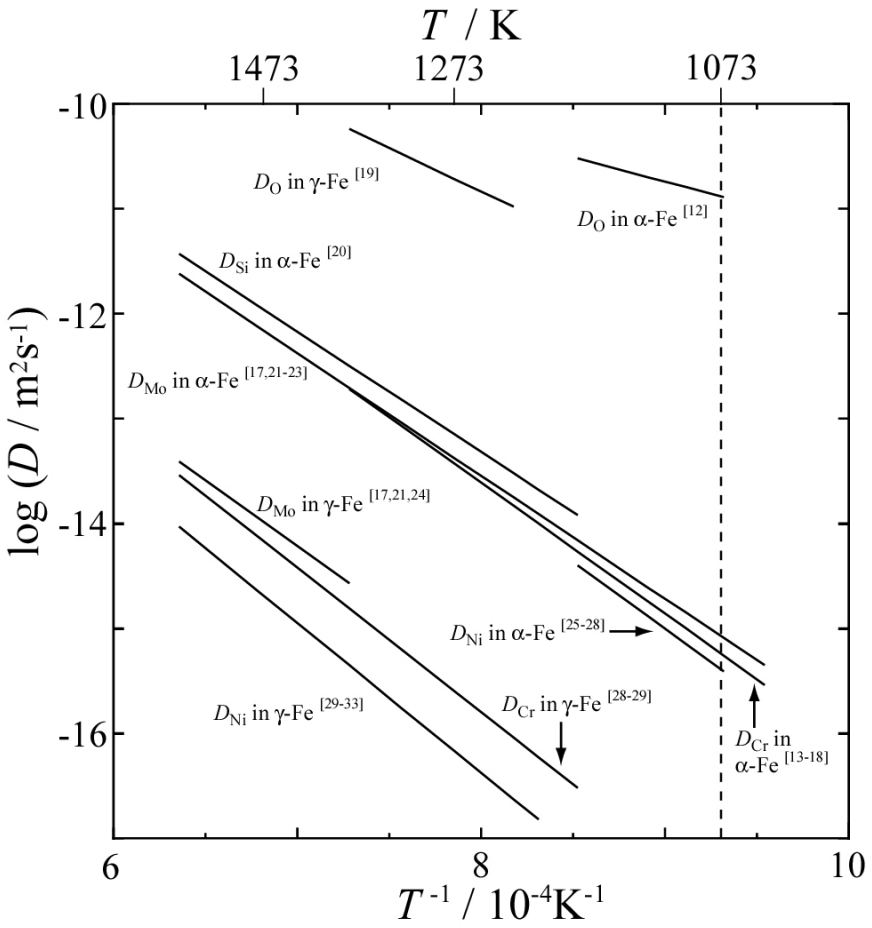

Fig. 2.14 Diffusion coefficient of substitutional solutes in α-Fe and γ-Fe [6].

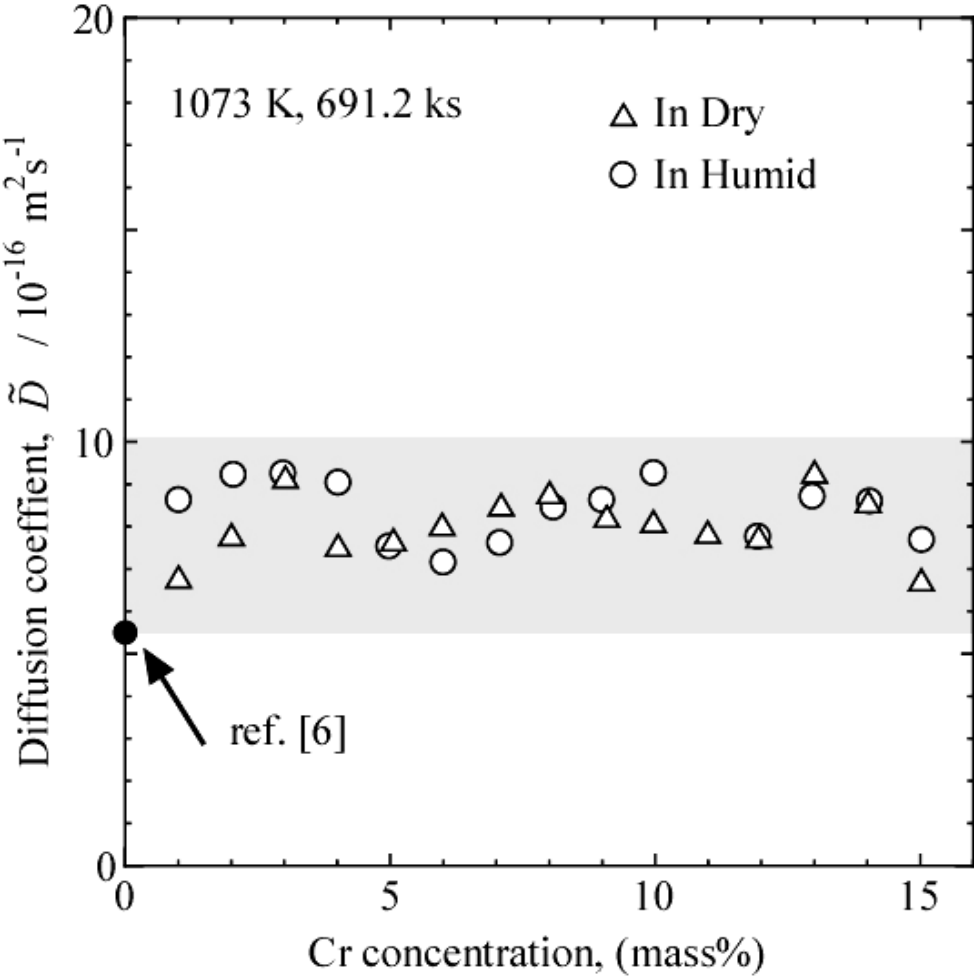

Fig. 2.15 Diffusion coefficient of Cr in dry and humid conditions at 1073 K as a function of Cr concentration [10].

2.6 Conclusion

The oxidation of Fe-0.5~17 wt% Cr alloys were investigated in dry and humid environment with oxygen partial pressure of 1.1×10^{-14} Pa, and water vapor pressure of 3.3×10^{2} Pa. The oxidation rate of the samples in humid condition is higher than in dry condition. The transition from internal to external oxidation occurs on Fe-8Cr and Fe-12Cr in dry and humid condition, respectively. The minimum Cr concentration required to form external scale is increase by 1.5 factor in humid condition compared to dry condition. The hydrogen in alloy, which is generated from water vapor may enhances the oxygen permeability in alloy.

References

[1] C. Wagner, *Zeitschrift für Elektrochemie*, **63** (7), 772-782 (1959).

[2] R. A. Rapp, *Acta Metallurgical*, **9**, 730 (1961).

[3] A. Atkinson, *Corrosion Science*, **22**(2), 87-102 (1982).

[4] J. H. Swisher and E. T. Turkdogan, *Transactions of the Metallurgical Society of AIME*, **239**, 426-431 (1967).

[5] J. Takada, S. Yamamoto, S. Kikuchi and M. Adachi, *Oxidation of Metals*, **25** (1/2), 93-105 (1986).

[6] H. Oikawa, *Tetsu to Hagane*, **68** (10), 1489-1497 (1982), In Japanese.

[7] T. Brylewski, T. Maruyama, M. Nanko and K. Przybylski, *Journal of Thermal Analysis and Calorimetry*, **55**, 681-690 (1999).

[8] Per Kofstad, *Nonstoichiometry, Diffusion, and Electrical Conductivity in Binary Metal Oxides*, Wiley-Interscience, (1972).

[9] I. Barin, *Thermochemical Data of Pure Substances*, VHC Publisher, Vol. **4**, (1991).

[10] T. Kodama, *Master Dissertation*, Tokyo Institute of Technology, 2006.

[11] J. Takada, S. Yamamoto, S. Kikuchi and M. Adachi, *Oxidation of Metals*, **25** (1/2), 93-105 (1986).

[12] J. Takada and M. Adachi, *Journal of Materials Science*, **21**, 2133-2137 (1986).

[13] A. M. Huntz, M. Aucouturier, P. Lacombe, *Compt. Rend. Acad. Sci.*, **C265**, p.554, (1967).

[14] L. V. Pavlinov, E. A. Isadzanov, V. P. Smirov, *Met. Metalloved.* , **25**, p.559, (1968).

[15] A. W. Huntz, P. Guiraled, M. Aucouturier, P. Lacombe, *Mem. Sci. Rev. Metall.*, **66**, p.85, (1969).

[16] A. W. Bowen, G. M. Leak, *Met. Trans.*, **1**, p.1695, (1970).

[17] P. J. Alberry, C. W. Haworth, *Met. Sci.*, **8**, p.407, (1974).

[18] V. P. Manaenkov, V. A. Lazarev, A. V. Kulemin, V. M. Golikov, *Izv. Akad. Nauk SSSR, Met.* **2**, p. 118, (1877).

[19] J. Takada, M. Adachi, M. Adachi, *J. Mater. Sci*. **19**, p. 3451, (1984).

[20] R. J. Borg, D. Y. F. Lai, *J. Appl. Phys*, **41**, p. 5193, (1970).

[21] J. L. Ham, *Trans. ASM*, **35**, p.331, (1945).

[22]J. Kugera, B. Million, K. Ciha, *Koc. Master*. , **7**, p.97, (1969).

[23] C. P. Heijwegen, G. D. Rieck, *Acta Met.* , **22**, p.1269, (1974).

[24] M. A. Karshtal, A. P. Mokrov, *Zaved. Lab*., **33**, p.827, (1967)

[25] R. J. Borg, D. Y. F. Lai, *Acta Met.* , **11**, p.861, (1963).

[26] K. Hirano, M. Cohen, B. L. Averbach, *Acta Met.* , **9**, p.440, (1961).

[27] A. D. Romig, Jr. J. I. Goldstein, J. I. Goldstein, *Met. Trans*., **12A**, p.243, (1981).

[28] D. B. Moharil, I. Jin, G. R. Purdy, *Met. Trans*., **5**, p.59, (1974).

[29] J. R. MacEwan, J. U. MacEwan, L. Yaffe, *Canad. J. Chem*., **37**, p.1626, (1959).

[30] T. Ustad, H. S ϕ rum, *Phys. Ttat. Sol. (a)*, **20**, p.285, (1973).

[31] J. I. Goldstein, R. A. Hanneman, R. E. Ogilvie, *Trans. Met. Soc. AIME*, **233**, p.812, (1965).

[32] M. Badia, A. Vignes, Compt. *Rend. Acad. Sci*., **C264**, p.1582, (1967).

[33] G. Henry, G. Cizeron, *Ann. Chim(Paris)*, **3**, p. 167, (1978).

Chapter 3

Oxygen permeability in internal oxidation zone of Fe-Cr alloys at 1073 K under dry and humid conditions

3.1 Introduction

In Chapter 2, it was discussed based on Wagner [1] treatment of binary alloys oxidation and showed that water vapor significantly affects the oxygen permeability in α-Fe, which leads to higher oxidation rates in water vapor environment. Many works have been done to investigate the oxygen permeability in dry condition, however no work has been reported on the increase of oxygen permeability in humid condition. In this chapter, Fe binary alloys with dilute Cr concentration were oxidized in dry and humid environment under same oxygen partial pressure of Fe/FeO mixed powder as a buffer at 1073 K. The changes of oxygen permeability both in dry and humid environment was investigated.

3.2 Experimental Procedure

3. 2. 1 Sample preparation

The Fe-0.5 and 2.25 wt% Cr binary alloys were prepared by argon-arc melting of Fe (99.99%) and Cr (99.9%). The alloy ingots were homogenized at 1373 K in vacuum for 86.4 ks. Then, the alloys were sliced into coupons of 1 mm thick and grounded to 2000-grit finish using SiC abrasion paper. The samples were then finally polished with 4 μm diamond paste, followed by cleaning in ethanol with ultrasonic agitation.

Chemical composition and phases in the alloys were analyzed using Electron Probe Micro Analyzer (EPMA) and x-ray diffraction (XRD). The chemical compositions of Fe-Cr alloys are shown in Table 3.1. The samples were confirmed to be a single phase of α-Fe solid solution.

Table 3.1 The Chemical composition of the Fe-Cr alloys analyzed using EPMA.

Alloys	Fe Concentration		Cr Concentration	
	mass %	mole %	mass %	mole %
Fe-0.5Cr	99.51	99.51	0.49	0.49
Fe-2.25Cr	97.76	97.76	2.24	2.24

3. 2. 2 Internal oxidation of Fe-Cr alloys

Figure 3.1 shows the experimental setup. The sample was placed in an airtight apparatus. Two R-type thermocouples were placed at the top and bottom of the sample to monitor the temperature. The distance between sample and thermocouple is about 5 mm. The isothermal zone is 30 mm range with temperature fluctuates ± 0.5 K.

The oxidation procedure is the same as described in 2.3.2. The samples were oxidized in Fe/FeO mixed buffer with oxygen partial pressure of 1.1×10^{-14} Pa. For the oxidation in dry environment, the apparatus was evacuated using a rotary pump for 1.8

ks and closed. The sample was heated to 1073 K and hold for 172.8 ks to 691.2 ks. For the oxidation in humid environment, the apparatus was evacuated, filled with Ar - 5% H_2 gas of 3 x 10^4 Pa and closed. The sample was heated to 1073 K and hold for 172.8 ks to 691.2 ks. The water vapor pressure is calculated to be 3.3 x 10^2 Pa. After oxidation, the samples were cooled to room temperature in the furnace.

After oxidation, cross section of the sample was examined and the depth of internal oxidation zone (IOZ) was measured. The depth of IOZ was measured randomly on both sides of the samples' surface for at least 75 readings of each sample. The mean value of the depth was determined. The oxygen permeability was determined from the parabolic rate constant, K_p of the samples.

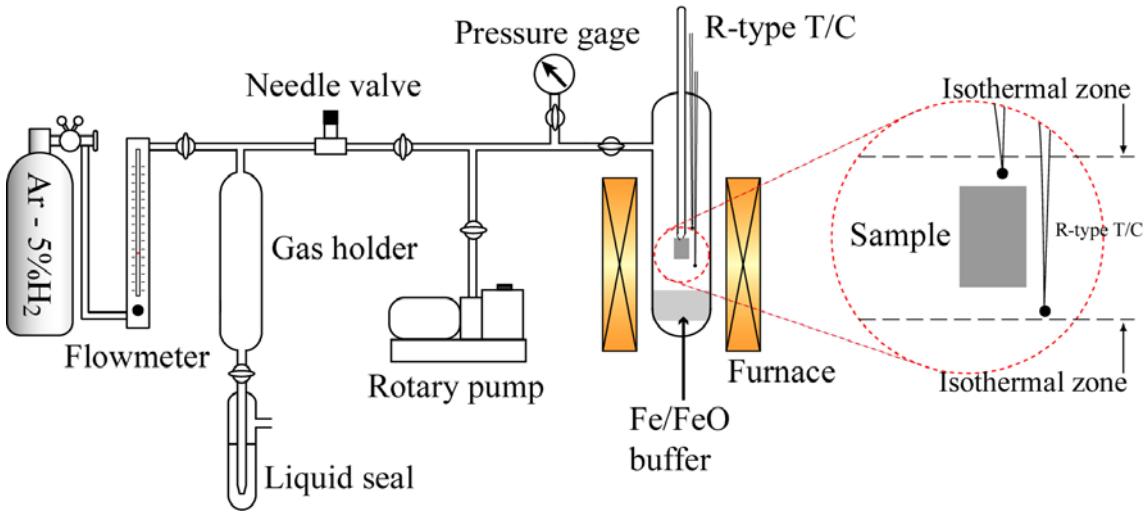

Fig. 3.1 Schematic diagram of the internal oxidation apparatus.

3.3 Results

3. 3. 1 Cross section

Figure 3.2 shows the optical microscope images of the internal oxide formed on Fe-Cr alloys in dry and humid condition for 691.2 ks. No grain boundary oxidation and anomalous localized oxidation were observed on the cross section of the samples.

Figure 3.3 shows the higher magnification of optical microscope image of Fe-0.5Cr and Fe-2.25Cr alloys in dry and humid condition for 345.6 ks. In dry condition, the oxide precipitates in Fe-0.5Cr is fine particles around 1 μm in size near the shallow sub-surface zone at the early stage of oxidation. However, in Fe-2.25Cr, the oxide precipitates is relatively larger and longer. The precipitated oxide grows towards the alloy/IOZ front. In humid condition, the size of oxides precipitates in Fe-0.5Cr is almost same as in dry condition. However, near the alloy/IOZ front, the oxide size increase by 2 times. The shape of precipitates oxides of Fe-2.25Cr is similar as in dry condition. The IOZ of Fe-0.5Cr is almost 1.5 times thicker than that of Fe-2.25Cr.

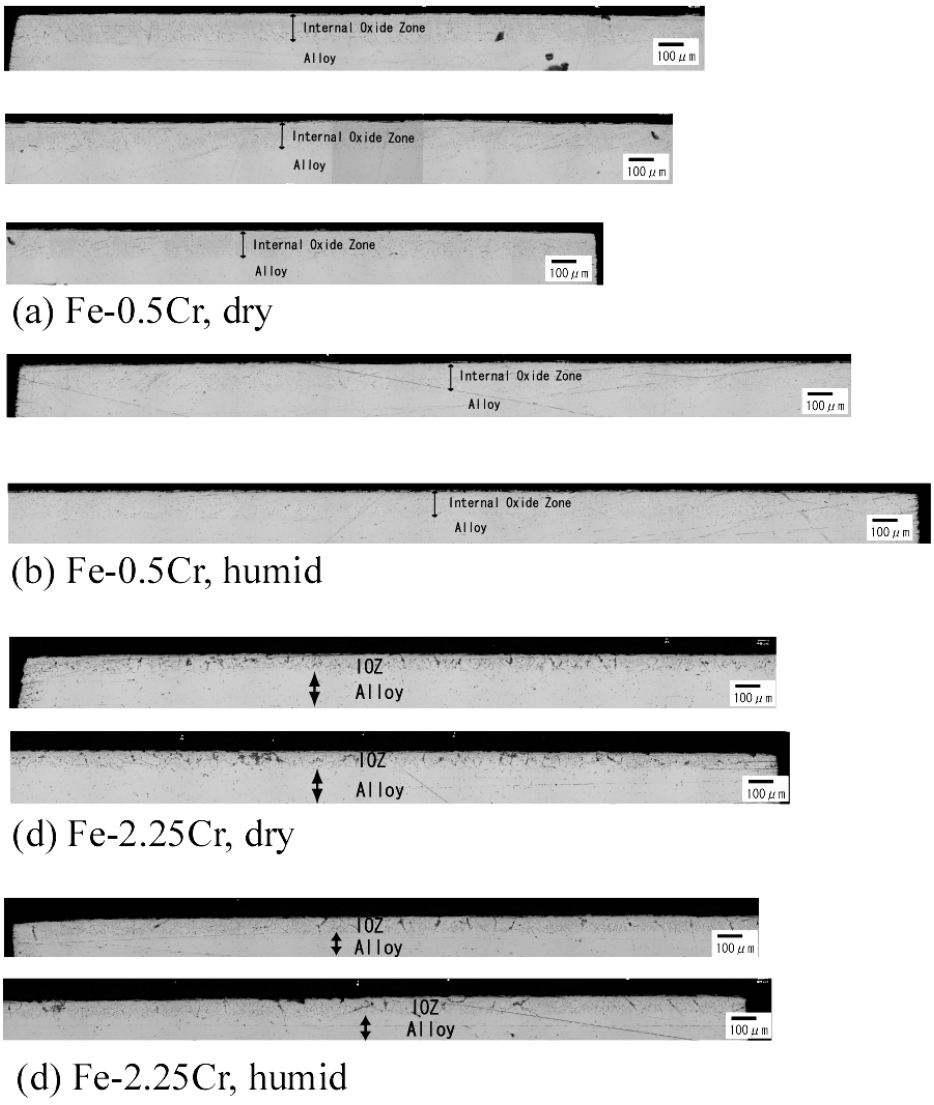

Fig. 3.2 Optical microscope images of the internal oxide formed on Fe-Cr alloys in dry and humid condition for 691.2 ks.

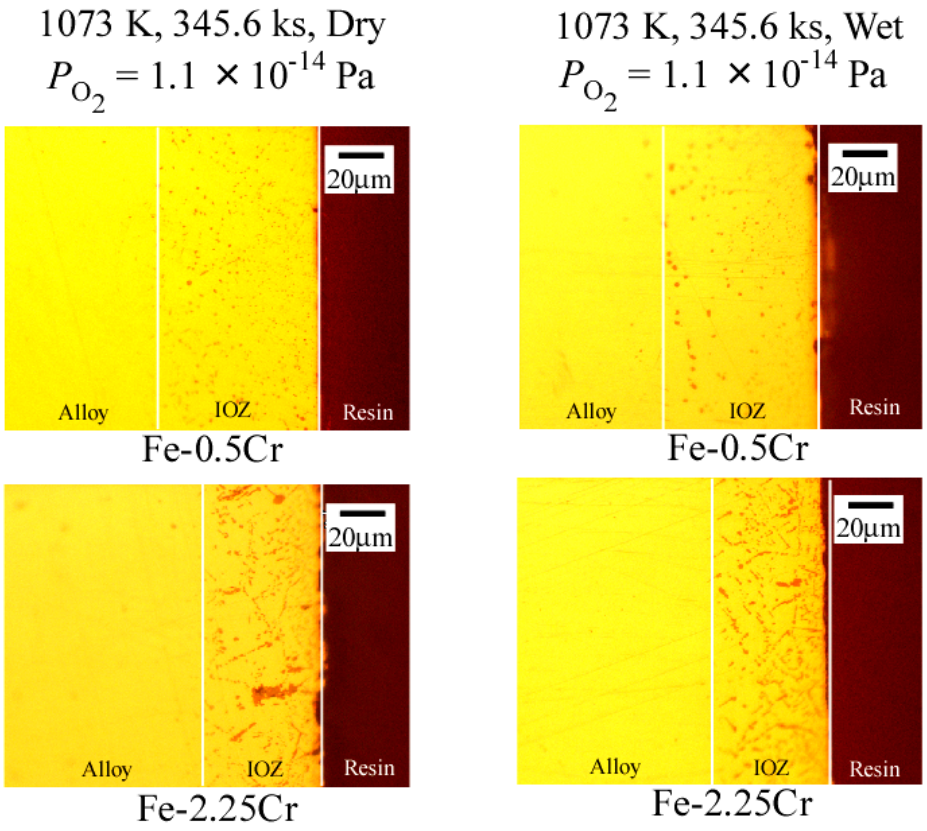

Fig. 3.3 Optical microscope image of Fe-0.5Cr and Fe-2.25Cr alloys in dry and humid condition for 345.6 ks.

3. 3. 2 Thickness of IOZ

Figure 3.4 shows the thickness of IOZ of Fe-0.5Cr and Fe-2.25Cr alloys oxidized in dry and humid condition as a function of the oxidation time. The growth of IOZ follows basically the parabolic rate law.

$$x^2 = 2K_p t \tag{3.1}$$

where x is the depth of IOZ, t is the oxidation time and K_p is the parabolic rate constant. The parabolic rate constant was determined from the slope of Fig. 3.5. The parabolic

rate constant of each sample is shown in Fig. 3.5. The K_p in the humid conditions is higher than in dry condition.

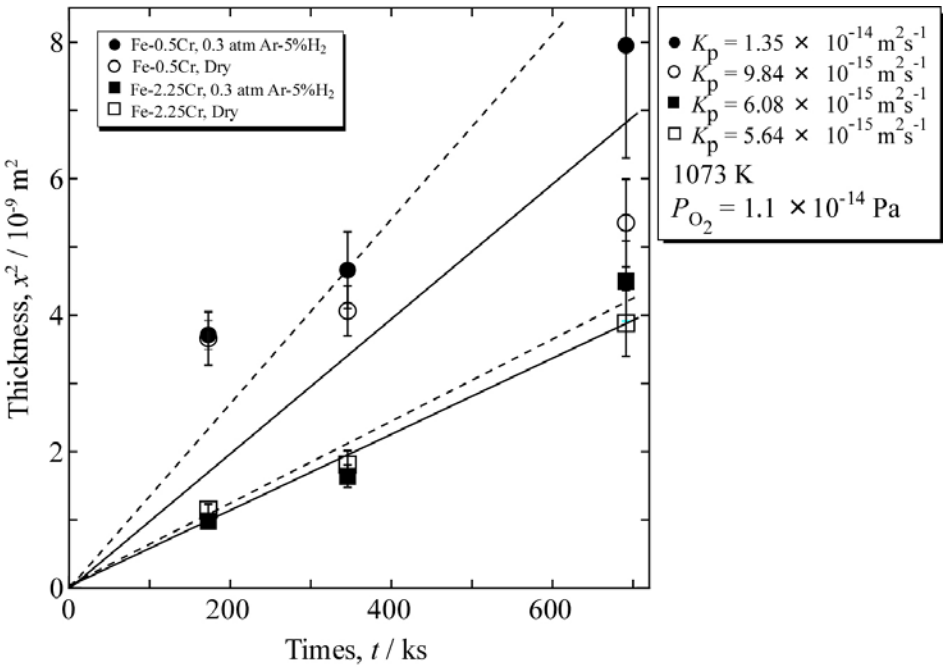

Fig. 3.4 Thickness of IOZ of Fe-0.5Cr and Fe-2.25Cr alloys oxidized in dry and humid condition as a function of the oxidation time.

3.4 Discussion

3. 4. 1 Oxygen permeability in α-Fe

The oxidation kinetics for growth of IOZ is parabolic, indicating that diffusion is the rate controlling process. Wagner [1] has proposed theoretical expression for the kinetics of internal oxidation.

$$x^2 = \frac{2N_O^{(s)}D_O}{\nu N_{Cr}}t \tag{3.2}$$

where N_{Cr} is the original concentration of Cr. From equations (3.1) and (3.2), it is well understood that the parabolic rate constant, K_p is proportional to the oxygen permeability, $N_O^{(s)}D_O$. In this way, the permeability of oxygen in α-Fe in dry and humid condition could be determined. Figure 3.5 shows the oxygen permeability as a function of Cr concentration. Kodama [2] has measured the oxygen permeability in Fe-5Cr under similar condition of this work. The data by Kodama [2] is included in Fig. 3.5. The oxygen permeability increases with the increase of Cr concentration.

Figure 3.6 shows the plot of log (N_OD_O/ms^{-2}) versus log (N_{Cr}/mol%). The plot shows linear lines with a slope of 2/3 both for dry and humid condition. From the value of slope, the oxygen permeability is plotted as a function of $N_{Cr}^{2/3}$ as shown in Fig. 3.7. The linear lines of the plot pass through origin when the Cr concentration is zero.

The critical Cr concentration to form external Cr_2O_3 scale is stated in the equation (2.2). Since the Cr concentration is only depends on the oxygen permeability, the equation (2.2) could be written as below.

$$N_{Cr\,(External)}^{*} \geq \left[AN_O^{(s)}D_O \right]^{\frac{1}{2}} \tag{3.3}$$

where A is independent of the concentration of Cr shown below.

$$A = \left[\frac{\pi g^{*} V_{Alloy}}{2\upsilon D_{Cr} V_{CrO_{1.5}}} \right] \tag{3.4}$$

From the Fig. 3.7, the dependency of oxygen permeability to Cr concentration in dry and humid could be showed as following

$$(N_O^{(s)} D_O)_{(dry)} = b_{dry} N_{Cr}^{2/3} \quad (3.5)$$

$$(N_O^{(s)} D_O)_{(humid)} = b_{humid} N_{Cr}^{2/3} \quad (3.6)$$

where b_{dry} and b_{humid} is the slope in dry and humid respectively. Equations (3.5) and (3.6) are substituted in equation (3.3). The critical Cr concentration from the Wagner equation may be describes as function of added Cr in the alloy. The modified equations of critical Cr concentration in dry and humid, respectively are showed as following.

$$N^*_{Cr\ (External)(dry)} \geq \left[Ab_{dry} N_{Cr}^{2/3} \right]^{\frac{1}{2}} \quad (3.7)$$

$$N^*_{Cr\ (External)(humid)} \geq \left[Ab_{humid} N_{Cr}^{2/3} \right]^{\frac{1}{2}} \quad (3.8)$$

Therefore, from the equations (3.7) and (3.8), the increase of Cr concentration to form external scale in humid is solely depend on the value of b. Equations (3.7) and (3.8) could be simplified and re-arranged as below.

$$N_{Cr}^2 \geq Ab N_{Cr}^{2/3} \quad (3.9)$$

Then, N_{Cr} could be showed as a simple function of A and b.

$$N_{Cr}^{4/3} \geq Ab \quad (3.10)$$

$$N_{Cr} \geq (Ab)^{3/4} \quad (3.11)$$

The increase of critical Cr concentration required to form external scale in humid condition could be showed as a ratio of b in dry and humid condition. The ratio is showed as following.

$$\frac{N^*_{Cr\ (External)(humid)}}{N^*_{Cr\ (External)(dry)}} = \left(\frac{b_{humid}}{b_{dry}} \right)^{3/4} \quad (3.12)$$

The values of b_{humid} and b_{dry} could easily determined from the Fig. 3.7, which is 3.75 x 10^{-15} m^2s^{-1} and 3.04 x 10^{-15} m^2s^{-1}, respectively. Calculation using equation (3.12) and respective b value shows that the ratio of Cr concentration to form external scale in humid environment increases by a factor of 1.2.

. The increase of oxygen permeability is always associated with fast-path for oxygen to diffuse such as along grain boundary and metal/precipitated oxide interfaces. In section 3.3.1, no grain boundary oxidation was observed. Thus, Figure 3.7 suggests that oxygen transport along the metal/precipitated oxide interfaces is further increased with the present of humidity by a factor of 1.2. This increases the critical Cr concentration need to form external scale.

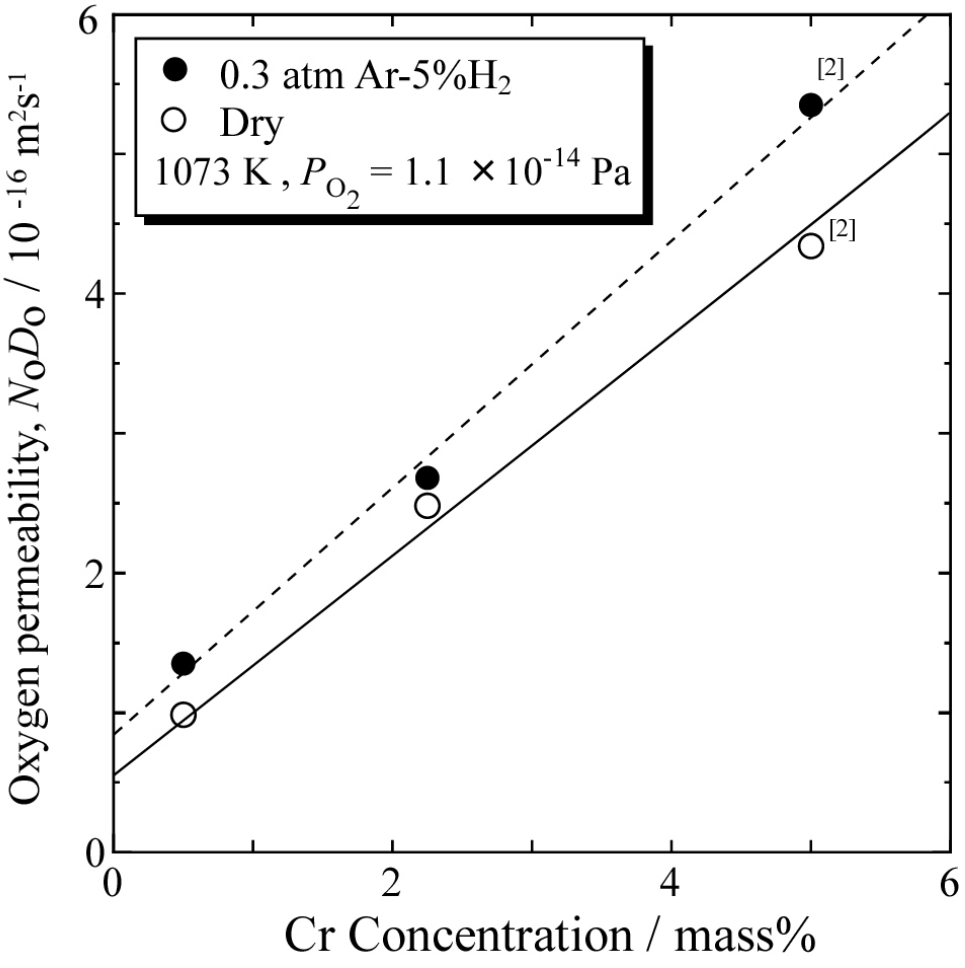

Fig. 3.5 Oxygen permeability as a function of Cr concentration in dry and humid condition at 1073 K.

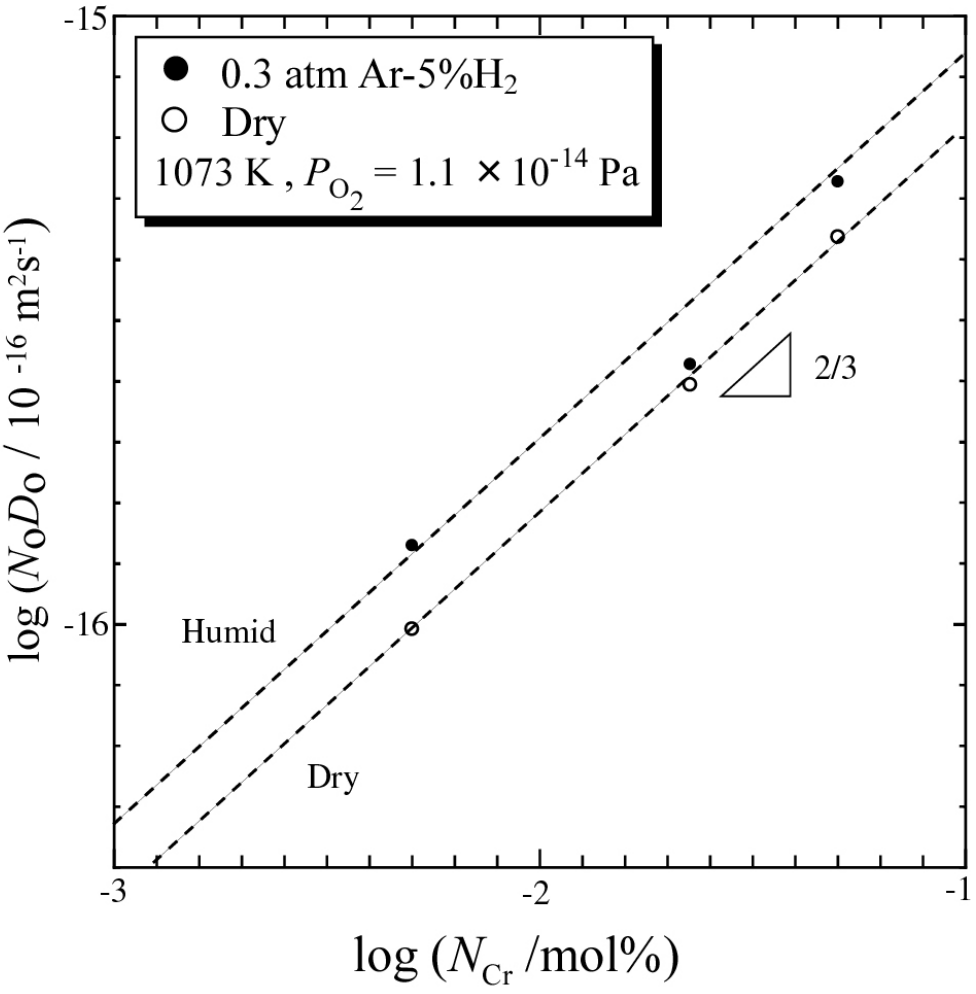

Fig. 3.6 Semi log plot of the oxygen permeability versus Cr concentration in dry and humid condition at 1073 K.

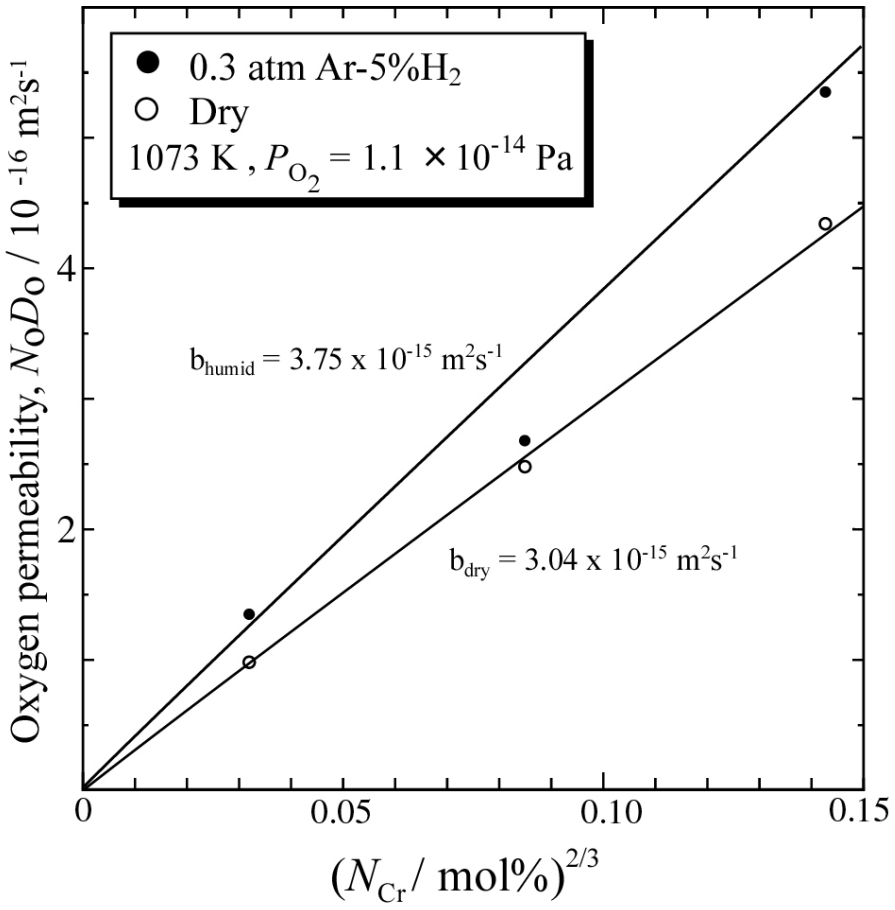

Fig. 3.7 Oxygen permeability as a function of Cr concentration, $(N_{Cr})^{2/3}$ in dry and humid condition at 1073 K.

3. 4. 2 Enhancement of oxygen transport

In the IOZ, oxygen could be transported through lattice alloy, alloy/precipitated oxide interface and oxide. The oxygen diffusivity in oxides such as $FeCr_2O_4$ and Cr_2O_3 is negligible compare to the diffusivity in lattice of α-Fe and along alloy/precipitated oxide interface. Thus, it is postulated that the enhancement of oxygen transport with the increase of the concentration of alloying element is due to the rapid diffusion of oxygen alloy/ precipitated oxide interface.

Kodama [2] has shown that the shape of oxide precipitates in Fe-5Cr alloy is changed from globular particles in dry to spike particles in humid condition. The cross section of Fe-5Cr [2] is shown in Fig. 3.8. The oxide morphology changes to spike particle, and it increase the IOZ thickness. This is clear evidence that water vapor affects the oxygen transport along the alloy/precipitated oxide interface. However, the mechanism on how water vapor enhances the oxygen transport along alloy/precipitated oxide interface is still unknown and need further investigation.

Many works has been done in dry condition to investigate the enhancement of oxygen diffusivity along the alloy/precipitated oxide interface in IOZ [3–12]. Figure 3.9 is a schematic diagram of internal oxide morphology of Fe and Ni base alloys with dilute Al or Cr content in Fe/FeO pack (Fe base alloys) and Ni/NiO pack (Ni base alloys). Under identical oxidation condition (i.e same oxygen partial pressure and solute atom concentration), a very different morphology was observed. In Fe-Al and Ni-Al alloys, the internal oxide grew perpendicular to the alloy/IOZ front. The oxide grew continuously from the surface to alloy/IOZ front with rod-like shape. This type of oxide shape enhances the oxygen diffusivity in alloy/precipitated oxide interface. However, in Fe-Cr and Ni-Cr alloys, the oxide is relatively coarser and more spherical. The oxide forms was discrete particle dispersed throughout the IOZ.

Above studies show that the morphology of precipitated oxide is various depends on the alloy system, and cannot be predicted easily. No systematic work has been done to explain and understand the change of oxide morphology from one alloy system to the other. Understanding this subject is important to pave the way to

quantitatively explain how water vapor affects the oxygen transport along metal/precipitated oxide interfaces.

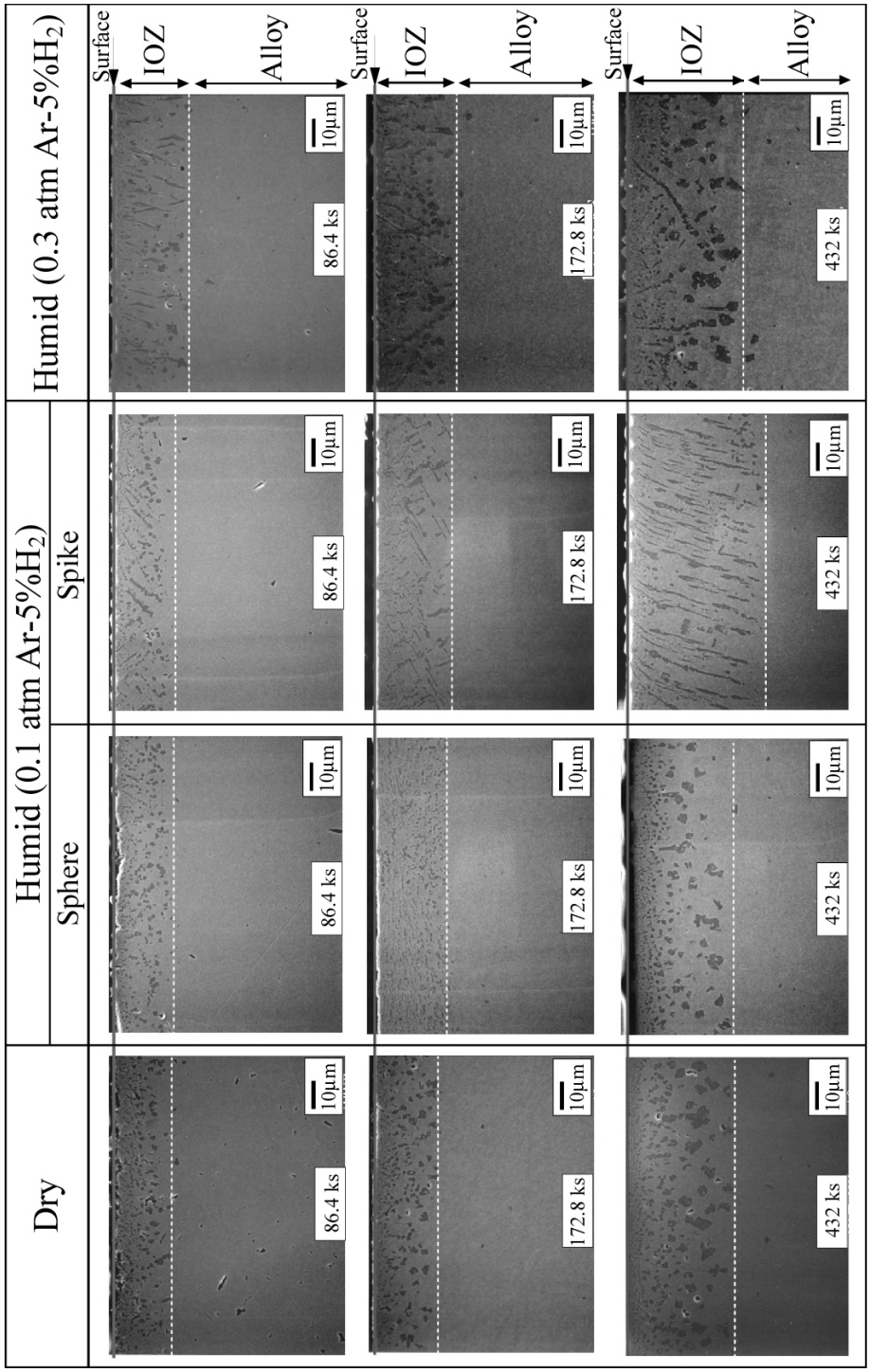

Fig. 3.8 Cross section of Fe-5Cr in dry and humid condition at 1073 K from the work of Kodama [2].

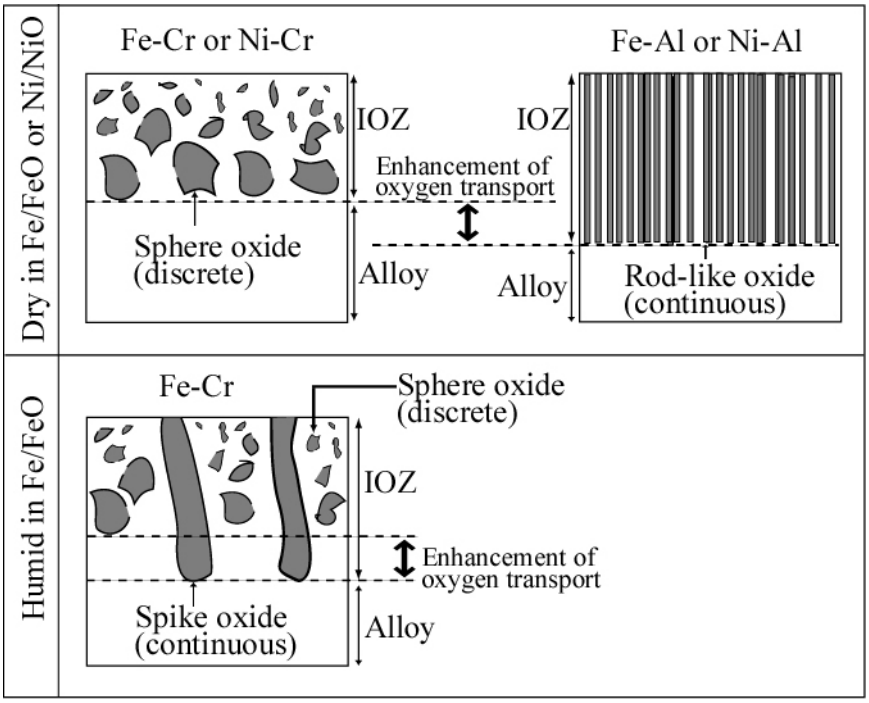

Fig. 3.9 Schematic diagram of internal oxide morphology of Fe and Ni base alloys with dilute Al or Cr content.

3.5 Conclusion

The internal oxidation of Fe-0.5 wt%Cr and Fe-2.25 wt%Cr alloys were investigated in dry and humid environment with oxygen partial pressure of 1.1×10^{-14} Pa, and water vapor pressure of 3.3×10^{2} Pa. Water vapor enhances the oxygen transport along the metal/precipitate oxide interface. The increase of oxygen permeability increases the critical Cr concentration to form external scale in humid condition by 1.2 times.

References

[1] C. Wagner, *Zeitschrift für Elektrochemie*, **63** (7), 772-782 (1959).

[2] T. Kodama, *Master Dissertation*, Tokyo Institute of Technology, 2006.

[3] J. Takada, S. Yamamoto, S. Kikuchi and M. Adachi, *Metallurgical Transactions A*, **17A**, 221-229 (1986).

[4] J. Takada, S. Yamamoto, S. Kikuchi and M. Adachi, *Oxidation of Metals*, **25** (1/2), 93-105 (1986).

[5] J. Takada and M. Adachi, *Journal of Materials Science*, **21**, 2133-2137 (1986).

[6] S. Hayashi and T. Narita, *Nippon Kinzoku Gakkai Shi*, **63** (9), 1204-1211 (1999). In Japanese.

[7] F. H. Stott, G. C. Wood, D. P. Whittle, B. D. Bastow, Y. Shida and A. Martinez-Villafane, *Solid State Ionics*, **12**, 365-374 (1984).

[8] D. P. Whittle, Y. Shida, G. C. Wood, F. H. Stott, B. D. Bastow, *Philosophical Magazine A*, **46** (6), 931-949 (1982).

[9] F. H. Stott and G. C. Wood, *Materials Science and Technology*, **4**, 1072-1078 (1988).

[10] H. C. Yi, S. W. Guan, W. W. Smeltzer and A. Petric, *Acta Metallurgica et Materialia*, **42** (3), 981-990 (1994).

[11] S. Goto and S. Koda, *Nippon Kinzoku Gakkai Shi*, **34** (3), 319-326 (1970). In Japanese.

[12] S. Goto and S. Koda, *Nippon Kinzoku Gakkai Shi*, **34** (3), 326-332 (1970). In Japanese.

[13] N. Birks, G. H. Meier and F. S. Pettit, *Introduction of the High Temperature Oxidation of Metals*, Cambridge University Press, (2006).

Chapter 4

Measurement of surface oxygen potential on Fe-Cr alloys in dry and humid conditions

4.1 Introduction

It was clear from chapter 2 and 3 that the presence of water vapor in oxidation environment enhances the oxygen transport along the precipitates oxide/metal interface. This explains the reason of accelerated oxidation rates and anomalous oxidation behavior in water vapor condition. In industries, various ferritic Cr alloys were used with small amount of alloying elements as shown in Table 1.1. Moreover, the alloys are subjected to wide-range of oxidation condition. Therefore, the oxidation resistance of the alloys cannot be solely determined by mass gain in isothermal oxidation. Evaluation of the oxidation resistance of an alloy is always required a laborious and time-consuming efforts.

It is imperative to develop an in-situ method to continuously monitoring of the formation of protective scale. Akiba et. al [1] have successfully monitor the oxygen chemical potential on growing oxide scales during high temperature oxidation of Fe, Ni and Co at 1373 K. The authors have showed that in case of oxidation kinetic is controlled by diffusion in the scale (parabolic rate law) as such on NiO and CoO scale, the surface chemical potential is almost identical to that in the atmosphere. The schematic illustration of the chemical potential distribution in and outside scale is showed in Fig. 4.1. However, if the oxidation kinetic is controlled by surface reaction

(linear rate law) as such on FeO scale, a boundary layer is developed and the surface oxygen chemical potential is much lower than in the atmosphere Fig. 4.1(b).

In chapter 2, it is clear that the formation of protective scale is affected by water vapor. The Cr concentration needed to form external scale is increase from 8 wt% in dry to 12 wt% in humid condition. The objective of this study is to measure the surface oxygen potential on Fe-Cr alloys in dry and humid environment, and distinguish the formation of protective scale from non-protective scale at early stage of oxidation.

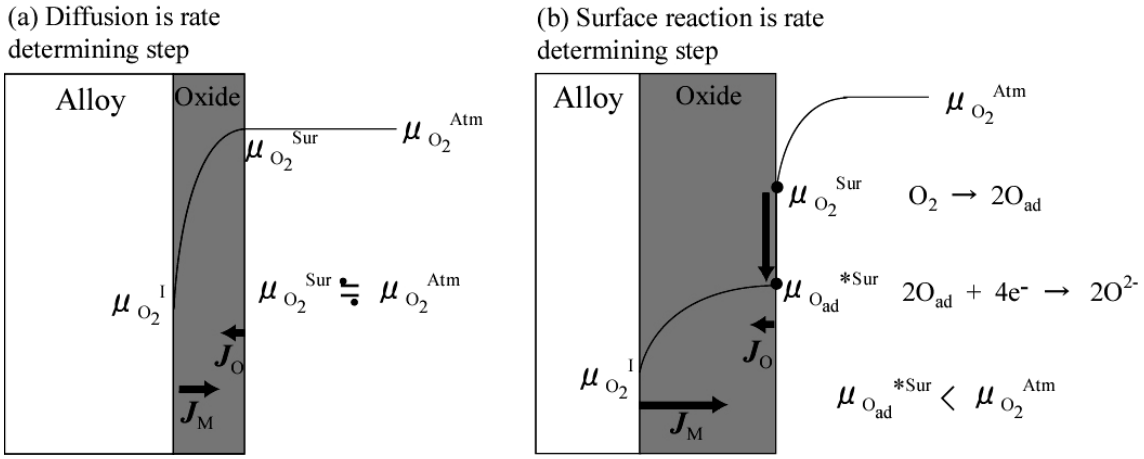

Fig. 4.1 Schematic diagram of potential distribution of oxygen in oxide scale.

4.2 Principle of measurement

Calcia-stabilized zirconia (CSZ) is well known as an ionic conductor, and is widely used as solid electrolyte in oxygen sensor / pump at high temperature. Figure 4.2 shows a schematic diagram of an oxygen sensor using CSZ as an electrolyte. If one side of oxygen partial pressure, $P_{O_2}^{I}$ is known value, the oxygen partial pressure in the other side, $P_{O_2}^{II}$ can be measured. The electromotive force (emf) of this cell is expressed as Nernst equation below.

$$E = \frac{\mu_{O_2}^{II} - \mu_{O_2}^{I}}{4F} = \frac{RT}{4F} \ln \frac{P_{O_2}^{II}}{P_{O_2}^{I}} \tag{4.1}$$

where *R*, *T* and *F* denote gas constant, temperature and Faraday constant, respectively. In this study, the surface oxygen potential on growing oxide scale was measured applying above principle.

Figure 4.3 (a) shows a schematic diagram of oxygen concentration cell for the measurement of surface oxygen potential. The cell is expressed as below

$$(-)\ \text{Pt}\ |\ \text{Metal}\ |\ \text{oxide scale, gas}(\mu^{*\text{Sur}}_{\text{O}_{ad}})\ |\ \text{CSZ}\ |\ \text{Pt, gas}(\mu^{\text{Atm}}_{\text{O}_2})\ (+) \qquad (4.2)$$

where $\mu^{*\text{Sur}}_{\text{O}_{ad}}$ and $\mu^{\text{Atm}}_{\text{O}_2}$ are chemical potentials of adsorbed oxygen atom at scale surface and of oxygen molecule in the atmosphere, respectively.

A sample was spot-welded with Pt wire is placed on CSZ that connected with Pt lead on the other side as shown in Fig. 4.3 (a). If the sample is exposed in oxidizing condition, oxide scale grows on the sample. In case of the growth of oxide scale is due to outward diffusion of metal ions, the tip of CSZ is embedded in the scale as shown in Fig. 4.3 (b). On the other hand, if the growth of oxide scale is due to inward diffusion of oxide ion, the CSZ tip is always contacting with the surface of the oxide scale as shown in Fig. 4.3 (c).

In the case that the oxide scale is an electronic conductor, it behaves itself as an electrode of the cell. Then, an electronic circuit is formed. The oxidation-reduction reaction of oxygen is mostly occurred at the triple phase boundary of CSZ, electrode (oxide scale) and gas phase. Accordingly, an emf is generated corresponds to the difference between oxygen potential on the oxide scale, $\mu^{*\text{Sur}}_{\text{O}_{ad}}$ and in the atmosphere, $\mu^{\text{Atm}}_{\text{O}_2}$. Anode reaction occurs on the oxide scale. First, the oxygen is adsorbed in the oxide scale and expressed as below.

$$\text{O}_2 \rightarrow 2\text{O}_{ad} \qquad (4.3)$$

Then, adsorbed oxygen is reacted with electron to become oxide ion as following.

$$2\text{O}_{ad} + 4\text{e}^- \rightarrow 2\text{O}^{2-} \qquad (4.4)$$

At the contact point of CSZ and Pt lead that located in the gas atmosphere. The reaction is expressed as below.

$$\text{O}_2 + 4\text{e}^- \rightarrow 2\text{O}^{2-} \qquad (4.5)$$

Applying the eq. (4.1) the emf of this cell could be written as

$$E_{\text{cell}} = \frac{\mu_{O_2}^{\text{Atm}} - 2\mu_{O_{ad}}}{4F} = \frac{\mu_{O_2}^{\text{Atm}} - \mu_{O_2}^{*\text{Sur}}}{4F} = \frac{RT}{4F} \ln \frac{P_{O_2}^{\text{Atm}}}{P_{O_2}^{*\text{Sur}}} \tag{4.6}$$

From this equation, oxygen potential on the oxide surface could be determined by measuring the E_{cell} and oxygen partial pressure at the atmosphere, $P_{O_2}^{\text{Atm}}$.

The possible rate determining steps of the growth of oxide scale are 1) diffusion of ions, and 2) surface reaction of oxygen. In the former case, the oxygen supply on the surface is fast enough compared to relatively slow ionic diffusion in the scale. This results in the surface oxygen potential to be almost equal to the atmosphere as schematically shown in Fig. 4.1(a). Thus, the emf is close to zero. The growth of protective scale of Cr_2O_3 is known be controlled by the diffusion of ions in the oxide scale. While in the latter case, oxygen is consumed rapidly on the scale surface as shown in Fig. 4.1(b). This results in a decrease of oxygen potential at the surface. The difference of oxygen potential between atmosphere and scale surface generates substantial amount of emf. The growth of non-protective scales such as iron oxides is known to be in this category. Therefore, by measuring the emf of the cell, the formation of protective scale could be distinguished from the non-protective scale at early stage of oxidation.

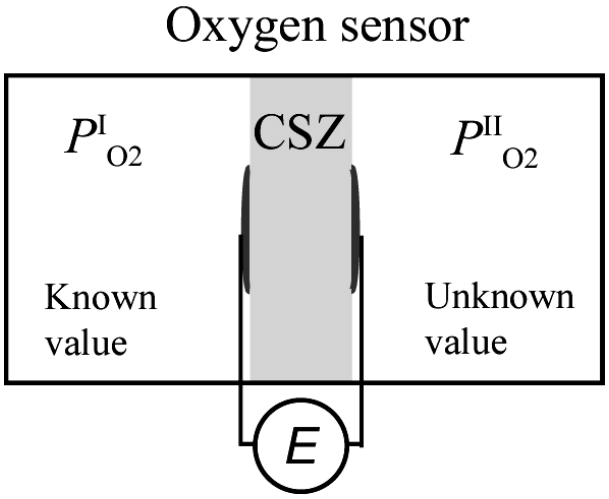

Fig. 4.2 Schematic diagram of an oxygen sensor.

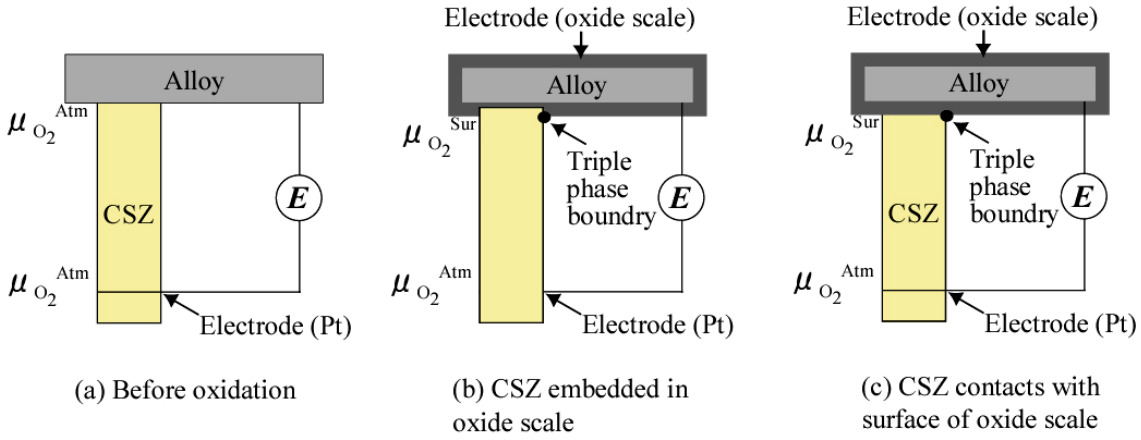

Fig. 4.3 Schematic diagram of oxygen concentration cell for the measurement of surface oxygen potential.

4.3 Experimental Procedure

4. 3. 1 Sample preparation

For experiment in dry condition, Fe (99.99%) plate purchased from Nilaco Corporation and Fe-5~22 wt% Cr was employed. Fe was cut into coupons of 10 mm x 5 mm x 1 mm. The Fe-5~17 wt% Cr binary alloys were prepared by argon-arc melting of the pure constituent metals of Fe (99.99%) and Cr (99.9%). The alloy ingots were homogenized at 1373 K in vacuum for 86.4 ks. Then, the alloys were cut into coupons of 10 mm x 5 mm x 1 mm. While Fe-22 wt%Cr steels was supplied by Hitachi Metal Co. The samples were grounded to 2000-grit finish using SiC abrasion paper, and finally polished with 4 μm diamond paste. Then, the samples were cleaned in ethanol with ultrasonic agitation.

For experiments in humid condition, arc melted Fe-5-17 wt%Cr alloys and Fe-22 wt%Cr steel was used in the experiment. The chemical composition of Fe-5~17 wt%Cr alloys and Fe-22 wt%Cr is shown in table 4.1 and 4.2 respectively.

Table 4.1 The chemical composition of the Fe-5~17 wt% Cr alloys analyzed using EPMA.

Alloys	Fe Concentration		Cr Concentration	
	mass %	mole %	mass %	mole %
Fe-5Cr	94.9	94.5	5.1	5.5
Fe-8Cr	91.8	91.2	8.2	8.8
Fe-10Cr	90.2	89.5	9.8	10.5
Fe-12Cr	87.5	86.7	12.5	13.3
Fe-17Cr	83.1	82.1	16.9	17.9

Table 4.2 The chemical composition of Fe-22 wt% Cr steels.

Element	C	Si	Mn	P	S	Ni	Cr	Al	Fe
Mass %	0.023	<0.01	0.01	0.004	0.002	0.01	21.93	0.01	Bal.

4. 3. 2 Emf measurement procedures

Figure 4.4 shows the schematic illustration of experimental apparatus and the setup of the oxygen concentration cell. The CSZ tube was cut into the shape as shown in Fig. 4.5, which has 3 legs to support a sample and ensure free gas flow. The 2 legs of the CSZ are coated with insulating materials of Al_2O_3 cement. This assures that oxidation-reduction of oxygen occurs only at one contact point between the CSZ and the sample. Moreover, in order to ensure that gas supply is enough at triple phase boundary, the surface area of CSZ tip that contacted with the sample was fabricated as small as possible. Figure 4.6 shows the optical microscope image of the CSZ tip. The area of the top of the leg is estimated around 0.0025 mm^2.

The platinum electrode detecting the oxygen potential in the atmosphere is attached 20 mm away from the sample. This makes sure that the detecting electrode is outside of gas boundary layer.

A CSZ oxygen sensor is located 5 mm below the cell to continuously monitor

the oxygen partial pressure in the atmosphere, $P_{O_2}^{Atm}$. The sensor measured the emf generated from the difference of oxygen partial pressure in the experimental apparatus and in the air. The emf of this oxygen sensor is expressed as

$$E_{sensor} = \frac{\mu_{O_2}^{Air} - \mu_{O_2}^{Atm}}{4F} = \frac{RT}{4F} \ln \frac{P_{O_2}^{Air}}{P_{O_2}^{Atm}} \quad (4.7)$$

where $\mu_{O_2}^{Atm}$ and $P_{O_2}^{Air}$ is oxygen chemical potential and oxygen partial pressure in air, respectively. The cell and CSZ oxygen sensor must be located in the isothermal zone to minimize the errors by thermo-electromotive force of CSZ and temperature dependence of gas phase equilibrium. The isothermal zone was determined to be 30 mm. The temperature of the sample, Pt electrode 20 mm below the sample and CSZ oxygen sensor was monitored during the experiment by an R-type thermocouple. Due to the difficulty to maintain the wide isothermal zone, the temperature of oxygen sensor is always below the temperature of the cell by around 10 K. The temperature on the sample surface and oxygen sensor was used respectively to calculate the surface oxygen potential and oxygen potential (oxygen partial pressure) in the atmosphere.

The cell was heated to 1073 K with flowing Ar-21%O_2 or Ar-20%O_2-20%H_2O mixed gas for experiment in dry or humid conditions, respectively. The heating rate is 2.9 x 10^{-1} Ks^{-1} and the gas flowing rate is 1.67 x 10^{-6} m^3s^{-1}. The experiment was carried out up to 20 ks. After the experiment, the cell was cool down in the furnace. To investigate the change of surface oxygen potential with the presence of water vapor, in addition to above experiments, Fe-10Cr was also oxidized in dry-humid and humid-dry sequenced conditions.

A blank experiment using Pt foil as a sample was carried out to investigate the surface oxygen potential, where no oxygen was consumed. Principally, without oxygen consumption the surface oxygen potential is equivalent to the atmosphere.

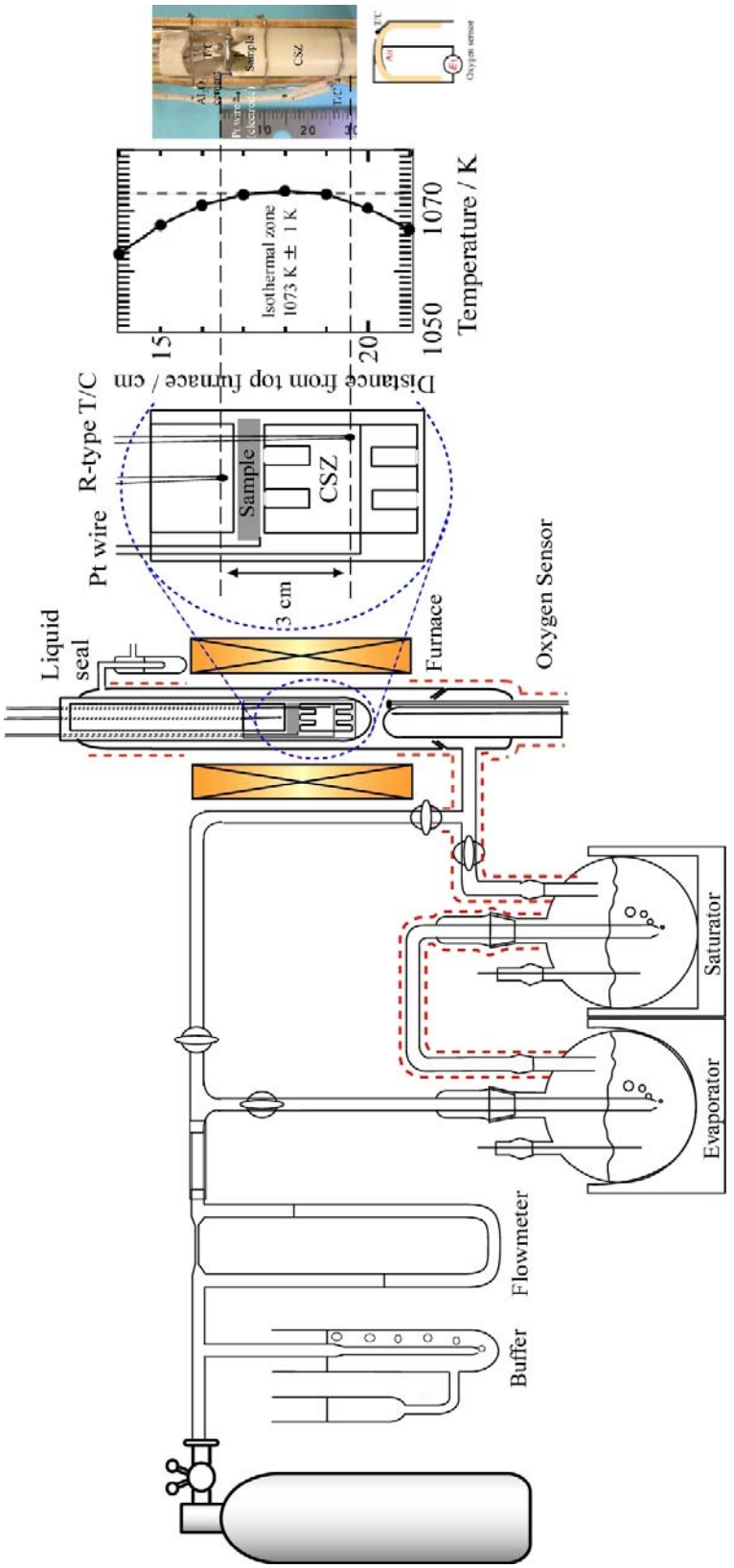

Fig. 4.4 Schematic diagram of the experimental apparatus.

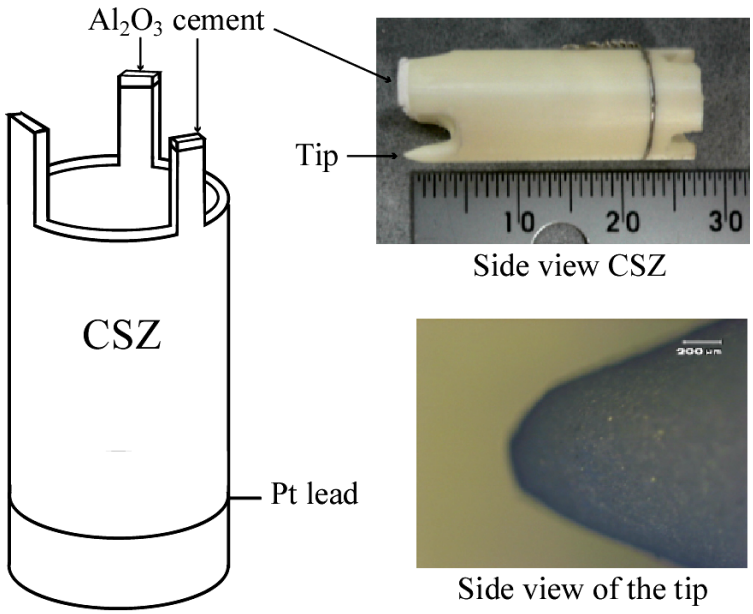

Fig. 4.5 Schematic diagram of CSZ tube and the side view.

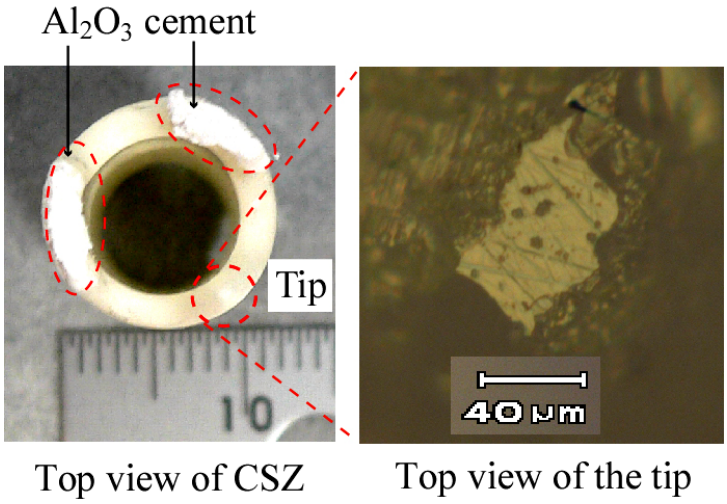

Fig. 4.6 Top view of CSZ tube and CSZ tip.

4.4 Results

4.4.1 Blank experiment using Pt foil

Figures 4.7 and 4.8 show the emf generated in the cell and oxygen sensor during the blank experiment using Pt foil as a sample in Ar-21%O_2 (dry) and Ar-20%O_2-20%H_2O (humid) mixed gas. The temperatures of the sample, Pt electrode 20 mm below the sample and CSZ oxygen sensor are also presented in both figures. The temperature difference between the sample and Pt electrode is around 5 K during the experiment. However, because of the position of the oxygen sensor that slightly out of the isothermal region, the temperature differs by 10 K from the sample temperature in dry condition. However, during the experiment in humid condition, the temperature of oxygen sensor is higher that the sample by 10 K. The temperature is stable during the experiment, and the fluctuation is within $\pm$1 K. The temperature of sample was used to calculate the surface oxygen potential, and the temperature of CSZ oxygen sensor was used to calculate the oxygen potential at the atmosphere.

In Ar-21%O_2 mixed gas, the emf of oxygen sensor is stable at 0.5 mV during the experiment, and the atmosphere oxygen partial pressure is 2.1 x 10^4 Pa calculated using E_{sensor} and the equation (4.7). In Ar-20%O_2-20%H_2O mixed gas, the emf of oxygen sensor is around 1 mV, which gives the oxygen partial pressure of 2.0 x 10^4 Pa. The results assure that the CSZ oxygen sensor correctly monitor the oxygen partial pressure of the atmosphere. The emf of the cell is generated during the heating period, probably due to temperature difference between the two electrodes. After the heating period, when the temperature is stable the emf of the cell is almost 0 mV. These results assure that the emf caused by thermo-electromotive force is negligibly small.

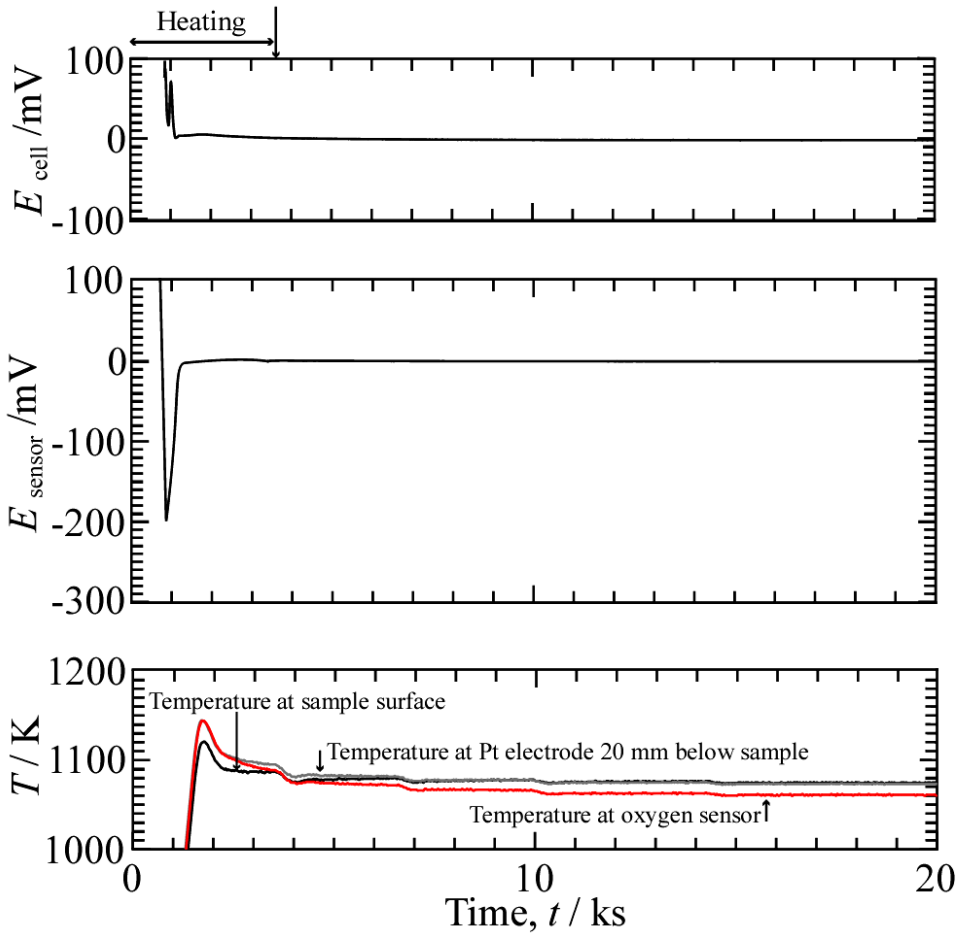

Fig. 4.7 The emf of the cell and oxygen sensor during the blank experiment using Pt foil as a sample in Ar-21%O_2 at 1073 K.

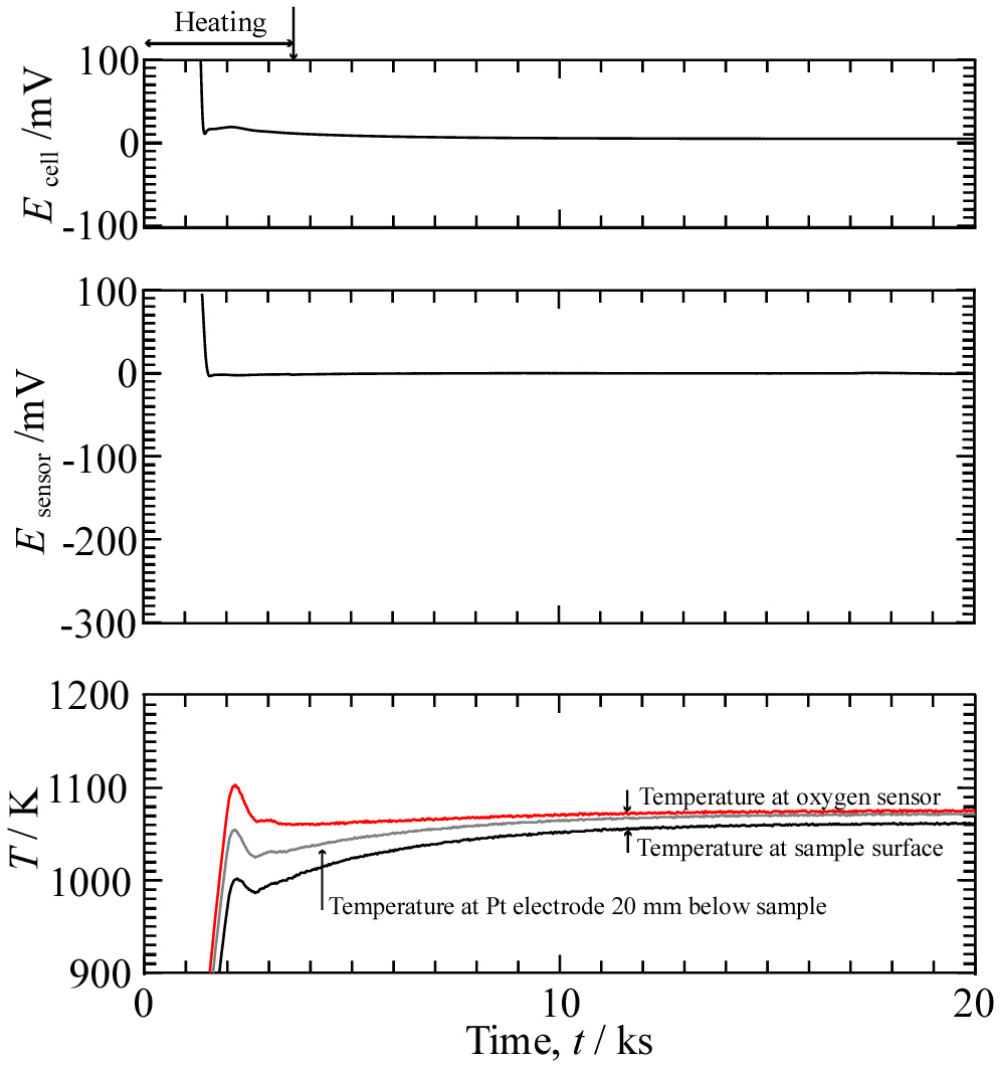

Fig. 4.8 The emf of the cell and oxygen sensor during the blank experiment using Pt foil as a sample in Ar-20%O_2-20%H_2O mixed gas at 1073 K.

4.4.2 Oxidation of Fe-Cr alloys in Ar-21%O_2 mixed gas

Figure 4.9 shows the temperature of each cell and oxygen sensor using Fe, Fe-5~17Cr as sample. All cells show a stable temperature after heating period. The temperature difference between sample surface and 20 mm below the sample is scattered from 2 K to 5 K. The temperature of oxygen sensor is lower by 10 K from the sample temperature. However, in case of Fe-17Cr alloy, the oxygen sensor temperature is almost same as the sample temperature. The fluctuation of temperature is within ±1 K.

Figure 4.10 shows the emf generated during the oxidation of Fe, Fe-5~17Cr alloys in dry condition. The emf of oxygen sensor and temperature also presents in the same figure. The emf of Fe, Fe-5Cr is largely positive during the initial stage of oxidation, and decrease with the increasing of oxidation time. The emf of the sample decreases with the increase of Cr concentration. In Fe-10~17Cr alloys, the emf drops sharply right after the temperature is stable. Fe-12Cr and Fe-17Cr shows lowest emf among the samples about 10 mV. The emf of sensor is around 0 mV to –1 mV.

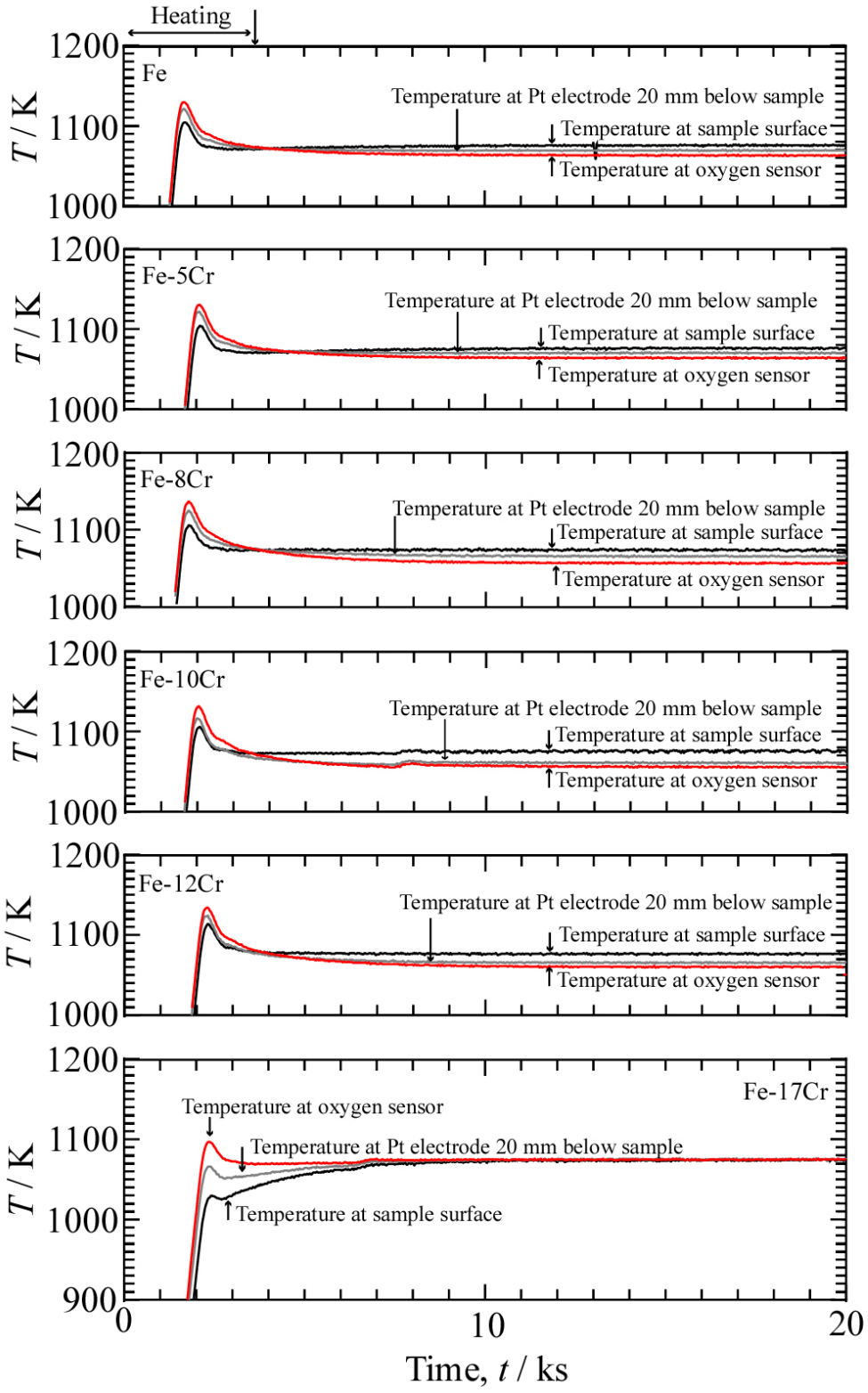

Fig. 4.9 The temperature of each cell and oxygen sensor with Fe, Fe5-17Cr as the sample in Ar-21%O_2 mixed gas.

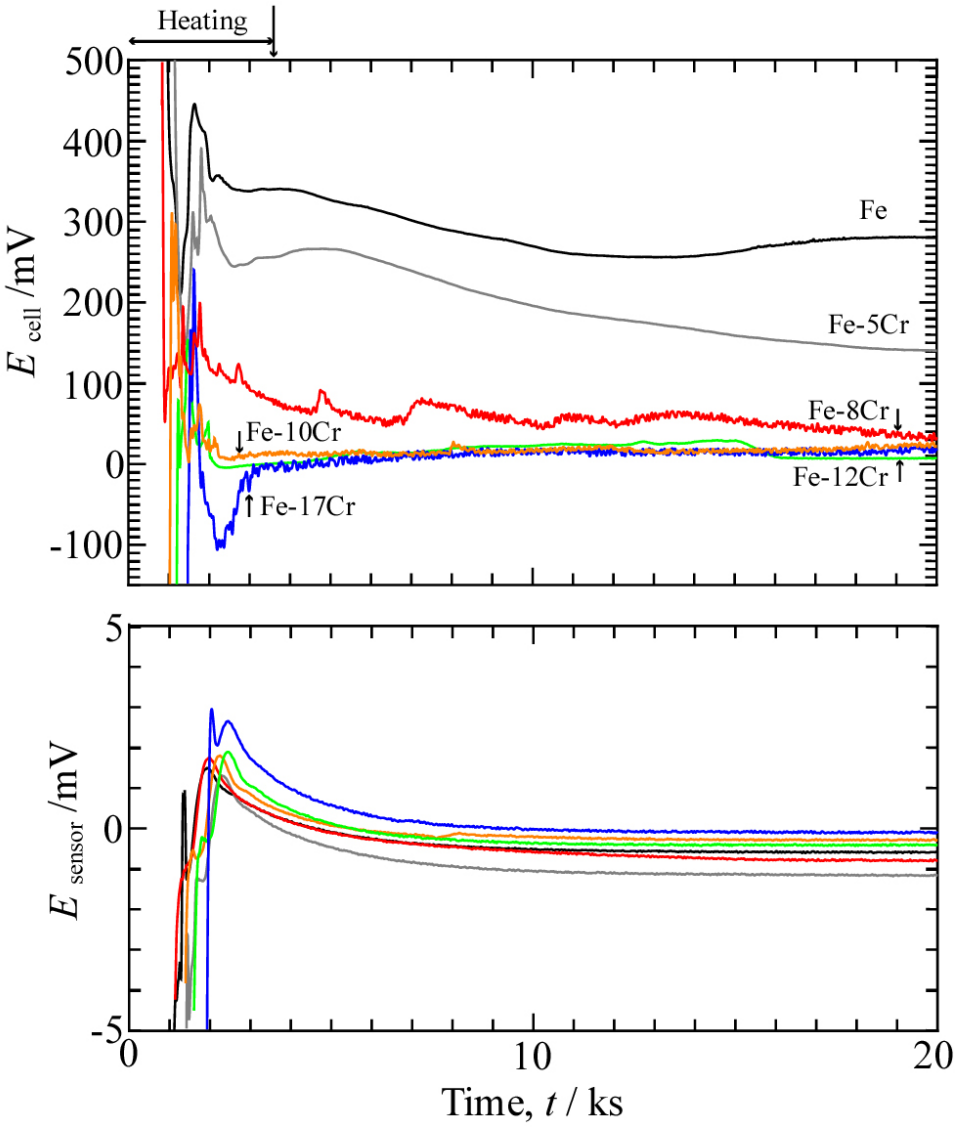

Fig. 4.10 The emf of cell and oxygen sensor at 1073 K in Ar-21%O_2 mixed gas.

4.4.3 Oxidation of Fe-10~17Cr alloys and Fe-22Cr steel in Ar-20%O_2-20%H_2O mixed gas

Figure 4.11 shows the temperature of each cell and oxygen sensor using Fe-10~17Cr alloys and Fe-22Cr steel as the sample. The temperature is stable with fluctuation of ±1 K. The temperature of oxygen sensor is higher by 15 K compared to the sample temperature. The temperature difference between sample surface and 20 mm below the sample is scattered from 2 K to maximum 5 K.

Figure 4.12 shows the emf generated during the oxidation of Fe-10~17Cr alloys and Fe-22Cr steels in humid condition. The emf of oxygen sensor of the atmosphere also presents in the same figure. The emf of Fe-10~17Cr is largely positive during the oxidation and intensely fluctuates. The emf of the sample is decrease with the increase of Cr concentration. However, Fe-22Cr shows that the emf is around 0 mV.

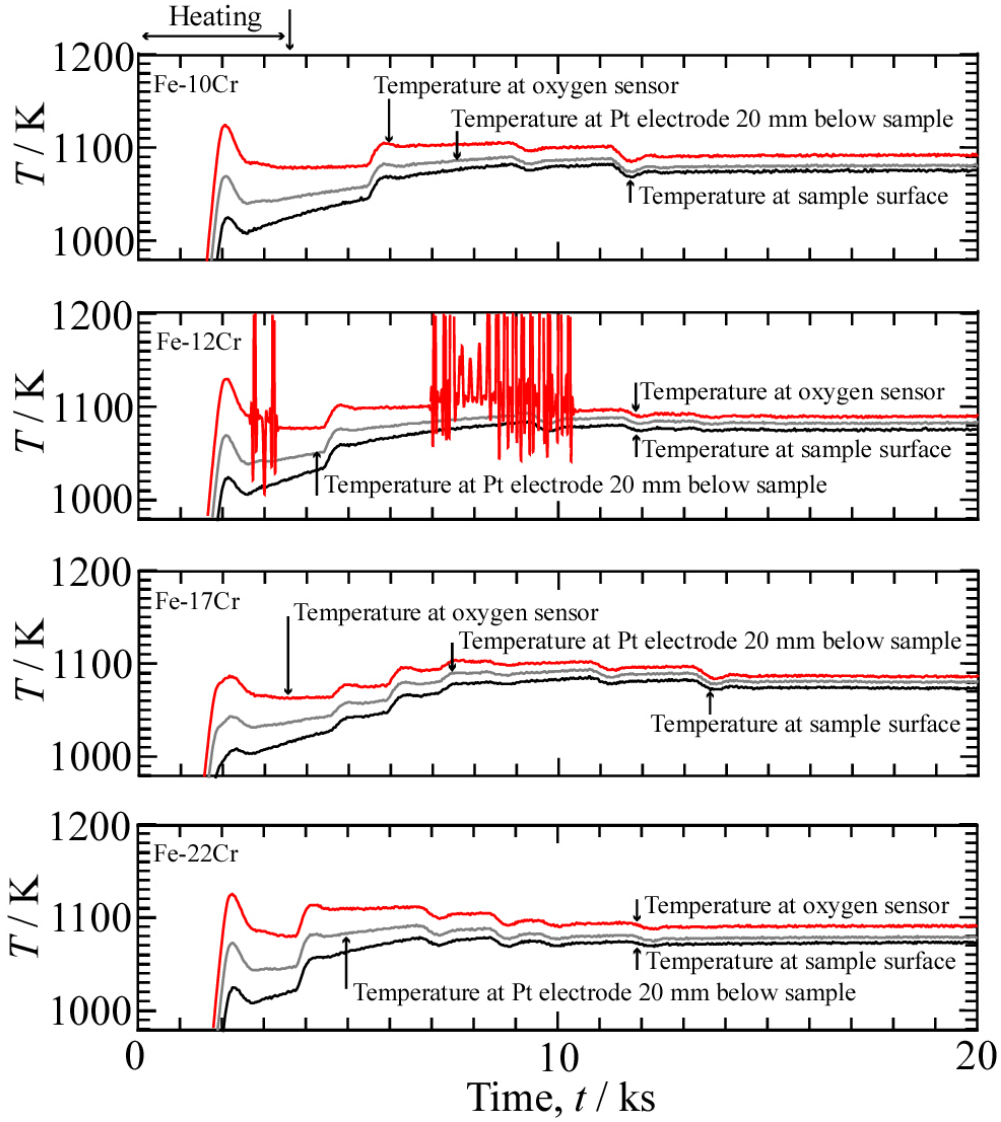

Fig. 4.11 The temperature of each cell and oxygen sensor using Fe-10~17Cr alloys and Fe-22Cr steel as the sample during oxidation in Ar-20%O_2-20%H_2O mixed gas at 1073 K.

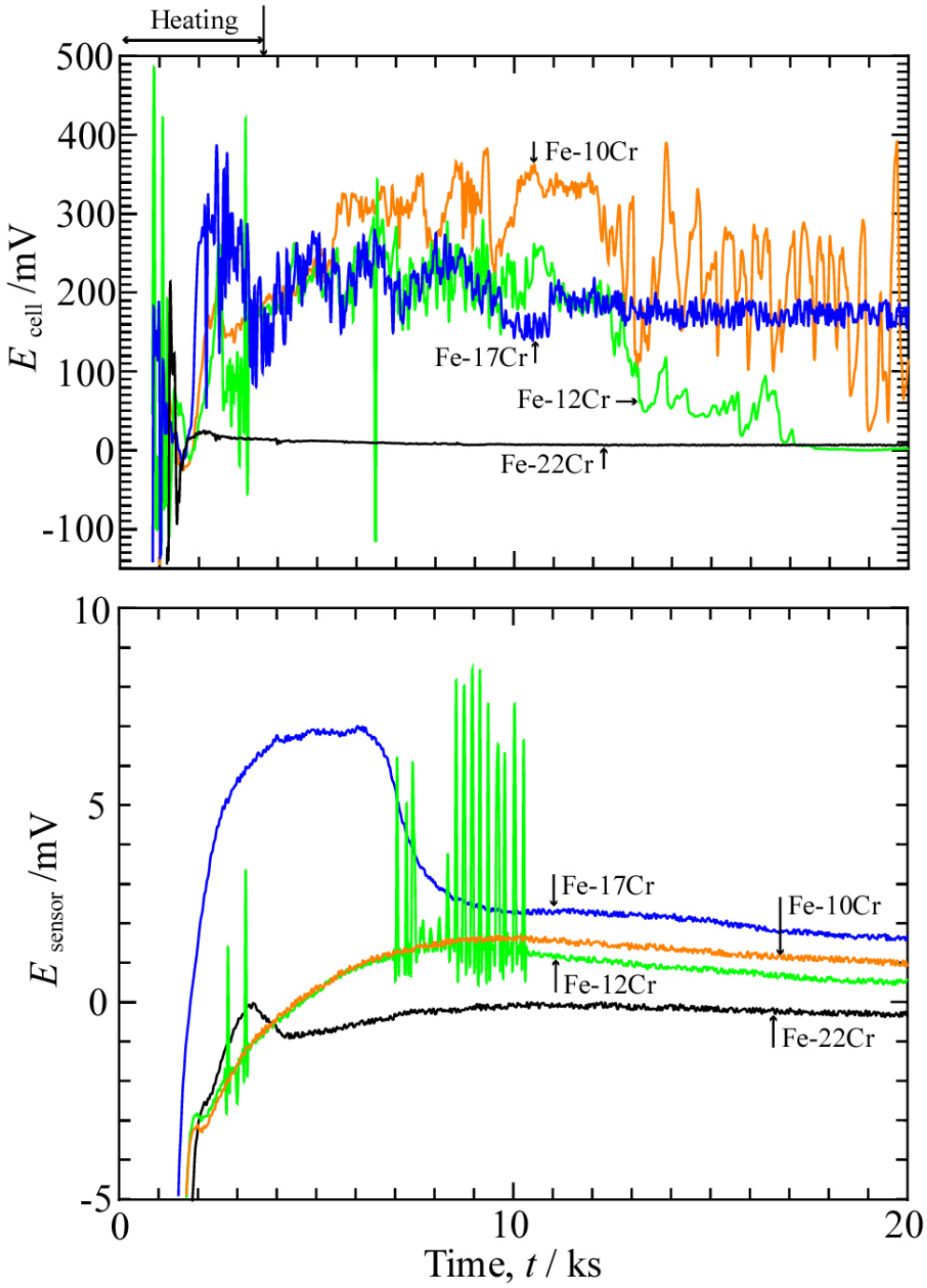

Fig. 4.12 The emf generated during the oxidation of Fe-10~17Cr alloys and Fe-22Cr steel in Ar-20%O_2-20%H_2O mixed gas at 1073 K.

4.4.4 Surface of oxide scale contacted with CSZ

The surface morphology of the samples oxidized in Ar-21%O_2 and Ar-20%O_2-20%H_2O mixed gas is shown in Fig. 4.13. In Ar-21%O_2 mixed gas, the surface of Fe-10~17Cr is flat covered with oxide. While in Fe-8Cr some part of the oxide surface is having a hemisphere shape. Fe-8Cr is probably the transition point between the formation of oxide scale that adheres to the alloy and the scale that exfoliates. The XRD patterns of the oxide surface shown in Fig. 4.14 confirms that Cr_2O_3 forms in the Fe-10~17Cr alloys. The oxide on Fe and Fe-5Cr alloys is severely exfoliated during cooling process. The XRD patterns of the samples on the exfoliated surface in Fig. 4.16 show that Fe_2O_3 and Fe_3O_4 were formed.

In Ar-20%O_2-20%H_2O mixed gas, the surface of Fe-10~17Cr alloys and Fe-22Cr steel is relatively flat and no exfoliation is observed. However, surface XRD patterns of Fe-10~17Cr in Fig.4.15 show that Fe_2O_3 and Fe_3O_4 were formed. It was confirmed that Cr_2O_3 is the only oxide phase presents in Fe-22Cr steel.

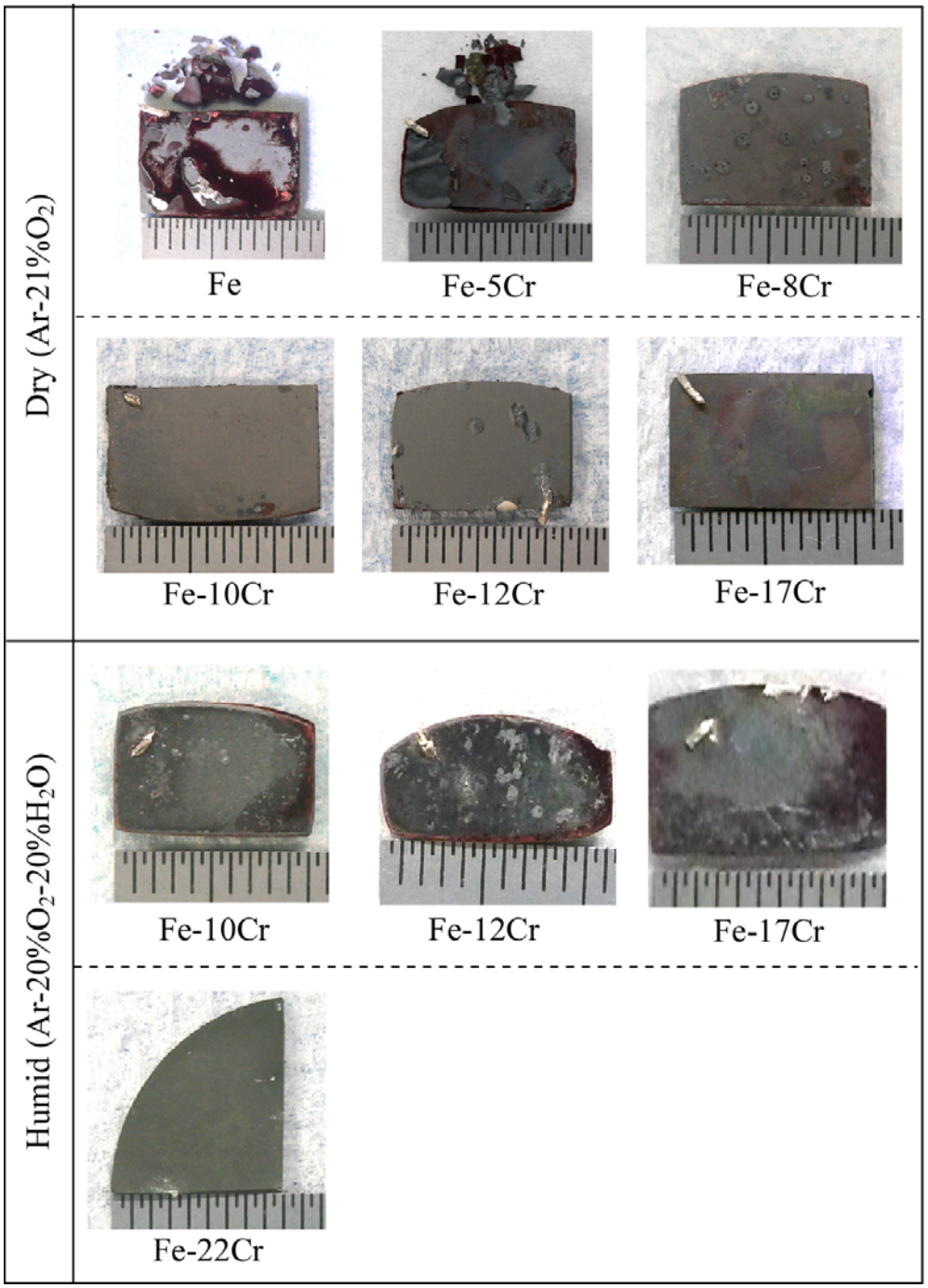

Fig. 4.13 Surface morphology of the samples oxidized in Ar-21%O_2 and Ar-20%O_2-20%H_2O mixed gas at 1073 K.

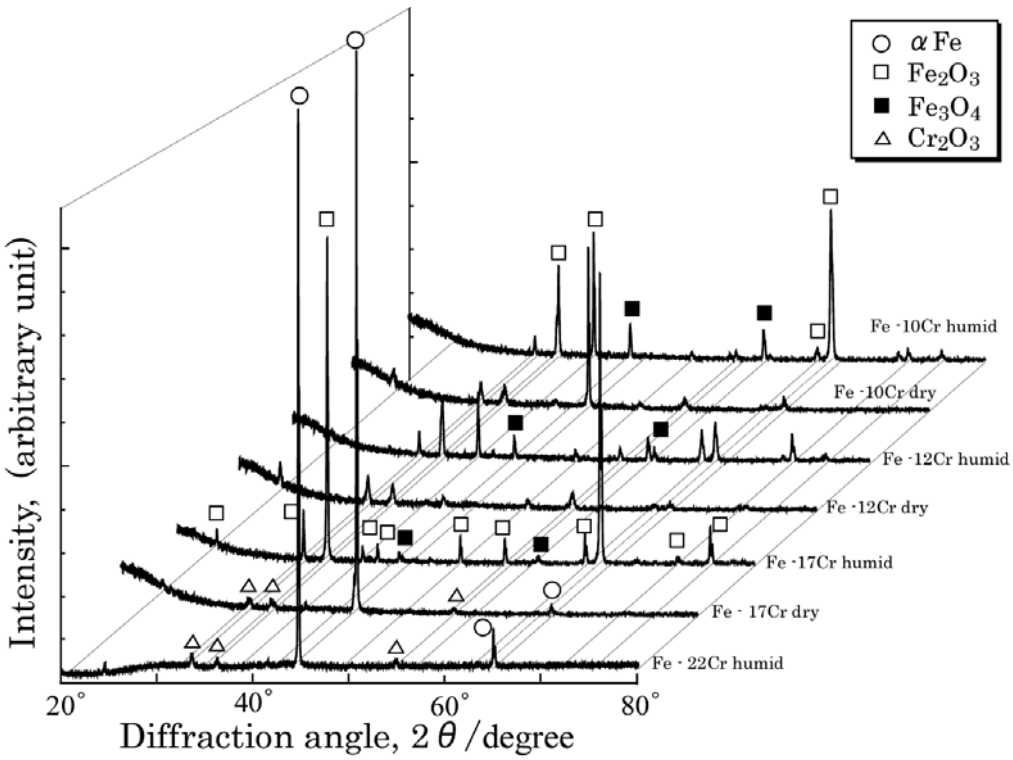

Fig. 4.14 XRD patterns of Fe-10Cr alloys and Fe-22Cr steel oxidized in Ar-21%O_2 (dry) and Ar-20%O_2-20%H_2O (humid) mixed gas at 1073 K.

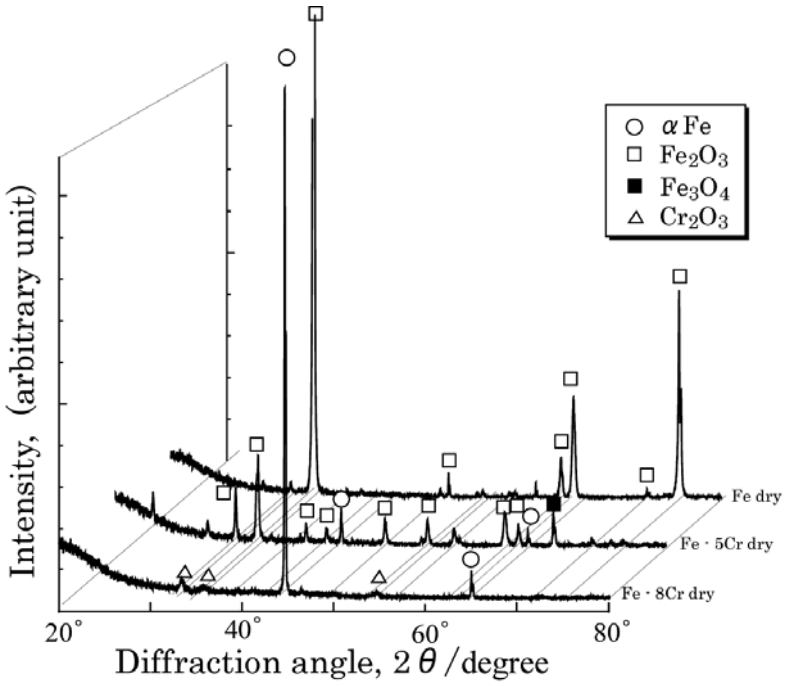

Fig. 4.15 XRD patterns of Fe, Fe-5Cr and Fe-8Cr oxidized in Ar-21%O_2 mixed gas at 1073 K.

4.5 Discussion

4.5.1 Oxygen chemical potential on the surface of oxide scale during oxidation in Ar-21%O_2 and Ar-20%O_2-20%H_2O mixed gas

Figure 4.16 shows the oxygen chemical potentials in the atmosphere, on the surface of respective oxide scale in the Fe, Fe-5~17Cr alloys calculated from the emfs of the cell and sensor during oxidation in Ar-21%O_2 mixed gas. The oxygen chemical potentials on the surface of Fe-10~17Cr are close to oxygen potential in the atmosphere shortly after the heating period. The difference of generated emf is maintained during the oxidation. With the decrease of Cr concentration, such as in Fe-8Cr, the difference between surface oxygen potential and oxygen potential in the atmosphere becomes larger. In Fe-8Cr, the difference is slowly decreased with oxidation time. This indicates that oxygen consumption in Fe-8Cr is larger than Fe-10~17Cr especially at the initial stage. The growth of oxide scale is decreases as the scale thickness in increase, which gives the smaller difference between surface oxygen potential and oxygen potential in the atmosphere at longer oxidation time. The low surface oxygen potential on Fe and Fe-5Cr indicates the rapid consumption of oxygen and the rapid growth of iron oxides.

Figure 4.17 shows the surface oxygen potential on the Fe-10~17Cr alloy and Fe-22Cr steel in Ar-20%O_2-20%H_2O mixed gas at 1073 K calculated from emf generated in the cell and sensor shown in Fig. 4.12 at 1073 K. The oxygen chemical potential on the surface of Fe-10~17Cr is drastically decreased up to 4 order of magnitudes from the oxygen potential in the atmosphere. This is a remarkable difference from the same samples that oxidized in dry condition. Higher Cr concentration as such in Fe-22Cr steel indicates that the surface oxygen potential is close to the oxygen potential at the atmosphere. This could be understood that protective Cr_2O_3 scale is formed on the sample.

From the above results, it is obvious that Fe with 10wt% Cr and above gives the formation of protective Cr_2O_3 scale in Ar-21%O_2 mixed gas. However, in Ar-20%O_2-20%H_2O mixed gas, up to 22wt% Cr is required to form protective Cr_2O_3

scale. These results conform that water vapor affects the formation of protective Cr_2O_3 scale. This fact demonstrates that continuous monitoring of surface oxygen potential can be applied to distinguish the formation of protective scale in dry or humid condition.

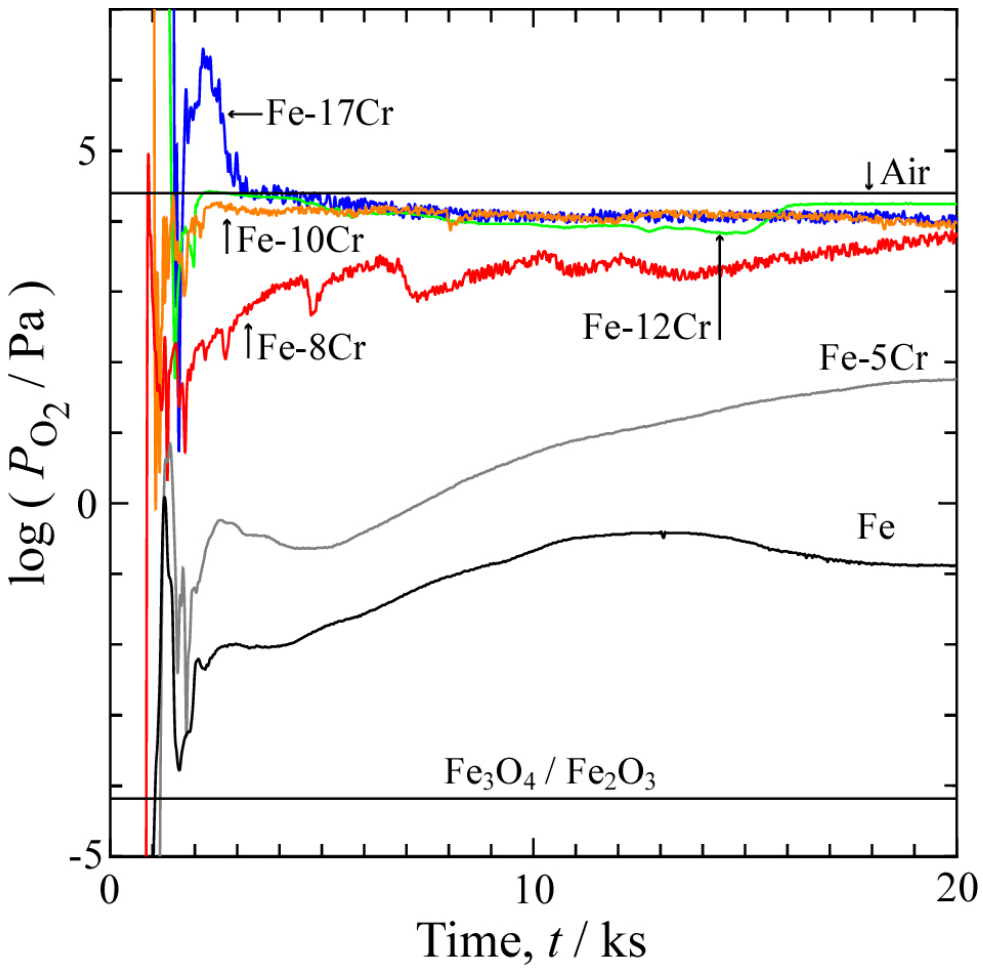

Fig. 4.16 Surface oxygen potential of Fe, Fe-5~17Cr alloys at 1073 K in Ar-21%O_2 mixed gas.

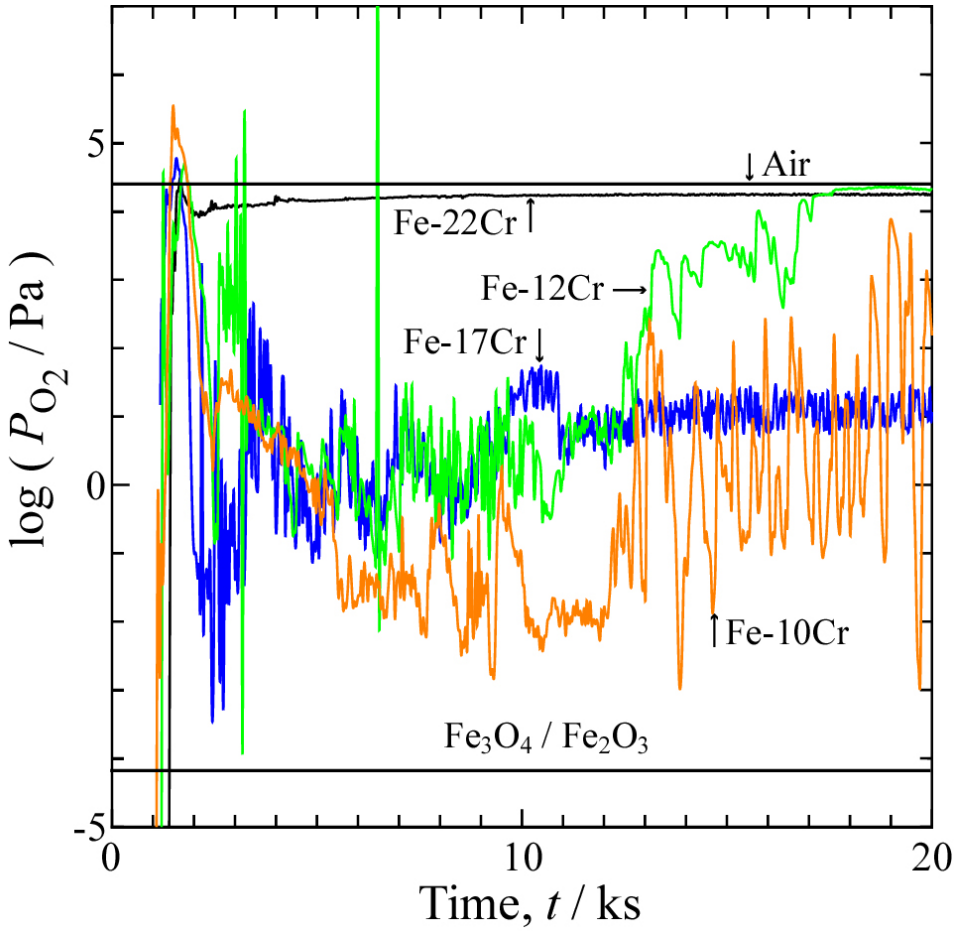

Fig. 4.17 Surface oxygen potential of Fe-10~17Cr alloys and Fe-22Cr steel at 1073 K in Ar-20%O_2-20%H_2O mixed gas.

4.5.2 Increase of Cr concentration to form protective scale in Ar-20%O_2-20%H_2O mixed gas

Figure 4.18 summarizes the scale morphology on the alloys that exposed in dry and humid condition. As could be observed from the Fig. 4.18, Cr concentration required to form protective scale in dry is 10wt%, while in humid condition is up to 22wt%. In humid condition, the emf of cell of the alloys with Cr concentration below 17wt% fluctuates significantly compared to the Fe-22Cr steels as shown in Fig 4.12 and Fig 4.10. The fluctuation of emf reflects to the rapid changes in oxygen potential on the triple phase boundary. This suggests that with the presence of water vapor cracks was actively generated. The oxygen uptake was very large at the crack formation. However, because the concentration of Cr is high, the crack was quickly healed by the formation of new Cr_2O_3 scale. During this time oxygen was less consumed until new crack propagated. The repeating formation of cracks and protective scale generates the fluctuation of the emf.

Renusch [2] and Schutze [3] have observed similar behavior on Fe-9Cr alloys that oxidized in humid condition by acoustic emission (AE) measurement. Figure 4.19 shows the AE from samples oxidized in dry and humid conditions at 923 K. Sample in dry condition does not emit any signal, while the acoustic emission was detected on the sample in humid condition. Schutze [3] explains that cracks are generated in order to relieve the stress generated during oxidation. The generation of cracks gives the acoustic emission signal. Due to generation of cracks, the oxidation rate in humid condition was accelerated.

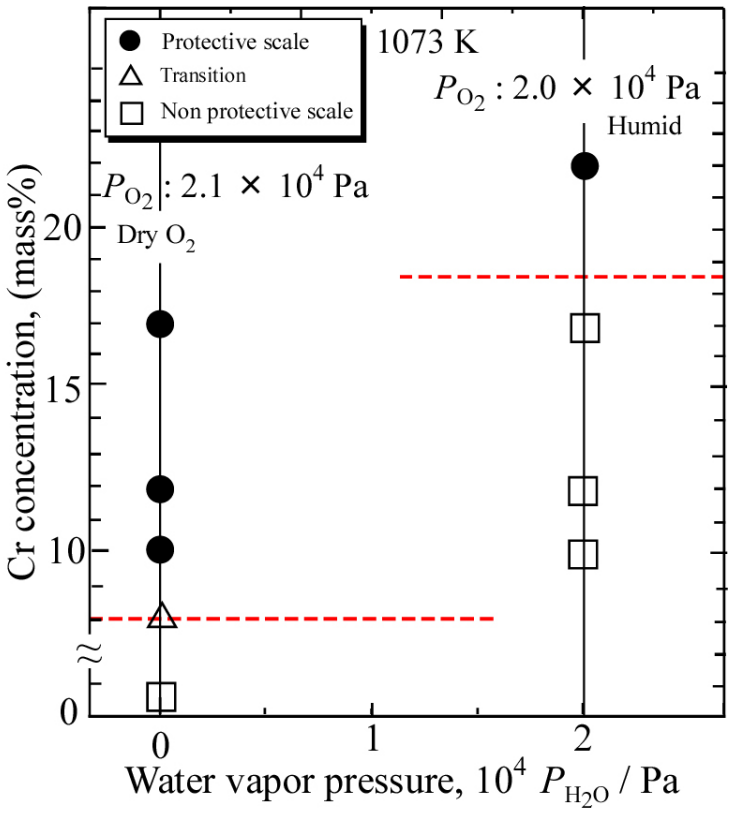

Fig. 4.18 Type of scale forms on the alloys in dry and humid condition.

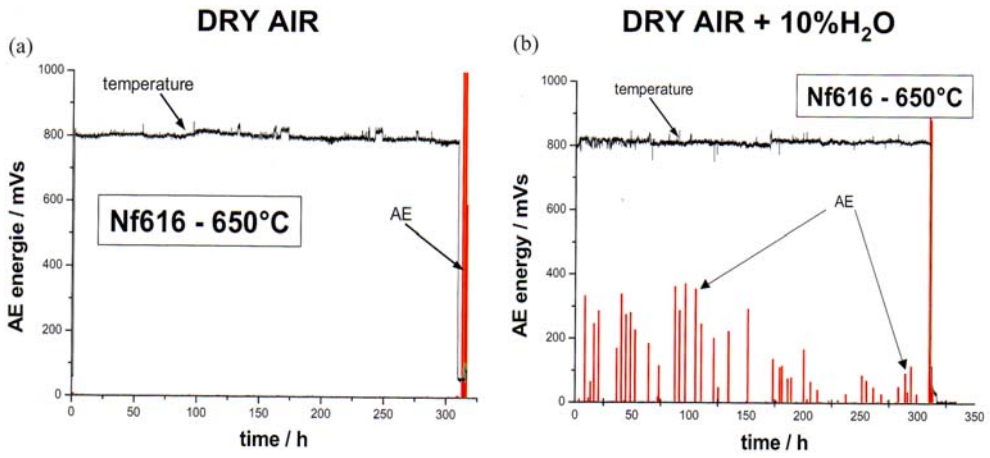

Fig. 4.19 Acoustic Emission signal of the samples oxidized in dry and humid condition at 923 K [3].

4.6 Conclusion

The oxygen chemical potential on growing oxide scale of Fe, Fe5~17Cr alloys and Fe-22Cr steel in Ar-21%O_2 and Ar-20%O_2-20%H_2O mixed gas was monitored continuously using oxygen concentration cell of CSZ. In Ar-21%O_2 mixed gas, the oxygen chemical potential of the oxide formed on Fe-10~17Cr alloys is slightly smaller than the atmosphere. This is due to the formation of protective Cr_2O_3 scale. The surface oxygen potential of Fe and Fe-5Cr is largely decrease due to the formation of non-protective Fe oxides. In Ar-20%O_2-20%H_2O mixed gas, the surface oxygen potential of Fe-22Cr steel is slightly smaller than the atmosphere. The surface oxygen potential of Fe alloys with Cr concentration up to 17wt% is largely decreased from the atmosphere due to the formation of Fe oxides. The presence of water vapor may enhances the crack formation of scales and results in the formation of non-protective Fe oxides. The measurement of surface oxygen potential can be applied to distinguish the formation of protective scale at early stage of oxidation.

References

[1] Kojiro Akiba, Mitsutoshi Ueda, Kenichi Kawamura and Toshio Maruyama, *Materials Transactions*, **49**(3), 629 – 636 (2008).

[2] D. Renusch and M. Schutze, *Materials at High Temperatures*, **22**(1/2), 35-45 (2005).

[3] M. Schutze, D. Renusch and M. Schorr, *Materials at High Temperatures*, **22**(1/2), 113-120 (2005).

Chapter 5

Conclusion

5.1 Summary

The effect of water vapor on the transition from internal to external oxidation is an important aspect in the high temperature oxidation of ferritic Fe-Cr alloys. The objective of this study is to quantitatively clarify the water vapor effect using Wagner treatment of binary alloys oxidation. The study was focused on the transition from internal to external oxidation of ferritic Fe-Cr alloys in steam condition compared to dry condition. The results are summarized as below.

In **Chapter 1 ; "Introduction"**, the background and objective of this study was presented with the emphasis to increase power generation efficiency in conventional fossil fuel power plant and SOFCs.

In **Chapter 2 ; "High temperature oxidation of Fe-Cr alloy at 1073 K in dry and humid atmospheres with the oxygen partial pressure of the Fe-FeO coexistance"**, the effect of water vapor on the oxidation of the alloys in Fe/FeO oxygen partial pressure at 1073 K was clarified base on Wagner theory of alloy oxidation. It was showed that the transition from internal to external oxidation occurs on Fe-8Cr and Fe-12Cr in dry and humid condition, respectively. It was proposed that the increase of oxygen permeability under humid condition increase the Cr concentration required to

form external scale.

In **Chapter 3 ; "Oxygen permeability in α-Fe at 1073 K under dry and humid conditions"**, the permeability of oxygen was measured form internal oxidation of Fe-0.5 ~ 2.25% Cr alloys in dry and humid condition. The increase of oxygen permeability increases the critical Cr concentration to form external scale in humid condition by 1.2 times. Microstructure change of internal precipitated oxide was observed on sample oxidized in humid condition. This is due to the existence of dissolved hydrogen in the alloy.

In **Chapter 4 ; "Oxygen potential on the surface of growing oxide scale during oxidation of Fe-Cr alloys at 1073 K in dry and humid atmospheres"**, a new method was proposed to monitor the formation of protective scale on Fe-Cr alloys at early stage of oxidation by continuously measuring the surface oxygen potential. The oxygen chemical potential on growing oxide scale of Fe, Fe5~17Cr alloys and Fe-22Cr steel in Ar-21%O_2 (dry) and Ar-20%O_2-20%H_2O (humid) mixed gas was monitored continuously using oxygen concentration cell of CSZ. In Ar-21%O_2 mixed gas, the oxygen chemical potential of the oxide formed on Fe-10~17Cr alloys is slightly smaller than the atmosphere. This is due to the formation of protective Cr_2O_3 scale. The surface oxygen potential of Fe and Fe-5Cr is largely decrease due to the formation of non-protective Fe oxides. In Ar-20%O_2-20%H_2O mixed gas, the surface oxygen potential of Fe-22Cr steel is slightly smaller than the atmosphere. The surface oxygen potential of Fe alloys with Cr concentration 17wt% and below is largely decreased from the atmosphere due to the formation of Fe oxides. The presence of water vapor may enhances the crack formation of scales and results in the formation of non-protective Fe oxides. The measurement of surface oxygen potential can be applied to distinguish the formation of protective scale at early stage of oxidation.

In **Chapter 5 ; "Conclusion"**, the results from this study is was summarized.

Index of tables

Index of figures

Acknowledgement

This dissertation has been submitted for the partial fulfillment for the degree of Doctor of Engineering at Tokyo Institute of Technology. I am deeply indebted to Professor Dr Toshio Maruyama who gave myriad directions from constitution of the thesis to detailed discussions and kindly showed much patience with my tardy progress in the compilation. I would like to express my deepest appreciation for his continuous encouragement and supervision.

A special debt of gratitude goes to Associates Professor Dr Kenichi Kawamura and Assistant Professor Dr Mitsutoshi Ueda for their cooperative supervision through many fruitful discussions, candid opinions and valuable suggestions both in experimental techniques and data analysis.

I greatly appreciate the suggestions and comments from the members of my thesis examiner, Professor Dr Tooru Tsuru, Professor Dr Masahiro Susa and Associates Professor Dr Yoshinao Kobayashi. Discussions, comments and opinions from them greatly broaden my scientific perspectives.

Dr Kojiro Akiba, my close companion who I have shared a lot of my thoughts, arguments and disputes. He explained the basic concept of the measurement of surface oxygen potential that forms the Chapter 4 of this dissertation. He has always been a caring friend to answer me in hard and enjoyable times.

I have been very lucky to have a number of talented individuals doing PhD degree in the laboratory. Mr Minoru Tanaka, Mr Wei-Ping Huang and Mr Asep Ridwan Setiawan who have constantly support and help my laborious experimental works.

I have been blessed with extremely good friends in the laboratory, Mr Atsuo Tanaka, Mr Yusuke Sasaki, Mr Satoshi Tomikawa, Mr Keisuke Masaki, Mr Masakazu Yamashita, Mr Yuichi Kamo, Mr Shun Kawamura, Mr Taku Kitahara, Mr Wataru Todo, Mr Ryo Maruyama, Ms Lyta, Ms Liu Lu, Mr Kentaro Okumura, Mr Hiroto Kimura, Mr Koji Fujita and Mr Tomohiro Mizutani. I have spent a great and enjoyable time with

them. My sincere thank and heartfelt appreciation to them for their patience to my self-centered manners, and about tolerating my poor daily jokes.

Mr Kentaro Okumura has generously contributes ZMG steels for my chapter 4. Mr Koji Fujita has shows his tenderness and warm-heartedness during my thesis compilation.

I would like to extend my sincerely thank to all my colleagues with whom I share many difficulties in the research and have many useful discussions. To Kulliyah of Engineering, International Islamic University, Malaysia for continuous supports. To Ministry of Higher Education, Malaysia for financial supports. To the One I believe in.

My beloved parents, for the tears, patience, encouragements, supports and faiths, I am deeply acknowledges them.

Mohd Hanafi Bin Ani

March 26th, 2009